PHYSIK-DEPARTMENT

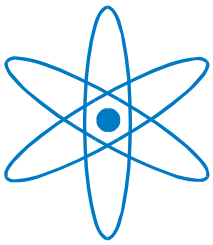

Design and tests of an adaptive focusing neutron guide

Dissertation
von

Roxana Georgiana Valicu

TECHNISCHE UNIVERSITÄT MÜNCHEN

TECHNISCHE UNIVERSITÄT MÜNCHEN

Institute E13 and E21

Design and tests of an adaptive focusing neutron guide

Roxana Georgiana Valicu

Vollständiger Abdruck der von der Fakultät für Physik der Technischen Universität München zur Erlangung des akademischen Grades eines Doktors der Naturwissenschaften
genehmigten Dissertation.

Vorsitzender : Univ.-Prof. Dr. H. Friedrich
Prüfer der Dissertation:

1. Univ.-Prof. Dr. Winfried Petry
2. Univ.-Prof. Dr. Peter Böni

Die Dissertation wurde am 09.07.2012 bei der Technischen Universität München eingereicht und durch die Fakultät für Physik am 23.08.2012 angenommen.

Abstract

Diese Arbeit beinhaltet die Monte Carlo Simulationen, sowie die erste Tests mit einem adaptiv fokussierenden Neutronenleiter zur Erzeugung eines wellenlängenunabhängigen Fokus.

Bekannte Neutronenleiter umfassen häufig einen Kanalkörper quadratischen Querschnitts, zusammengesetzt aus vier Glasplatten. Die Innenfläche des Kanalkörpers ist beispielweise mit einer komplexen Struktur von Metallschichten belegt. Durch diese soll, analog zur Lichtoptik, ein durchlaufender Neutronenstrahl reflektiert und letztlich weitergeleitet werden.

Für eine Strahlfokussierung stehen mittlerweile Neutronenleiter mit einer festgelegten Krümmung zur Verfügung. Für viele Untersuchungen ist es wichtig, den Neutronenstrahl auf eine möglichst kleine Fläche der zu untersuchenden Probe zu fokussieren. Hier hat es sich bei gekrümmten Neutronenleitern der o.g. Art, welche also eine festgelegte Krümmung besitzen, als nachteilig erwiesen, dass die Fokussierung (Grösse/Lage der Fokalfläche) wellenlängenabhängig ist. Demgemäss bedarf es für Messungen, die mit verschiedenen Wellenlängen durchgeführt werden einer entsprechenden Änderung der Krümmung des Kanalkörpers. Die Arbeit schlägt hierzu einen Neutronenleiter mit einem einfachen Mechanismus zum variablen Einstellen der Krümmung des Leiters vor. Mittels des vorgeschlagenen Mechanismus zum Einstellen der Krümmung soll eine variable Krümmung in horizontaler Richtung als auch in vertikaler Richtung des Leiters erreicht werden. Die Biegungen in horizontale und vertikale Richtung sind unabhängig von einander.

Das vorgeschlagene Element zum Einstellen der Krümmung umfasst im Wesentlichen ein Betätigungselement (Piezomotor) sowie eine Schubstange, welche mittels des Betätigungselements (in Stangen-Längsrichtung) betätigbar ist und über ein Hebelelement an der entsprechenden Glasplatte angreift. Über die Einleitung einer entsprechenden Kraft sowie eines Biegemoments am freien Ende der Glasplatte lässt sich nahezu jede geeignete Biegung erstellen. Durch Monte Carlo Simulationen haben wir die optimale parabolische Krümmung eines Neutronenleiters für das Spektrometer TOFTOF an der Forschungsneutronenquelle Heinz Maier-Leibnitz (FRM II) berechnet. Erste Tests mit Neutronen haben gezeigt dass man mit dem Adaptiv Fokussierenden Leiter bis zu einem Faktor drei in Intensität gewinnen kann einhergehend mit einer Verkleinerung der Strahlbreite im Fokalpunkt. Höhere Superspiegelung für den Leiter ermöglicht prinzipiell noch ein höher Gewinn.

Dieser Adaptive Leiter kann in allen Bereichen der Neutronenspektroskopie eingesetzt werden, um fokussierende Strahlen zu erzeugen.

Abstract

This work contains the Monte Carlo Simulations, as well as the first tests with an adaptive focusing neutron guide for creating a focus that does not depend on the wavelength of the incoming neutrons.

All known neutron guides consist of a rectangular shape, built out of four glass plates. The inner side of the guide is coated with a complex structure of metal layers. This reflects and guides the neutrons (in analogy with the reflection of the light).

For beam focusing neutron guides with fixed curvature can be built. For most experiments it is important that the beam is focused on to a small surface of the sample. In the case of focusing guides with fixed curvature it has been observed that the focusing (dimension and position of the beam focus) is wavelength dependent.

This is why for measurements that are performed with different wavelengths it is very important to change the curvature of the neutron guide in order to obtain optimal results. In this work we have designed, constructed and tested a guide where we can change the curvature during the experiment. In this way we can obtain a variable curvature in horizontal as well as in vertical direction. For a curvature in the horizontal or vertical direction it is not necessary to move all four walls, only two of the opposed plates.

The element that changes the curvature of the guide consists of an acting element (piezomotor) as well as a rod that can be operated by the piezomotor and that acts through a lever onto the plate. The action of a force and a consecutive torsion momentum at the free end of the plate changes the curvature of the whole plate in an almost parabolic way.

Making use of the Monte Carlo simulations we were able to determine the optimal curvature for each wavelength of a neutron guide for the spectrometer TOFTOF installed at the Forschungsneutronenquelle Heinz Maier-Leibnitz (FRM II). First tests have shown that with an adaptive focusing guide one can gain up to a factor three in intensity at the focal position and that the width of the beam is getting smaller. An increase in the supermirror coating of the focusing guide might bring higher gains in intensity.

These adaptive focusing guides can find applications in all fields of neutron spectroscopy for obtaining focusing beams.

Table of contents

Abstract……...5
1. Introduction……....8
2. Theoretical background……..9
2.1. Neutrons as particles……...……...9
2.1.1. Properties…….……9
2.1.2. Interaction of neutrons with matter…….……11
2.2. Neutron scattering and reflectivity……..…….12
2.2.1. Neutron scattering……..……..……12
2.2.1.a. Scattering by a fixed nucleus……..……12
2.2.1.b. Scattering of neutrons by matter…….……14
2.2.2. Neutron reflectivity…….....……18
2.3. Neutron guides……..……..……..20
2.3.1. Why do we need them?.....20
2.3.2. The principle…….……20
2.4. Recent developments……23
2.4.1. Focusing neutron guides…..…….24
2.4.1.a. Focusing principles……24
2.4.1.b. Focusing guides……..……...……30
2.4.2. Adaptive optics…….……..……...32
3. Monte Carlo simulations...……34
3.1. The Monte Carlo method……..……..34
3.1.1. Monte Carlo method versus deterministic methods……..……...37
3.1.2. McStas Simulation program…….……...38
4. Simulation results…….……44
4.1. For reaching the sub-mm range…….……44
4.1.1. The setup……...……..44
4.1.2. Simulation results…….…….……...45
4.1.3. Non symmetric setup……...……48
4.2. For PGAA……..51
4.3. Adaptive optics……..……55
4.3.1. Monte Carlo simulations…….……..56
4.3.2. Simulation results…….……58

4.3.3. Possible applications……62
5. Simulations for TOFTOF……63
5.1. The instrument……63
5.2. Monte Carlo simulations……64
5.2.1 Simulation setup……64
5.2.2. Simulation results……68
5.2.3. Calculation of radius of curvature……74
5.2.4. Adaptive optics……75
5.3. Prototype construction……82
5.3.1. Prototype design……82
5.3.2. Testing the geometry- characterization of the optical properties…84
5.3.2.a.Using the height-profilometer……84
5.3.2.b.Using the theodolyte……86
5.3.3 Corrections……89
5.3.3.a. due to the real shape of the glass……89
5.3.3.b. due to gravity……90
5.3.4. Inserting the motors……92
5.3.4.a. Determination of the parameters for each wavelength……92
5.3.4.b. Error estimations……93
5.4. First tests of the prototype at TOFTOF……99
6. Conclusions……110

Appendixes……112
5.a. Restrictions due to given geometry……112
5.b. Piezo Motor……113
5.c. Calibration……113
References……118
Acknowledgments……121
Publication list……122

1. Introduction

Neutron scattering is a powerful tool for the study of condensed matter because the wavelengths and energies of thermal and cold neutrons match well to the length and energy scales of solids and liquids. Neutron scattering is a useful source of information about the positions, motions, and magnetic properties of condensed matters.

In order to perform neutron scattering experiments far from the reactor core where the background would be far too large to permit a proper measurement, the neutrons need to be guided to the experiments using so called ~~"n~~eutron guides".

In the last years a new technique for guiding neutrons was developed (focusing guides) in which the design of a neutron guide is chosen using multiple focusing techniques depending on the desired properties of the beam at the sample position (intensity, divergence).

The aim of this work was to analyze and characterize different types of focusing guides using the Monte Carlo simulation program McStas and design an adaptive optics focusing guide for the time of flight instrument TOFTOF. Following the results of these simulations a prototype was build and tested at TOFTOF.

Chapter 2 gives a short introduction on neutron properties and principles of scattering and reflectivity as an important tool for performing measurements at a research reactor.

Recent developments in the field of neutron focusing and adaptive optics are also presented.

In chapter 3 is described the Monte Carlo method and the Monte Carlo program that allows to perform simulations where valuable information about the beam properties of an instrument can be obtained.

Chapter 4 presents various Monte Carlo simulations made for focusing in the sub-mm range, for optimizing the instrument PGAA as well as for adaptive optics.

Following the results of the simulations made for adaptive optics an optimized design is proposed for the time of flight instrument TOFTOF in chapter 5 together with the Monte Carlo simulation results, the construction of a prototype and its characterization.

In chapter 6 are presented the comparison between simulated and measured results and the steps to follow for improving the performances of the prototype.

2. Theoretical background

In this chapter are presented the properties of the neutron and its interaction with the matter. Special attention is given to neutron scattering and reflectivity, as they provide the tools for a better understanding of the principle of functioning of different instruments at the reactor and of neutron guides. Special focusing techniques are described, as well as the importance and application fields of adaptive optics.

2.1. Neutrons as particles

2.1.1. Properties

Walther Bothe and *Herbert Becker* described in 1930 an unusual type of a "*gamma radiation*", which occurred, when they irradiated metallic beryllium with *alpha-particles* (helium nuclei). *James Chadwick* recognized that the properties of this type of radiation were similar to a radiation of *neutral particles*, which were predicted 12 years before by *Ernest Rutherford*. This radiation was assumed to correspond to an uncharged nuclear constituent. When finally *Irène Joliot-Curie* (the daughter of Marie and Pierre Curie) and her husband Frédéric Joliot-Curie claimed that the "gamma radiation" of Bothe was able to knock out protons with a high energy out of paraffin, it became clear to James Chadwick that only "*neutrons*" with a mass comparable to protons would be able to do so. In the following experiments in the year 1932, *Chadwick* succeeded to show that the radiation from the irradiated beryllium was indeed the assumed uncharged nuclear particle, which was finally called the *neutron*. This discovery was essential for completing the description of the atom and its nucleus: the atomic nucleus consists of protons and neutrons and is surrounded by an electron cloud. In an electrically neutral atom the number of the negatively charged electrons in the electron cloud is exactly equal to the number of positively charged protons in the atomic nucleus. The number of neutrons in the nucleus, in contrast, can vary freely within certain ranges, giving rise to different isotopes of the same element (with given charge z, the number of protons). Neutrons together with protons are the constituents of atomic nuclei. The neutron is slightly heavier than a proton and can therefore decay into the ~~"~~lighter" particles, a proton, an electron and an anti-electron-neutrino. A neutron is only stable when bound in an atomic nucleus. The lifetime of free neutrons is about 886 seconds [Arzu01]. Neutrons are neutral only to the outside; they have an inner structure with a charge distribution of positive

and negative charges (this is similar to the neutral atoms). It has also a spin, a kind of an inner angular momentum. The moving inner charge leads to another interesting property of neutrons: it has a magnetic dipole moment and can, just as a compass needle, adjusts its spin in a magnetic field. These properties of neutrons, being neutral, having a magnetic moment and a spin, make them a very desirable tool in solid state physics. Neutrons are able to pass through massive layers with thicknesses of several centimeters. They can induce nuclear reactions, which can be used for a so-called activation analysis. The reaction leads to a radioactive nucleus, whose presence can easily be detected by its characteristic radiation. When the neutron beam is only scattered by a solid, it transports the information on the microstructure inside the solid body. Scattering of neutrons from research reactors is therefore used to study the microscopic structure of crystals, or the inner mechanical strain of big mechanical parts, like the valve of a ship diesel motor. Neutrons are also useful to study the structure of magnetic layer systems, like those used in magnetic storage media [Helm01].

To summarise here is a list of main advantages and disadvantages in using neutrons [Pynn01].

• *Advantages in using neutrons:*

– Wavelength comparable with interatomic spacings
– Kinetic energy comparable with that of atoms in a solid
– Penetrating => bulk properties are measured and sample can be contained
– Weak interaction with matter aids interpretation of scattering data
– Isotopic sensitivity allows contrast variation
– Neutron magnetic moment couples to $\boldsymbol{B}$ => neutron ~~–s~~ees" unpaired electron spins and orbital magnetism

• *Disadvantages in using neutrons:*

– Neutron sources are weak => low signals, need for large samples etc.
– Some elements (e.g. Cd, B, Gd) absorb strongly
– Kinematic restrictions (cannot access all energy and momentum transfers)

2.1.2. Interaction of neutrons with matter [Rina01]

How neutrons interact with matter affects the ways in which experiments can be performed with neutrons. Neutron interactions with the material affect the interpretation of neutron measurements. A neutron can have many types of interactions with a nucleus. Fig.2.1 shows the types of interactions and their cross sections. Each category of interaction in the figure consists of all those linked below it. The total cross section expresses the probability of any interaction taking place.

A simple notation can be used to give a concise indication of an interaction of interest.

If a neutron n impinges on a target nucleus T, forming a resultant nucleus R and the release of an outgoing particle g, this interaction is shown as T(n,g)R. The heavy nuclei are shown outside the parentheses. To denote a type of interaction without regard for the nuclei involved, only the portion in parentheses is shown.

An interaction may be one of two major types scattering or absorption. When a neutron is scattered by a nucleus, its speed and direction change but the nucleus is left with the same number of protons and neutrons it had before the interaction. The nucleus will have some recoil velocity and it maybe left in an excited state that will lead to the eventual release of radiation. When a neutron is absorbed by a nucleus, a wide range of radiations can be emitted or fission can be induced.

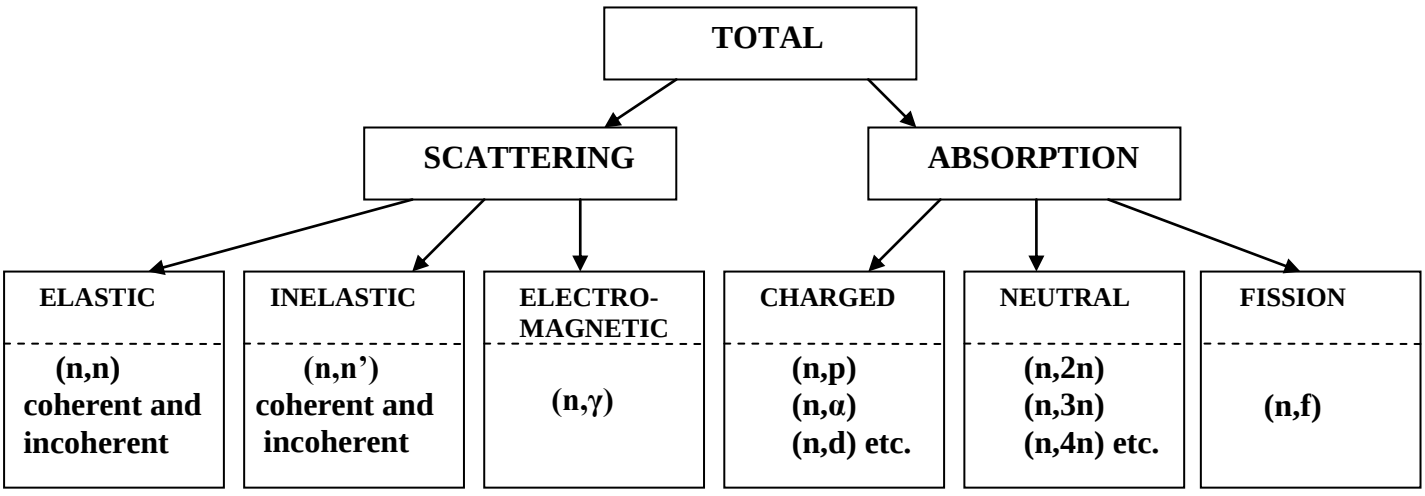

Fig.2.1 Various categories of neutron interactions. The letters separated by commas in the parentheses show the incoming and outgoing particles [Rina01].

2.2. Neutron scattering and reflectivity

2.2.1 Neutron scattering

How can we determine the relative positions and motions of atoms in a bulk sample of solid or liquid? Neutrons have no charge, and their electric dipole moment is either zero or too small to measure. For these reasons, neutrons can penetrate matter far better than charged particles. Furthermore, neutrons interact with atoms via nuclear rather than electrical forces, and nuclear forces are very short range—on the order of a few femtometers (i.e., a few times 10^{-15} meters). Thus, as far as the neutron is concerned, solid matter is not very dense because the size of a scattering center (i.e., a nucleus) is typically 100,000 times smaller than the distance between centers.

As a consequence, neutrons can travel large distances through most materials without being scattered or absorbed.

To understand the neutron scattering technique, we first examine the scattering by a single nucleus and then add up scattering from all of the nuclei within the solid or liquid we are interested in. This allows us to describe phenomena like neutron diffraction, used to determine the atomic arrangement in a material, and inelastic neutron scattering, which measures the vibrations of atoms. Minor modifications of the theory allows us to describe Small-Angle Neutron Scattering (SANS) that is used to study larger structures such as polymers and colloids as well as surface reflection of neutrons (often called reflectometry) in which layered materials and interfaces are probed. The consequences of the neutron's magnetic moment can also be explored. It leads to magnetic scattering of neutrons as well as to the possibility of polarized neutron beams that can provide enhanced information about vector magnetization in materials.

2.2.1.a. Scattering by a Fixed Nucleus

The scattering of neutrons by nuclei is a quantum mechanical process. Formally, the process has to be described in terms of the wavefunctions of the neutron and the nucleus. It is useful, to be able to switch between thinking about the wavefunction of a neutron—the squared modulus of which tells us the probability of finding a neutron at a particular point in space—and a particle picture of the neutron. This wave-particle duality is common in describing subatomic particles, and we will use it frequently, sometimes referring to neutrons as particles and sometimes as waves. Quantum mechanics tells us that the wavelength of the neutron

wave is inversely proportional to the speed of the neutron. For neutrons used in scattering experiment, the wavelength, λ, is usually between 0.1 nm and 1 nm. Often, we work in terms of the neutron wavevector, which is a vector of magnitude $2\pi/\lambda$ that points along the neutron's trajectory.

The scattering of a neutron by a free nucleus can be described in terms of a cross section, σ, measured in barns (1 barn = 10^{-28} m^2), that is equivalent to the effective area presented by the nucleus to the passing neutron. If the neutron hits this area, it is scattered isotropically, that is, with equal probability in any direction. The scattering is isotropic because the range of the nuclear interaction between the neutron and the nucleus is tiny compared with the wavelength of the neutron, so the nucleus essentially looks like a point scatterer.

Suppose that at an instant in time we represent neutrons incident on a fixed nucleus by a wavefunction $e^{i\boldsymbol{k}\cdot\boldsymbol{r}}$ in other words a plane wave of unit amplitude. The squared modulus of this wave function is unity for all positions, so the neutron has the same probability of being found anywhere but has a definite momentum $m \cdot v = hv/2\pi$. For a wave travelling in the x direction, the nodes of the wavefunction are straight wavefronts, as shown in Fig.2.2.

The amplitude of the neutron wave scattered by the nucleus depends on the strength of the interaction between the neutron and the nucleus. Because the scattered wave is isotropic, its wavefunction can be written as $(-\frac{b}{r})e^{i\boldsymbol{k}\cdot\boldsymbol{r}}$ if the scattering nucleus is at the origin of our coordinate system. The constant b, referred to as the scattering length of the nucleus, measures the strength of the interaction between the neutron and the nucleus. The minus sign means that b is a positive number for repulsive interaction between neutron and nucleus. Scattering length has the dimensions of length and is constant for a given nucleus.

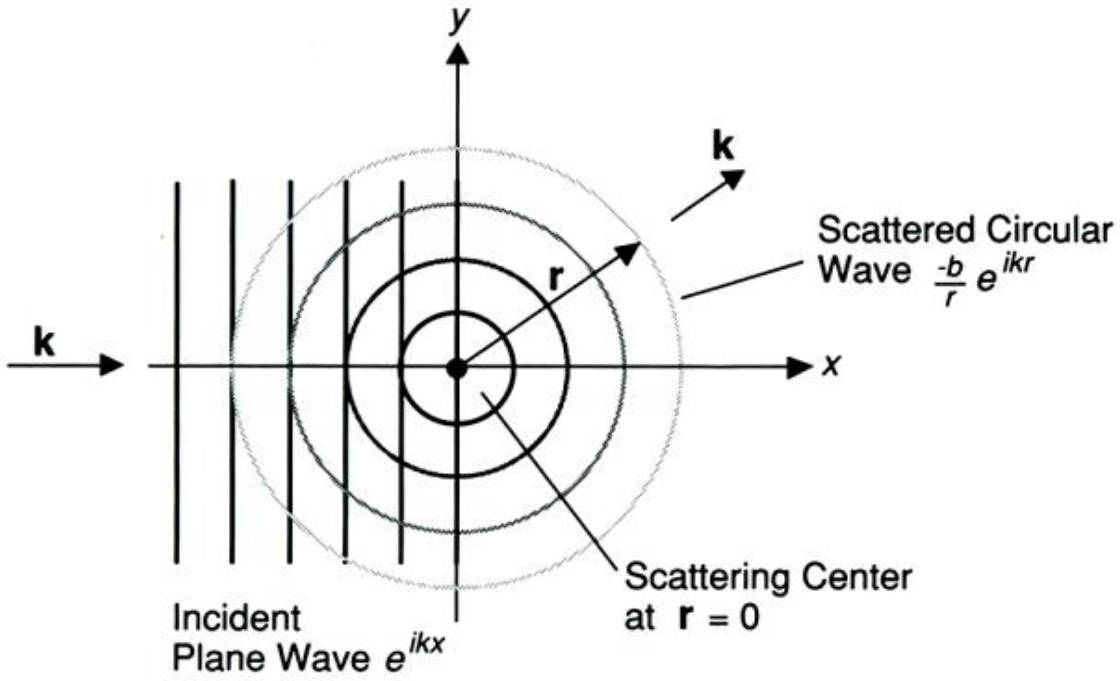

Fig.2.2. *A neutron beam incident on a single scattering center and travelling in the x direction can be represented by a plane wave with unit amplitude. Because the neutron sees the scattering center (a nucleus) as a point, the scattering will be isotropic. As a result, the scattered neutron beam spreads out in spherical wavefronts (here drawn as circles) of amplitude b/r [Sivi01].*

Because we have specified that the nucleus is fixed and because the energy of the neutron is too small to change the internal state of the nucleus, the scattering occurs without any change in the neutron's energy and is said to be elastic [Walt01]. Because the neutron's energy is unchanged by the collision, the same amount of wavevector k appears in the incident and scattered wavefunctions. It turns out that the cross section, σ, is given by $\sigma = 4\pi b^2$.

2.2.1.b. Scattering of neutrons by matter

When neutrons are scattered by matter, the process can alter both the momentum and energy of the neutrons and the matter. The scattering is not necessarily elastic as it is for a single fixed nucleus because the atoms in matter are free to move to some extent. They can therefore recoil during a collision with a neutron or, if they are moving when a neutron arrives, they can transfer energy to the neutron. As is usual in a collision, the total energy and momentum are conserved: the energy, E, lost by the neutron in a collision is gained by the scattering sample and vice versa [Prin01]. While considering the scattering of neutrons by matter, the

expression scattering vector (**Q**) is generally used which is the difference between the wave vector of the incident neutrons (**k**) and the wave vector of the scattered neutrons (**k'**). The relationship between these quantities is generally represented using –scattering triangles" [Dobr01] and these are depicted in Fig. 2.3.

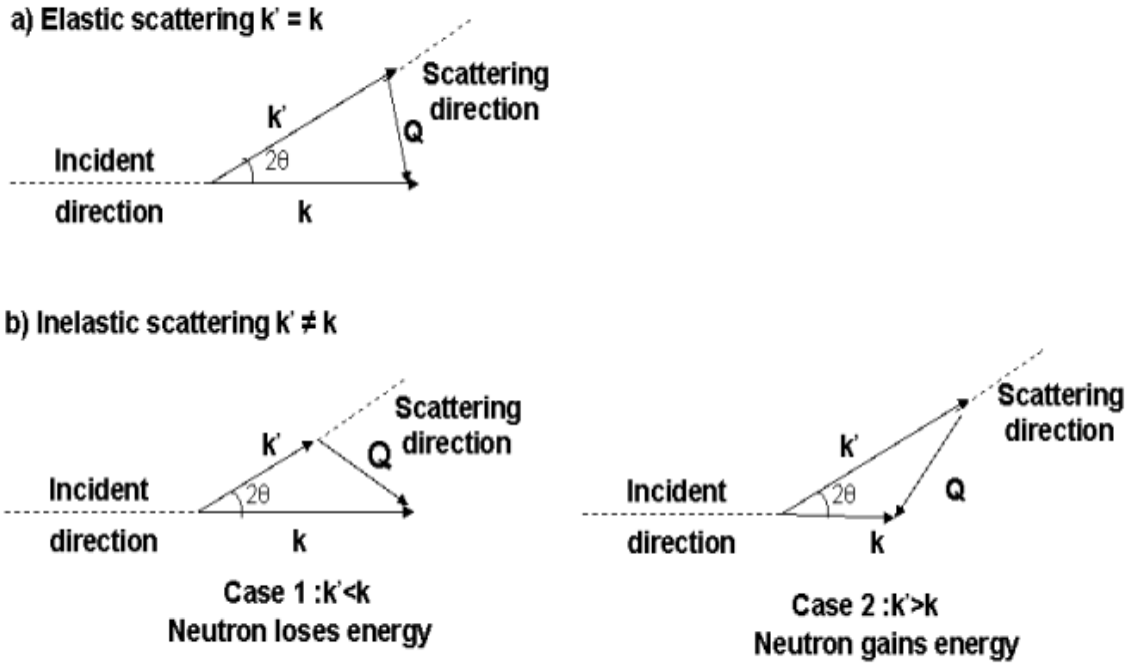

Fig.2.3 Scattering triangles in elastic and inelastic scattering (adapted from Ref. [Pynn01])

Scattering triangles are depicted here for both (a) an elastic scattering event in which the neutron is deflected but the neutron does not lose or gain energy (so that k' = k) and (b) inelastic scattering events in which the neutron either loses energy (k' < k) or gains energy (k' > k) during the interaction [Skol01] .

In both elastic and inelastic scattering events, the neutron is scattered through the same angle and the scattering vector is given by the vector relationship [Love01]:

$$\mathbf{Q} = \mathbf{k} - \mathbf{k'} \qquad 2.1$$

In neutron scattering experiments, scientists measure the intensity of neutrons scattered by matter (per incident neutron) as a function of the variables **Q** and E. The scattered intensity, denoted I (**Q**, E) is often referred to as the neutron-scattering law for the sample material.

In 1954, Van Hove [VanH01] showed that the scattering law can be written in terms of time-dependent correlations between the positions of pairs of atoms in the sample. Van Hove's result implies that I (**Q**, E) is proportional to the Fourier transform of a function that gives the probability of finding two atoms a certain distance apart.

Van Hove's work makes use of an observation made by Fermi that the actual interaction between a neutron and a nucleus may be replaced by an effective potential that is much weaker than the actual interaction. This so-called pseudo-potential causes the same scattering as the actual potential but is weak enough to be used in a perturbation treatment of scattering originally derived by Max Born. The Born approximation [Mess01] says that the probability of a neutron wave of wavevector **k** being scattering by a potential V(r) to become an outgoing wave of wavevector **k'** is proportional to:

$$\left|\int e^{i\boldsymbol{k}\cdot\boldsymbol{r}}\, V(\boldsymbol{r}) e^{i\boldsymbol{k'}\cdot\boldsymbol{r}} dr\right|^2 = \left|\int e^{i\boldsymbol{Q}\cdot\boldsymbol{r}}\, V(\boldsymbol{r}) dr\right|^2 \qquad 2.2$$

where the integration is over the volume of the sample. The potential V(r) to be used in this equation is the Fermi pseudo-potential which, for an assembly of nuclei situated at positions $\mathbf{r_j}$ is given by:

$$V(\boldsymbol{r}) = \frac{2\pi\hbar^2}{m}\sum_j b_j \delta(\boldsymbol{r} - \boldsymbol{r}_j) \qquad 2.3$$

where m is the neutron's mass and δ(r) is a Dirac delta function which takes the value unity at position **r** and is zero everywhere else. The b_j that appear in equation 2.3 are the scattering lengths that we encountered earlier. Van Hove was able to show that the scattering law could be written as:

$$I(\boldsymbol{Q}, E) = \frac{k\prime}{hk}\sum_{i,j} b_i b_j \int_{-\infty}^{\infty} \langle e^{-i\boldsymbol{Q}\cdot\boldsymbol{r}_i(0)} e^{-i\boldsymbol{Q}\cdot\boldsymbol{r}_j(\boldsymbol{t})}\rangle\, e^{\boldsymbol{i}-(\frac{\boldsymbol{E}}{\hbar})\boldsymbol{t}} dt \qquad 2.4$$

In this equation, the nucleus labeled i is at position r_i at time zero, while the nucleus labeled j is at position $\mathbf{r_j}$ at time t. Equation 2.4 is a double sum over all of the positions of the nuclei in the sample, and the angular brackets indicate that we need to do a thermodynamic average over all possible configurations that the sample could take with:

$$\sum_{i,j} b_i b_j \langle e^{-i\boldsymbol{Q}\cdot\boldsymbol{r}_i(0)} e^{-i\boldsymbol{Q}\cdot\boldsymbol{r}_j(\boldsymbol{t})}\rangle = \sum_{i,j} b_i b_j \int_{sample} \delta(\boldsymbol{r} - \boldsymbol{r}_i(0) + \boldsymbol{r}_j(t)) e^{-i\boldsymbol{Q}\cdot\boldsymbol{r}}\, d\boldsymbol{r} \qquad 2.5$$

Let us suppose further that all of the nuclei in our sample have the same scattering length so that $b_i = b_j = b$. Then the right-hand side of equation 2.5 becomes:

$$Nb^2 \int_{sample} G(\boldsymbol{r}, t) e^{-i\boldsymbol{Q}\cdot\boldsymbol{r}}\, d\boldsymbol{r} \qquad 2.6$$

where:

$$G(\boldsymbol{r}, t) = \frac{1}{N}\sum_{i,j} \delta(\boldsymbol{r} - \boldsymbol{r}_i(0) + \boldsymbol{r}_j(t) \qquad 2.7$$

and N is the number of nuclei in the sample. Evidently the function G is zero unless the separation between nucleus i at time zero and nucleus j at time t is equal to the vector **r**. Thus, the function tells us the probability that, within our sample, there will be a nucleus at the origin of our coordinate system at time zero as well as a nucleus at position **r** at time t. For

this reason this function is called the time-dependent pair correlation function because it describes how the correlation between the positions of nuclei evolves with time.

Van Hove's scattering law can be then written as

$$I(\boldsymbol{Q}, E) = \frac{Nb^2k\prime}{hk} \int_{-\infty}^{\infty} dt \int_{sample} G(\boldsymbol{r}, t) e^{-i\boldsymbol{Q}\cdot\boldsymbol{r}} e^{i(\frac{E}{\hbar})\boldsymbol{t}} d\boldsymbol{r} \qquad 2.8$$

which allows us to see that the scattering law is proportional to the space and time Fourier transforms of the time-dependent correlation function. This general result provides a unified description of all neutron scattering experiments. By inverting Equation 2.8 we can obtain from neutron scattering information about both the equilibrium structure of matter and the way in which this structure evolves with time.

Coherent scattering is the case in which neutron waves scattered from different nuclei interfere with each other. This type of scattering depends on the distances between atoms and on the scattering vector, and it thus gives information about the structure of a material.

Elastic coherent scattering tells us about the equilibrium structure, whereas inelastic coherent scattering (with $E \neq 0$) provides information about the collective motions of the atoms, such as those that produce phonons or vibrational waves in a crystalline lattice. In the second type of scattering, incoherent scattering (like isotope incoherent scattering and nuclear spin incoherent scattering), there is no interference between waves scattered by different nuclei. Rather the intensities scattered from each nucleus just add up independently. Once again, one can distinguish between elastic and inelastic scattering. Incoherent elastic scattering is the same in all directions, so it usually appears as unwanted background in neutron scattering experiments. Incoherent inelastic scattering, on the other hand, results from the interaction of a neutron with the same atom at different positions and different times, thus providing information about atomic diffusion.

In reality, atoms are not frozen in fixed positions inside a crystal. Thermal energy causes them to oscillate about their lattice sites and to move around inside a small volume with the lattice site as its center. Since an atom can contribute to the constructive interference of Bragg scattering only when it is located exactly at its official position at a lattice site, this scattering becomes weaker the more the atoms vibrate and the less time they spend at their official positions. The factor by which the Bragg peaks are attenuated because of the atomic motion is called the Debye-Waller factor. Although such weakening of the scattering signal is the only effect of the thermal motions of atoms on elastic Bragg scattering, it is not the only way to use neutrons to study atomic motions. In fact, one of the great advantages of neutrons as a probe of condensed matter is that they can be used to measure details of atomic and molecular

motions by measuring inelastic scattering in which the neutron exchanges energy with the atoms in a material [Pynn01].

Neutrons can also provide information about the structure at or close to the surfaces of materials, beside the structure of bulk matter as described so far. Neutrons are sensitive to surface structure when they impinge on surfaces at sufficiently low angles. This method is usually referred to as neutron reflectometry.

2.2.2. Neutron reflectivity [Baco01]

The reflection of neutrons (neutron reflectometry) at a surface is very similar to the better known phenomenon of the reflection of light (optical reflectometry). That a beam of neutrons can be reflected from a flat surface just like light was first demonstrated by Fermi and applied for the first time for neutron guides. Light reflected from a thin film may undergo strong interference depending on the wavelength of the light, its state of polarisation, the thickness of the layer and the refractive indices of the media involved.

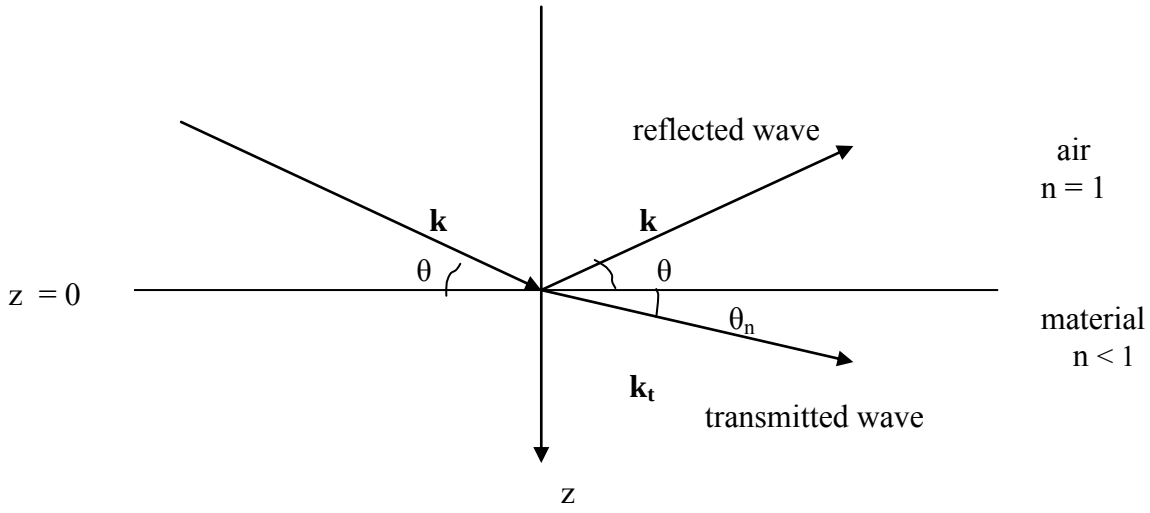

Fig.2.4 Plane wave reflection on a flat surface. The incident, as well as the reflected and transmitted waves are depicted

We assume a neutron beam reflecting on a flat surface with an incident angle theta. This surface (see Fig. 2.4) is defined by the interface between the air (n = 1) and a medium of refractive indices n < 1. For a wavelength lambda, the wavevector is defined by:

$$k = \frac{2\pi}{\lambda} \qquad 2.9$$

The wavevector in the medium of index n is defined by:

$$k_n^2 = k^2 - 4\pi N b \qquad 2.10$$

N is the number of atoms per volume unit and b is the neutron coherent scattering length. The product N·b is called the neutron coherent scattering length density. For a homogeneous medium, the refractive indices n is defined by the ratio of the wavevector in the material to the wavevector in the vacuum [Squi01]:

$$n = \frac{k_n}{k} = 1 - \frac{\lambda^2}{2\pi} Nb \qquad 2.11$$

At the interface between the air and a medium of indices n, Descartes' law can be written:

$$cos\theta = ncos\theta_n \qquad 2.12$$

Total reflection occurs if θ lower than θ_C where θ_C is defined so as $\theta_n = 0$, which means:

$$cos\theta_c = n \qquad 2.13$$

From the equations 2.11 and 2.13 we obtain:

$$1 - (sin\theta_c)^2 = 1 - \frac{\lambda^2}{\pi} Nb \qquad 2.14$$

which is equivalent to:

$$sin\theta_c = \sqrt{\frac{Nb}{\pi}}\lambda = a\lambda \qquad 2.15$$

where the *a* parameter is used to characterise the material.

The projection of the wavevector on the z axes (perpendicular to the surface) is defined as:

$$q = \frac{2\pi}{\lambda} sin\theta \qquad 2.16$$

If the material is made of many layers, each one having an index n_p, the propagation of a plane wave in the layers p and p+1 can be written the following way: [Dail01]

$$\Psi_z(z_p) = A_p \exp(iq_p z_p) + B_p \exp(-iq_p z_p)$$

$$\Psi_z(z_{p+1}) = A_{p+1} \exp(iq_{p+1} z_{p+1}) + B_{p+1} \exp(-iq_{p+1} z_{p+1}) \qquad 2.17$$

where $i^2 = -1$, and A_p and B_p are the incoming and outgoing amplitudes in the layer p respectively. We have also:

$$q_p^2 = q^2 - 4\pi N b_p$$

$$q_{p+1}^2 = q^2 - 4\pi N b_{p+1} \qquad 2.18$$

We can write the continuity conditions at the interface p/p+1:

$$\Psi_z(z_p) = \Psi_z(z_{p+1}) = u(z_{p/p+1})$$

$$\Psi'_z(z_p) = \Psi'_z(z_{p+1}) = u'(z_{p/p+1}) \qquad 2.19$$

The reflectivity in $z_{p/p+1}$ is defined as being the ratio of the intensity of the reflected beam by layer p+1 to the intensity arriving in layer p and is written:

$$R = \frac{|B_p|^2}{|A_p|^2} = \left| \frac{1 - \frac{u'(z_{p/p+1})}{iqu(z_{p/p+1})}}{1 + \frac{u'(z_{p/p+1})}{iqu(z_{p/p+1})}} \right|^2 \qquad 2.20$$

where $u(z_{p/p+1})$ and $u'(z_{p/p+1})$ are functions of $z_{p/p+1}$ and q_{p+1}.

With this equation, we can calculate the reflectivity at the last interface (last layer/bulk), and then recursively calculate the reflectivity at each interfaces, and so obtain the reflectivity of the air/first layer interface.

The reflectivity is analyzed using a formula in which the scattering length density, averaged over dimensions parallel to the surface, is split into thin layers and each density is refined until the measurement can be fitted. This method is called the Parratt formalism [Parr01] and has been programmed into a number of widely available software packages.

2.3. Neutron guides

2.3.1. Why do we need them?

The neutron guides transport slow neutron beams from the reactor core to the instrument and their use was first proposed by Christ, Mayer-Leibnitz and Springer [Chri01], [Leib01]. The neutron guides function in analogy with the optic fibers: a neutron entering the guide tube with an angle of incidence that is smaller than the critical angle corresponding to its particular wavelength will be transported along the tube by multiple total reflection. If a slight curvature is then incorporated in the tube, only those neutrons with the wavelength greater than some minimum value are transported down the tube. The shorter-wavelength fast neutrons, as well as any gammas in the incident beam, pass trough the wall of the tube where they can be absorbed in a suitable shielding. In this way a very clean and highly collimated beam of slow neutrons can be transported to a low-background location far from the primary neutron source where it is then available for neutron scattering experiments [Brue01].

2.3.2. The principle

Neutrons as particle waves follow the same law for the total reflection as light waves. To construct a neutron mirror or neutron guide the first question to solve was to find a medium for neutrons, which is optically "thinner" than vacuum. This is the case for all media with a positive scattering length b (see equation 2.11). Nickel exhibits one of the largest scattering lengths, i.e. exhibits one of the largest critical angle and is therefore ideally suited as mirror

material in neutron guides. The limiting angle for *total reflection* of a neutron mirror is much smaller than for light in the optical glass fiber; it also depends on the neutron wavelength. A rough formula for the limiting angle for neutron total reflection at a Nickel surface is 1° times the wavelength of neutrons in nanometer, which results for the wavelength of 0.5 nm to approximately 0.5°. This small angular range for the total reflection reduces the efficiency in comparison to an optical glass fiber, but it still allows transporting neutrons to a remarkable distance up to 10 - 100 meter. The acceptance angle of neutrons is improved by using so-called *super-mirrors*, with limiting angles larger by factors 2 - 3 as compared to critical angle of Ni [Meze01]. The factor by which the critical angle is increased in comparison to the critical angle for natural Ni is called m. Super-mirrors are using layer systems with alternating layers of for example Ni and Ti, with a maximum in the difference of the respective scattering length. The variation in thickness d of the layers is such that a continuum of Bragg reflections is added on top of critical angle, thereby increasing the angle of reflection.

In order to transport thermal or cold neutrons under small glancing angles almost loss-free from the neutron source to the distant neutron instrument neutron guides [Sear01] are used. Typical neutron guides have lengths of up to 100m and rectangular cross-sections of area ~100cm^2. At first neutron guides were fabricated from glass plates coated on their inside with a thin layer of natural Ni or enriched ^{58}Ni. In such guides neutrons are transported by total reflection on the inner guide walls, with typical neutron reflection losses of 1% per bounce.

Starting about twenty five years ago [Leib01], [Brue01] neutron guides equipped with 'supermirror' coatings were developed. A neutron supermirror [Boen01] consisting of typically 100 double layers of Ni/Ti of varying thickness typically doubles the maximum permitted angle of neutron reflection. However, neutron reflection losses are stronger for a supermirror than for a conventional nickel mirror, typically 10% per bounce. Therefore, very long supermirror neutron guides must be of the 'ballistic' type in order to bring benefits [Boen02]. A neutron guide is called ballistic when its cross section varies along its length such as to minimize transport losses within the guide. In order to suppress a background due to a direct beam of gamma rays and fast neutrons, the guide is tightly surrounded by a combined shielding consisting of polyethylene, bor and lead. Unlike thermal neutrons, gamma rays and fast neutrons are not subject to reflections from the Ni coating and penetrate the guide walls. In the shielding around they are scattered and absorbed and only collimated thermal neutrons pass through. Therefore, a biological shielding, formed by boron-doped polyethylene and lead bricks, is built along the whole guide.

The quality of a neutron guide is influence by the quality of the supermirrors that builds it. There are a couple of parameters that influence the quality of a supermirror (Ni/Ti multilayers), in particular the number of bilayers, possibilities for isotope substitutions, interfacial roughness and other imperfections. [Meze02]

Therefore there is the requirement for adding more and more bilayers in order to reach very high critical q values [Hayt01]. This approach is technically limited due to the following reasons:

i) With an increasing number of layers, quality correspondingly suffers due to the increasing amplification of interface roughness.

ii) Diffusion plays an increasing role especially for high-m supermirrors. The smallest single layer thickness of an m = 4 supermirror is about 40 Å. For metallic multilayers, it is very difficult to achieve rms-roughness values less than 5 Å.

iii) The technical demands and fabrication time needed for depositing high-m supermirrors is roughly proportional to the number of layers; therefore, the cost for high-performance supermirror coatings rises very steeply.

iv) The control of mechanical strain becomes more and more difficult for high-m supermirrors having very high total film thickness, e.g. approximately 35,000 Å in the case of m = 3.5 mirrors. Associated with this is the danger of mechanical failure of the films (cracks or extensive peeling).

Enhancement of the critical q-value of a supermirror and its reflectivity function may be achieved by artificially increasing the contrast in scattering length density, $\Delta N \cdot b$, between the materials constituting the mirror. There are cases in which natural Ni and Ti are substituted by more favourable isotopes or alloyed with other elements, for example hydrogen or carbon [Ande01] .

In order to achieve high reflectivities at large angles it is necessary to grow multilayers with very smooth and sharp interfaces on large and smooth substrates. The major problem with this large m mirrors is the fact that the total thickness of the coating becomes very large. Therefore the force of coating on the substrate exceeds the mechanical strength of the glass and gives rise to fractures leading even to coatings detaching from the surface [Boen03].

As a conclusion, the losses in reflectivity are due to:

- Absorption due to the enormous total thickness of approximately 50.000 Å
- Incoherent scattering (playing an important role)
- Roughness between the interlayers (10% of individual layer thickness), plus surface roughness of the substrate

• Interdiffusion among the layers becoming increasingly more important with decreasing layer thickness

• Limited coherence due to deviations from design layering

• Small-angle scattering on grain structure

By overcoming the losses stated above, supermirror performances could be enhanced significantly. Supermirror coatings have reached nowadays an m factor of 7.

The neutron reflectivity phenomenon offers us therefore the possibility to transport neutrons using neutron guides. The main advantage of using a neutron guide tube is its capability to transport a neutron beam easily without significant intensity loss, that is conserving the phase space density of neutrons, to a place far distant from the neutron source where a wider area with lower background can be prepared for beam utilization.

2.4. Recent developments

Current trends in condensed matter physics evolve towards the investigation of strongly correlated electron systems. They include materials that exhibit quantum phase transitions [Stoc01] driving exotic phases, multiferroic materials [Sen01], low dimensional magnetism [Thie01] and high-temperature superconductors [Chan01]. However, the need of low temperatures in the mK-regime, high magnetic fields and hydrostatic pressures, permanently pushes the experimental requirements to new limits, as only small samples can be used under these conditions. Therefore, there is a continuous demand for higher neutron intensities at the sample position that is required to answer nowadays scientific questions. Neutron optics has been constantly developed and upgraded, improving both neutron flux and resolution, in order to meet these experimental challenges. Major developments are the installation of supermirror guides [Wagn01], [Ibbe01] delivering a high neutron flux to the experimental position, and the virtual source concept [Pint01], [Kuld01] that in combination with large focusing monochromator and analyzer arrays [Rist01], [Nune01], [Sche01], [Link01] allows to increase the energy resolution of the spectrometer while simultaneously focusing the neutron beam on small samples and reducing the background.

The use of focusing guides is therefore a well-established technique to significantly increase the neutron flux for the investigation of small samples or samples subject to extreme conditions such as pressure or high magnetic field. In chapter 2.4.1 are presented possible ways of focussing a neutron beam, while in chapter 4 are illustrated simulation techniques and results for reaching the sub-mm range.

2.4.1. Focusing neutron guides

2.4.1.a. Focusing principles

A bent guide tube instead of a straight guide transmits preferentially those neutrons with a wavelength longer than the characteristic wavelength given by the geometrical configuration of the guide, which reduces the components of shorter-wavelength neutrons and gamma rays unnecessary for the neutron optics and slow neutron scattering experiments [Mild01].

This cutoff wavelength depends on the guide curvature and width. If we consider a curved guide with the radius of the outer wall ρ and the distance between the inner and the outer wall (width) a (see figure 2.5), this curved guide has a characteristic angle: $\Psi_c = \sqrt{2a/\rho}$

This is the minimum angle that the guide subtends (in the horizontal plane) in order to get out of the direct line-of-sight. This curved guide has a cutoff wavelength $\lambda_c = \Psi_c \cdot \lambda/\theta_c$, with the critical angle defined by formula 2.15.

All reflections are assumed to be specular with reflectivity 1 up to this defined critical angle θ_c and with reflectivity 0 above θ_c.

There are two types of reflections that appear in bent guides:

- Zig-zag reflections (large θ_a) (red line in figure 2.5) – reflections on both walls
- Garland reflections (small θ_a) (blue line in figure 2.5) – reflections from outer wall, never touching the inner wall

If the maximum reflection angle allows only Garland reflections near the outer wall, then the guide is not efficiently ~~–~~filled". If $\theta_a \approx \theta_i$ (the incident angle) the filling of the guide will be fairly isotropic (many reflections).

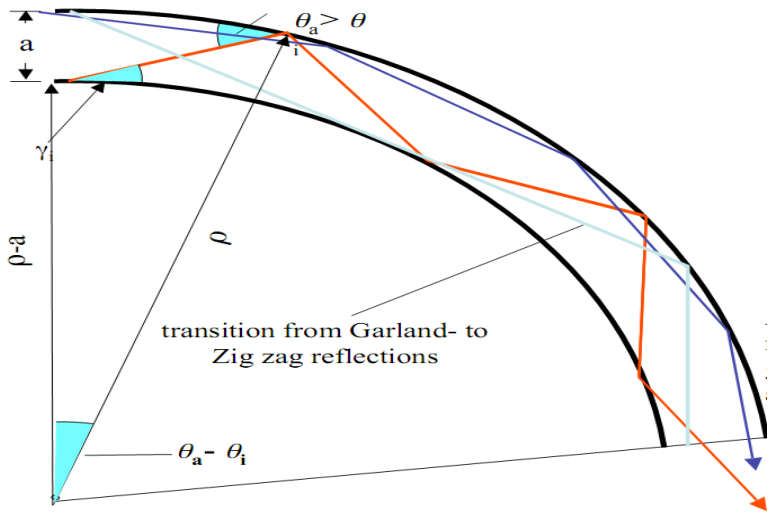

Fig. 2.5. Reflection that occur in a bent guide [Chup01]

Beam focusing can be achieved by total reflection from a curved surface. [Ande01]

Same as in optics, neutron focusing can be achieved with parabolic, elliptic mirrors or combinations of these two.

An ellipse is a two dimensional closed curve that satisfies the equation [Clyn01] :

$$\frac{x^2}{a^2}+\frac{y^2}{b^2}=1 \qquad 2.20$$

The curve is described by two lengths, a and b. The longer axis, a, is called the semi-major axis and the shorter, b, is called the semi-minor axis. The parameters of an ellipse are also often given as the semi-major axis, a, and the eccentricity, e:

$$e=\sqrt{1-\frac{b^2}{a^2}} \qquad 2.21$$

or a and the flattening, f:

$$f=1-\frac{b}{a} \qquad 2.22$$

In the above common equation two assumptions have been made. First that the origin of the x-y coordinates is at the center of the ellipse and second that the longer axis of the ellipse is along the x-axis.

The convention that the semi-major axis is the x-axis will be used throughout. In this technical note both conventions for the coordinate system origin will be used. The equations with the origin at the center of the ellipse and at one focus are shown. The two focus points are located along the x-axis (the longer axis) at a distance of:

$$c=\sqrt{a^2-b^2} \qquad 2.23$$

from the center. There are two, one on each side (at ±c, marked with F1 and F2 in figure 2.6.).

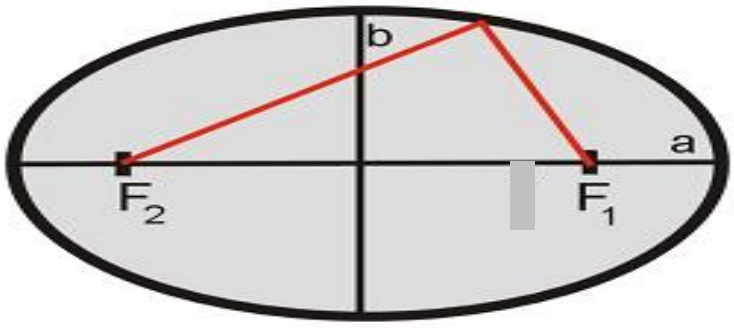

Fig. 2.6. Ellipse with important points

It can be mathematically proved that light ray that passes through one focus point of an elliptical mirror is reflected in such direction that it passes through the second focus point. This property is exploited for the elliptical neutron guide construction.

Consider a curved mirror surface that is constructed as follows. Start with a curve, denoted by y(x) in the x–y plane, that is symmetrical under a reflection through the y axis; i.e.

$y(-x) = y(x)$.

The y-axis is thus the symmetry-axis of the two-dimensional curve y(x). The three-dimensional curved mirror surface is then obtained by rotating the curve about the y-axis, thereby producing a "surface of revolution" corresponding to the surface of the mirror. The projection of this surface onto the x–y plane yields the original curve y(x).

Due to the symmetry of the three-dimensional surface, it is sufficient to examine the light rays propagating in the x–y plane. Consider two parallel light rays that strike a curved mirror surface.

The first ray is initially propagating in a direction parallel to the y-axis. It then strikes the mirror with an angle of incidence θ with respect to the normal to the curve y(x) at the point P, labeled by coordinates (x, y). Using the law of reflection, the angle of reflection of the resulting reflected ray is equal to the angle of incidence, θ. The second ray heads down the y-axis, strikes the mirror at O and then is reflected back up the y-axis. Both reflected rays intersect at the focal point F, labeled by coordinates (0, f), as shown in the figure 2.7. [Focu01].

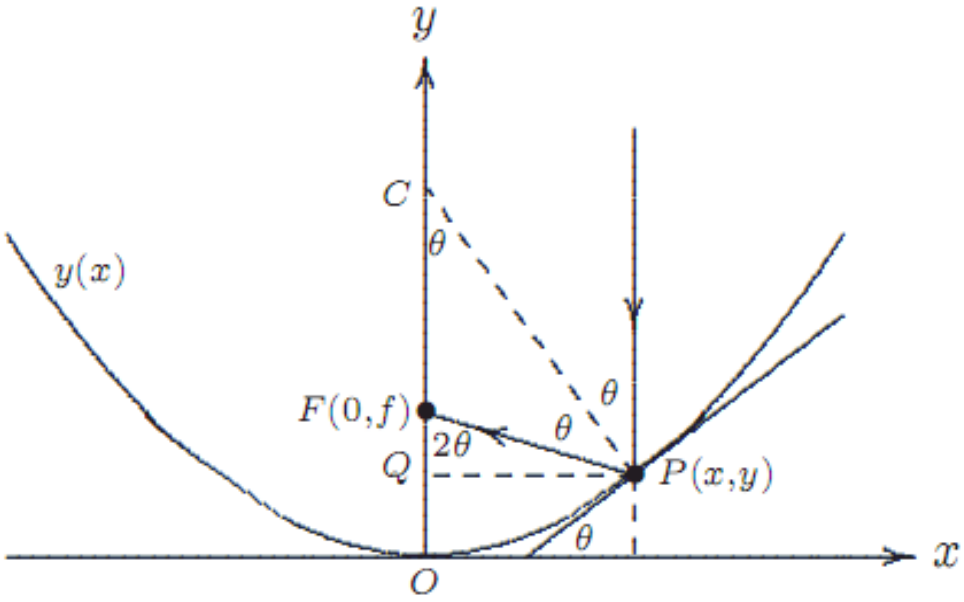

Fig.2.7. Parabolic focusing mirror, with focal point F and center C. P is a point belonging to the parabola where a tangent is drawn

The tangent line to the curve at P is explicitly shown above. Simple geometrical considerations imply that the angle the tangent line makes with the x-axis is also given by θ. Thus,

$$f = y + \frac{x}{\tan 2\theta} \qquad 2.24$$

Using the identity below it follows:

$$\tan 2\theta = \frac{2\tan\theta}{1-\tan^2\theta}$$
$$f = y + \frac{x(1-\tan^2\theta)}{2\tan\theta} \qquad 2.25$$

For a spherical mirror, the curve shown above is part of a circle of radius r. Moreover, C is the center of the circle, since the line segment CP is perpendicular to the tangent line at point P. Hence the length of CP is equal to r. Note that the triangle CFP is isosceles, hence the length of the sides FP and FC are equal. Denote this length by a. Then by the law of cosines:

$$r^2 = 2a^2[1-\cos(\pi-2\theta)] = 2a^2[1+\cos(2\theta)] = 4a^2\cos^2\theta \qquad 2.26$$

Finally, noting that f + a = r, we end up with:

$$f = r(1-\frac{1}{2\cos\theta}) \qquad 2.27$$

This last equation shows that there is no unique focal point, since f depends on the angle θ. However for small θ values we can use the approximation:

$$\cos\theta \cong 1-\frac{\theta^2}{2} \cong 1,\ for\theta << 1 \qquad 2.28$$

in which case, we can approximate:

$$f \cong \frac{1}{2}r,\ for\theta << 1 \qquad 2.29$$

That is, for small angles (or equivalently for a mirror whose length is much smaller than the radius r), the location of the focal point F is independent of the angle of incidence, which means that all parallel rays that strike the spherical mirror (at small angle) pass through the focal point F.

Consider a parabola that is described by the equation:

$$y = Ax^2 \qquad 2.30$$

for some positive constant A. Then dy/dx = 2Ax. Inserting these results into eq. 2.24 gives the following result for the focal length:

$$f = Ax^2 + \frac{x(1-4A^2x^2)}{4Ax} = \frac{1}{4A} \qquad 2.31$$

Thus, indeed the focal length f is independent of x. That is, all light rays that are initially parallel to the y-axis (i.e. the symmetry axis of the parabola) pass through the focal point F after reflecting off the mirror. No small angle approximation is necessary in this case.

The requirement that the initial light rays should be parallel to the symmetry axis of the parabola is critical. One can show that if the initial light rays are parallel to each other but are not parallel to the symmetry axis of the parabola (sometimes called off-axis parallel rays), then the reflected rays are not focused to a unique focal point.

Wolter[Asch01] in 1951 analysed mirrors which have concentric figures of revolution, i.e. paraboloids, hyperboloids and ellipsoids. He showed that in order to achieve a true image over an extended field of view the x-rays have to undergo two successive reflections from either a paraboloid/hyperboloid or paraboloid/ellipsoid combination which are mounted in a coaxial and confocal arrangement. Fig. 2.8. is a schematic of the three configurations Wolter studied in detail and which are known as the Wolter type I, type II and type III systems. For each of the three configurations the two mirrors are arranged coaxially and they have a coincident common focus which makes the system focus. The Wolter type I and Wolter type I1 configurations both utilise a paraboloid and a hyperboloid. Within the type I system reflection occurs on the internal surfaces of each mirror; the reflection is off the external surface of the hyperboloid for the type II systems. In type III systems the incident rays are first reflected from the external surface of a paraboloid and then focused by the internal surface of an ellipsoid.

The main difference between the three systems is the ratio of focal length to total system length. The focal length of the type 1 system is given by the distance from the paraboloid/hyperboloid intersection plane to the focus. Therefore the system length is larger than the focal length by the length of the paraboloid. The type II has a focal length which is larger and can exceed the system length substantially. The type III system has the shortest focal length of all three configurations. All three systems are equivalent in optical performance with respect to the Abbe sine condition. The principal surface is not a sphere as required but a paraboloid which is well approximated by a sphere in the angular region close to the centre of the field of view. Wolter showed that the sine condition can be approximately fulfilled also for larger apertures by introducing further hyperboloids, but only for an even number of mirrors in total.

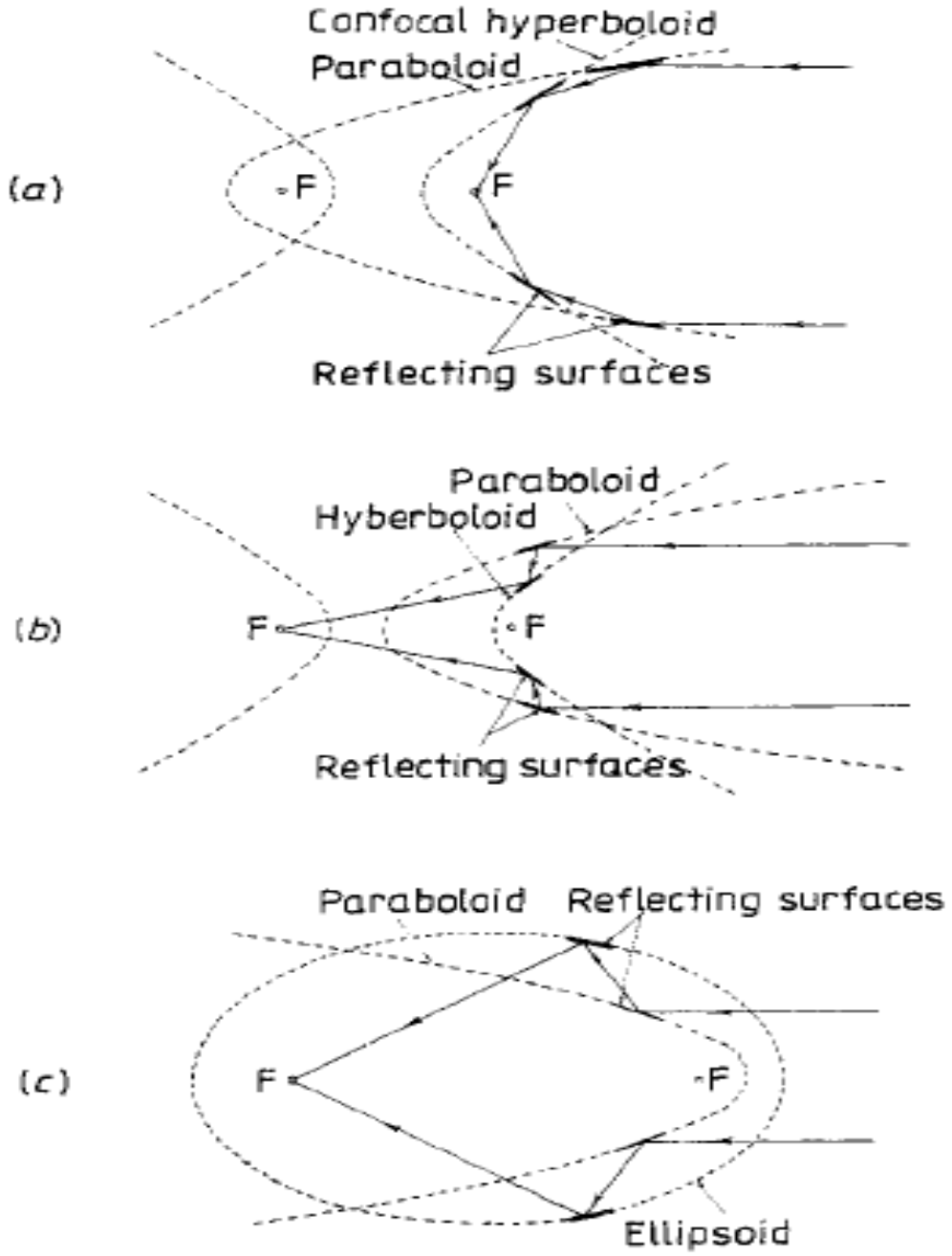

Fig.2.8 Schematic of the different Wolter telescopes called type I, type II and type III from top to bottom

The collecting area can be enlarged by nesting additional Wolter telescopes in the interior. Each system acts independently from its neighbouring ones. All of the systems are coaxial and have a common system focus.

A new concept of neutron focalisation on SANS spectrometers using a combination of curved super mirrors (SM) can be proposed. The aim is to design a focusing system which is achromatic and has no absorption. The proposed design combines advanced neutron optical element such as parabolic and elliptic SM. Figure 2.9. presents the device design. A parabolic SM focuses the beam from the exit of the guide to make it a point source at its focal point *Fp*.

An elliptic SM with its primary focal point (*Fe1*) lying at the same position as *Fp* images *Fe1* to its secondary focal point *Fe2* according to the properties of ellipses. Now, if a sample is placed after the elliptic SM and a detector is located at *Fe2*, then we build a focusing system with working on reflection (around 85% for m = 3 SM) and achromatic. Therefore, SANS instruments could benefit of this technique in terms of flux at the sample.

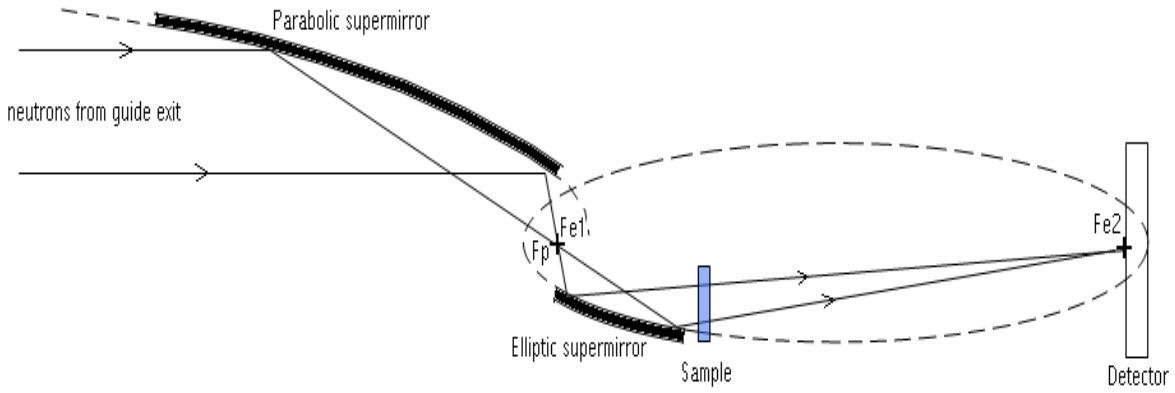

Fig. 2.9. Design of the focusing device with a combination of parabolic and elliptic supermirrors

2.4.1.b Focusing guides

The most recent developments have shown that elliptic guide systems can be used to focus neutron beams while simultaneously reducing the number of neutron reflections, hence, leading to considerable gains in neutron flux. Parabolic and elliptic guides can focus the beam in a single point beyond the guide exit with well defined beam characteristics and a gain factor in intensity of over 30 compared to straight guides [Scha01]. They can find applications in elastic and inelastic neutron scattering as well as for neutron radiography and tomography.

It has been recently shown [Jano01] that the focusing performance of the elliptic nose crucially depends on its total length: for large length of the elliptic nose the guide behaves even worse than a straight guide as it leads to a large number of zig-zag-reflections and therefore the neutron beam has the smallest width and highest intensity near to the guide exit than at the position where the neutron beam is expected to be optimally focused.

For small values of the length of the elliptic guide the number of reflections is essentially identical to a straight guide and only the very last reflection is used to focus the beam onto the focal spot. This leads to an improvement of the focusing performance for small lengths.

The conclusion is that the increased gain can easily be understood according to Fig. 2.10. The finite divergence of the neutron beam broadens the spatial distributions of the neutrons over the length of the gap (G). The increased entrance width of the elliptic guide (Win) therefore allows to minimize neutron losses due to this beam broadening. The intensity gain as a function of linw can be understood in terms of a virtual point source generated by the straight guide section in front of the gap. The beam image at the exit of the straight guide can be approximately mapped to a point if we again consider the divergence of the beam.

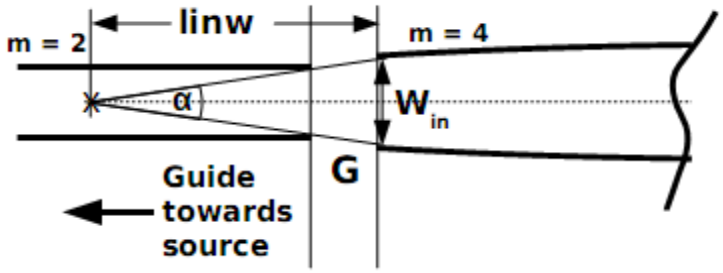

Fig. 2.10. The entrance of the elliptic section can be used to minimize losses after a gap (G) in the neutron guide. This is achieved by taking into account the divergence of the neutron beam enlarging via an enlarged entrance width W_{in} to the elliptic section. Further the beam image of the straight guide section in front of the gap can be mapped to a virtual point source (X) inside the guide. The distance linw between the focal spot of the ellipse and the guide entrance needs to be adjusted in such a way that the focal spot is situated at the position of this virtual point source.

In comparison to an elliptic guide that maps the virtual source situated at l_{inw}, a parabolic guide will focus better a parallel beam with lower divergence into a small beam in focal point.

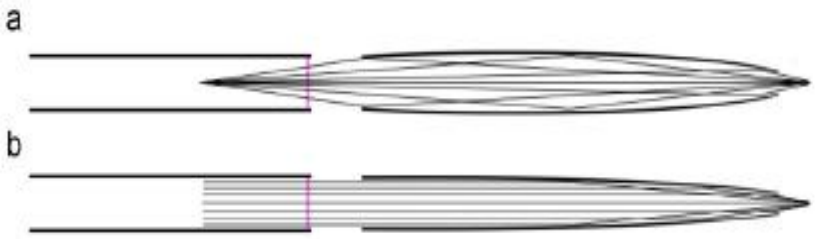

Fig. 2.11. Schematic focusing design of (a) fully elliptic and (b) fully parabolic guides in the horizontal plane.

The better performance of the parabolic versus the elliptic focusing concept for an instrument at the end of a neutron guide can be understood by the following reason: the parabolic guide focuses neutrons with small divergence from the whole entrance window into its focal point,

whereas the elliptic guide focuses neutrons with higher divergence from outer parts of the entrance window into its focal point. This can be seen in the schematic drawings of Fig. 2.11 (a,b). At larger distances from the reactor, the neutron intensity provided by the guide is dependent on the neutron divergence. The intensity is strongly reduced for neutrons with higher divergence due to the reflection losses in the preceding neutron guide. This reduction of intensity for neutrons with higher divergence becomes especially significant for higher neutron energies. Since the elliptic concept also depends on focusing neutrons out of these high-divergence regimes into its focal point, it has a clear disadvantage with respect to the intensity, especially for higher neutron energies. In contrast, the parabolic concept basically focuses neutrons with low divergence (from the regime with highest flux in the intensity-divergence distribution) into its focal point [Koma01].

Therefore the optimal shape of the focusing guide has to be chosen accordingly to the properties of the beam in front of the focusing optics and to the desired properties of the beam after the guide.

Also the use of focusing guides opens wide possibilities to adapt the phase space of neutron beams to match the needs of neutron beam lines and to transport the neutrons efficiently from the moderator to the sample and detector.

The new focusing techniques can find applications in triple axis, time of flight and spin-echo spectroscopy as well as for imaging with neutrons.

2.4.2. Adaptive optics

The aim of the implementation of adaptive focusing neutron optics is to adapt the beam size as well as the beam divergence to the sample. By means of actuators, the curvature of the guide can be adjusted independently and therefore the focal length of the device can be varied. It is known that a focused neutron beam has many advantages for the investigation of small samples in the mm or sub mm range. The aim of this focussing is to obtain a focal point in the sub mm range in order to perform elastic and inelastic scattering on very small samples. Another important aspect is to reduce the scattering background in experiments under extreme conditions as in high magnetic fields or high pressures so that the beam illuminates only the sample. In the same way a focusing device can be used to collect the scattered neutrons after the sample.

The idea behind adaptive optics is to give the possibility to align the focal point on tiny samples or to adapt the beam size and the divergence of the neutron beam to the sample. This

is possible by changing the curvature of the elliptic or parabolic guide by means of actuators independently in x and y direction so that the focal length of the device can be changed. We consider as an example a parabolic guide whose curvature can be modified by means of actuators (fig. 2.12). Fig.2.12 shows the principal design of an adaptive parabolic focusing guide to adjust the focal spot of the focusing guide thus changing the flux and the divergence of the neutron beam at the sample position.

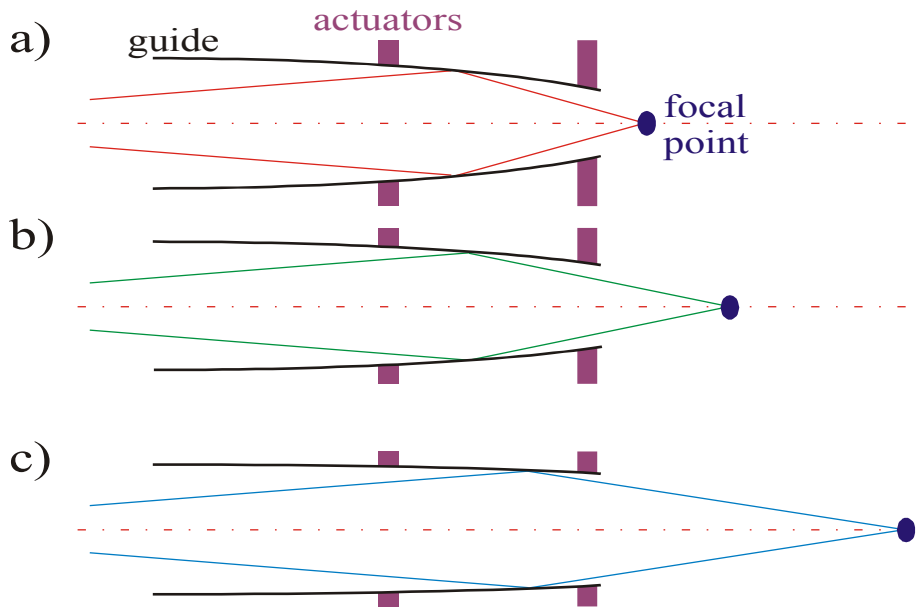

Fig.2.12. Principle of adaptive optics. By means of actuators the focal length of the ellipse can be changed.

As shown in Fig. 2.12 a, by adjusting the end of the guide we increase the curvature of the guide, therefore we decrease the focal length thus obtaining a beam with a small width in the focal point and an increased divergence. A decrease of the curvature leads to an increased focal length (Fig. 2.12 c) with an increased width of the beam in focal point and a decreased divergence.

If we consider a white beam, each wavelength will be focused at a specific point f (the dependency of the position of the focal point with the wavelength is presented in chapter 5). If we consider now a monochromatic beam and we adapt the curvature of the guide with respect to the wavelength we can obtain that each wavelength will be focused at the same point. As an example we have chosen two wavelengths 1.5 Å in Fig. 2.13 upper part and 12 Å in Fig. 2.13 lower part. The two wavelengths are focused onto the same position because of the change in curvature in the reflecting guide. Monte Carlo simulations for the realization of such a device and the corresponding prototype will be presented in chapter 5.

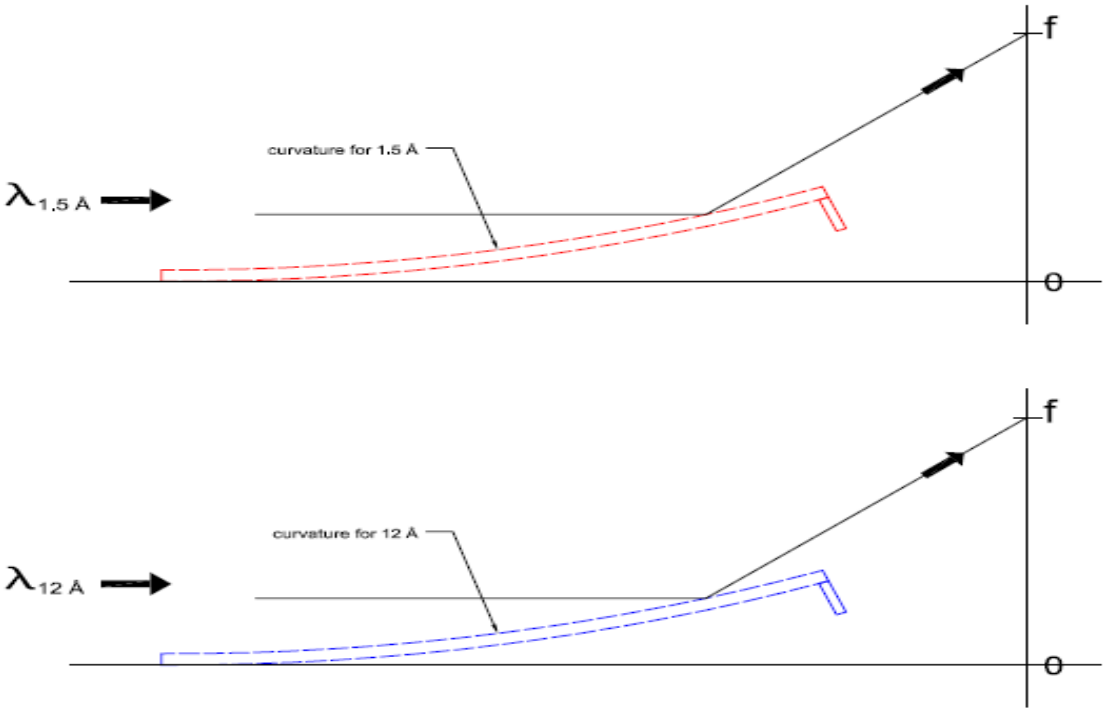

Fig.2.13 Schematic of adaptive optics. Due to the change in curvature both wavelengths are focussed onto the same position f.

3. Monte Carlo simulations

In this chapter are presented the basics of Monte Carlo simulations in comparison with deterministic methods. The Monte Carlo simulation program McStas is described, starting from the way components are defined to construct an instrument up to the way neutron reflections are treated in the program..

3.1. The Monte Carlo method

Neutron histories are difficult to determine because of the large number of different interactions possible in materials. Techniques for calculating the behavior or transport of neutrons and gamma rays in such circumstances are important for the design of instrument the interpretation of measurements, and the development of shielding configurations [Muhl01]. Two techniques for calculating the transport of neutrons in matter are described briefly in the following.

a)Monte Carlo Techniques

The probabability of a neutron interaction occurring is an important feature in the description of neutrons traveling through matter. Instead of trying to predict what an individual neutron may do, one can use procedures to predict what fraction of a large number of neutrons will behave in some manner of interest. Calculation techniques that, in simplistic terms, predict neutron events with ~~"r~~olls of dice" (actually the generation of random numbers in a computer) are called Monte Carlo methods. The response of an assay system can often be calculated from the transport of many individual neutrons, despite the inclusion of a few improbable neutron histories that deviate drastically from the average behavior.

The Monte Carlo method can allow a detailed three-dimensional geometrical model to be constructed mathematically to simulate a physical situation. A neutron can be started at a selected location with a certain energy and direction. It travels distances that are consistent with the mean-free-paths in the materials, with random variations from the expected mean.

At the end of each step in the neutron's path, a decision maybe made to simulate a certain interaction, with the decision based on the cross section for the interaction with that material at that neutron energy. If an interaction is selected, the results of the interaction are simulated and its consequences followed. Eventually, a point is reached where no further interest in the neutron exists and its history is terminated. This might occur with the escape of the neutron or its moderation to very low energy. The neutron might be absorbed followed by the emission of a gamma ray of no interest or it might undergo a multiplication event. If a multiplication event occur the histories of the new neutrons are followed. In principle, the history of a simulated neutron is one that might actually occur with a real neutron.

By repeating this procedure for many thousands of neutrons and by keeping tallies of how many enter the detector region, how many cause fissions, how many escape through a shielding or whatever else is of interest, an average behavior and its uncertainty are gradually deduced. Many specialized techniques may be used to get good average values with the fewest number of neutrons, but there are cases where even a fast computer cannot provide enough histories within the constraints of time and budget. Nonetheless, Monte Carlo techniques provide essential assistance in design work by closely modeling the actual geometry of a problem and by having imaginary neutrons that simulate the motions and interactions of real ones.

b) Discrete Ordinates Techniques

Analytical transport equations exist that describe the exact behavior of neutrons in matter. However, only approximate numerical solutions to these equations can be obtained for complicated systems. Procedures for obtaining these numeral solutions are classified as discrete ordinates techniques. Some important differences distinguish discrete ordinates techniques from Monte Carlo techniques. Only one- or two-dimensional geometries are generally practical with a discrete ordinates process, and the neutrons are considered to be at discrete locations instead of moving freely through a three dimensional geometry. In a two dimensional discrete ordinates case, for example, it is as if the surface material were covered by a wire mesh and the neutrons existed only at the intersections of the wires. Furthermore, the energy of a neutron at any time must be selected from a finite set, in contrast to the continuously varying energy of a neutron in the Monte Carlo method.

Despite these disadvantages, discrete ordinates techniques can produce useful results in many cases.

Monte Carlo can be used to duplicate theoretically a statistical process (such as the interaction of nuclear particles with materials) and is particularly useful for complex problems that cannot be modeled by computer codes that use deterministic methods. The individual probabilistic events that comprise a process are simulated sequentially. The probability distributions governing these events are statistically sampled to describe the total phenomenon. In general, the simulation is performed on a digital computer because the number of trials necessary to adequately describe the phenomenon is usually quite large. The statistical sampling process is based on the selection of random numbers—analogous to throwing dice in a gambling casino—hence the name ―Monte Carlo.‖ In particle transport, the Monte Carlo technique is pre-eminently realistic (a numerical experiment). It consists of actually following each of many particles from a source throughout its life to its death in some terminal category (absorption, escape, etc.). Probability distributions are randomly sampled using transport data to determine the outcome at each step of its life.

The neutron ray-tracing Monte-Carlo method has been used widely for e.g. guide studies, instrument optimization and design. Most of the time, the conclusions and general behaviour of such studies may be obtained using the classical analytical approaches, but accurate estimates for the flux, the resolutions, and generally the optimum parameter set, benefit advantageously from MC methods. Recently, the concept of virtual experiments, i.e. full

simulations of a complete neutron experiment, has been suggested as the main goal for neutron ray-tracing simulations [Mont01].

3.1.1. Monte Carlo method versus deterministic methods [Hend01]

Monte Carlo methods are very different from deterministic transport methods. Deterministic methods, the most common of which is the discrete ordinates method, solve the transport equation for the average particle behavior. By contrast, Monte Carlo obtains answers by simulating individual particles and recording some aspects (tallies) of their average behavior. The average behavior of particles in the physical system is then inferred (using the central limit theorem) from the average behavior of the simulated particles. Not only are Monte Carlo and deterministic methods very different ways of solving a problem, even what constitutes a solution is different.

Deterministic methods typically give fairly complete information (for example, flux) throughout the phase space of the problem. Monte Carlo supplies information only about specific tallies requested by the user.

When Monte Carlo and discrete ordinates methods are compared, it is often said that Monte Carlo solves the integral transport equation, whereas discrete ordinates solves the integro-differential transport equation. Two things are misleading about this statement. First, the integral and integro-differential transport equations are two different forms of the same equation; if one is solved, the other is solved. Second, Monte Carlo ―solves" a transport problem by simulating particle histories.

A transport equation need not be written to solve a problem by Monte Carlo. Nonetheless, one can derive an equation that describes the probability density of particles in phase space; this equation turns out to be the same as the integral transport equation.

Without deriving the integral transport equation, it is instructive to investigate why the discrete ordinates method is associated with the integro-differential equation and Monte Carlo with the integral equation. The discrete ordinates method visualizes the phase space to be divided into many small boxes, and the particles move from one box to another. In the limit, as the boxes get progressively smaller, particles moving from box to box take a differential amount of time to move a differential distance in space. In the limit, this approaches the integro-differential equation, which has derivatives in space and time. By contrast, Monte Carlo transports particles between events (for example, collisions) that are separated in space

and time. Neither differential space nor time are inherent parameters of Monte Carlo transport. The integral equation does not have terms involving time or space derivatives.

Monte Carlo is well suited to solving complicated three-dimensional, time-dependent problems. Because the Monte Carlo method does not use phase space boxes, there are no averaging approximations required in space, energy, and time. This is especially important in allowing detailed representation of all aspects of physical data.

3.1.2 .McStas simulation program [Kjae01]

The software package McStas is a tool for carrying out Monte Carlo ray-tracing simulations of neutron scattering instruments with high complexity and precision. The simulations can compute all aspects of the performance of instruments and can thus be used to optimize the use of existing equipment, design new instrumentation, and carry out virtual experiments for e.g. training, experimental planning or data analysis.

In the McStas formulation of a neutron scattering instrument, all objects apart from the neutron are referred to as components. This includes for instance:

- **Source:** The exit of a neutron production facility, where neutrons of certain velocities are emitted into some portion of space
- **Monochromator/Analyzer:** crystals used to select a neutrons of a single wavelength to probe the sample with (monochromator) or to analyze (analyzer)
- **Sample:** An object altering the neutron physical properties in some sense, examples used here are
    a. Vanadium. Scatters incoming neutrons incoherently
    b. Powder2. Can be thought of as a large number of crystals, each scattering neutrons according to the Bragg law, thereby producing two concentric Debye-Sherrer cones. This sample also has the posibility of adding inchoherent, eleasticaly scattered neutrons.
- **Monitors:** Objects *monitoring* or registering neutron characteristics. In the exercises below are used different types of detectors or monitors:
    1. Monitor. Single monitor, detecting the number of neutrons flying through a plane. (User defined opening size)
    2. PSD_monitor. Square monitor, detecting the number of neutrons passing through a plane, divided into pixels. square regions of a plane. (User defined resolution and opening size)

3. PSD_monitor_4PI. As PSD_monitor but shaped like a sphere.
4. L_monitor. Wavelength monitor, measuring the different wavelengths of the passing neutrons. (L is for lambda)
5. Monitor_nD. General monitor for detecting all sorts of physical properties of the neutron. In our cases used with options

    - 'single' - as PSD_monitor but only one small square

    - 'banana' - as PSD_monitor but shaped like a curved, horizontal band

- **Collimators:** Devices controling the direction and divergence of the neutron ray.

- Collimator_linear A series of parallel absorbing neutron plates that limits the beam divergence.

In short, the core of the McStas system is a precompiler. From a user-provided instrument description, components are assembled into a single piece of ansi-c code. Using a compiler, e.g. gcc, the c code is compiled into an executable program which can be run on your computer. Optionally, the program takes input arguments to tune the setup of your instrument/simulation.

Important details that have to be followed while using McStas:

- **Neutron histories/Intensities:** McStas simulates neutron histories rather than direct neutron counts, i.e. when a Monte Carlo choice is made in a given component (e.g. a random number is generated to decide a new direction of the neutron ray), the neutron *weight factor* is adjusted accordingly. As you may have guessed already, the weight factor is actually a probability of observing a neutron of the given behaviour. The transition to direct neutron intensites is made by adjusting the initial neutron weight of the source component, giving the absolute flux of neutrons emitted in one second. This means that the intensity of the neutron beam at a given position is the initial neutron weight multiplied by the product of all the Monte Carlo weight factors occuring from the source to the given position.

- **3D space:** The 3D space in which the instrument is defined, usually has a single component which is placed absolutely in space, e.g. at (0,0,0). All other components can be placed relative to this component.

- **Changing coordinate system:** Each component has its own local coordinate system. As the neutron travels from one component to the other, the local component coordinate system changes. The definition is that z is the direction toward the next component, and that the y-direction is vertical.

- **Component order matters:** It is important to understand that McStas is component order dependent. The basic idea is to follow the neutron as it travels from one component to the

next in the instrument description. This means that if you place one component *geometrically* before another component, but *orderly* after the other component, neutrons may never reach your 'first' component. This means that some designs can be difficult to achieve, though generally a solution can be found.

- **Use Arm()'s:** The Arm() component is very good for defining changed orientation of the instrument, e.g. for axis turning points etc. Placing many Arm()'s will improve future flexibility of your instrument.
- **Use PSD_monitor()'s:** The PSD_monitor() component is a **p**osition **s**ensitive **d**etector. This component can be used to image the shape of your beam as it travels through the instrument. This is very useful for debugging purposes. Other monitors, for instance wavelength monitors can also be useful.

Our main interests during the Monte Carlo simulations were the neutron guides and the PSD monitors together with Divergence Monitors for characterizing the beam at the sample position. For implementing a neutron guide in the program one needs to define first the reflectivity curve. For this an empirical formula derived from the experimental data is used:

$$R = \begin{cases} R_0, \ Q \leq Q_C \\ \frac{1}{2} R_0 \left(1 - tanh\left[\frac{Q - mQ_C}{W}\right]\right)(1 - \alpha(Q - Q_C)), \ Q > Q_C \end{cases} \quad 3.1$$

Here Q is the length of the scattering vector defined by:

$$Q = \left|\boldsymbol{k_i} - \boldsymbol{k_f}\right| = \frac{m_n}{\hbar}\left|\boldsymbol{v_i} - \boldsymbol{v_f}\right| \quad 3.2$$

m_n being the mass of the neutron.

The number m in the above equation is a parameter determined by the mirror materials, the bilayer sequence, and the number of bilayers (and was treated in chapter 1). As can be seen, $R = R_0$ for $Q < Q_c$, where Q_c is the critical scattering wave vector for a single layer of the mirror material. At higher values of Q, the reflectivity starts falling linearly with a slope α until a ”soft cut-off” at $Q = m \cdot Q_c$. The width of this cut-off is denoted W. See the example reflection curve in figure 3.1.

It is important to notice that when $m < 1$, the reflectivity remains constant at $R = R_0$ up to $q = Q_c$, and not $m \cdot Q_c$. This means that $m < 1$ parameters behave like $m = 1$ materials.

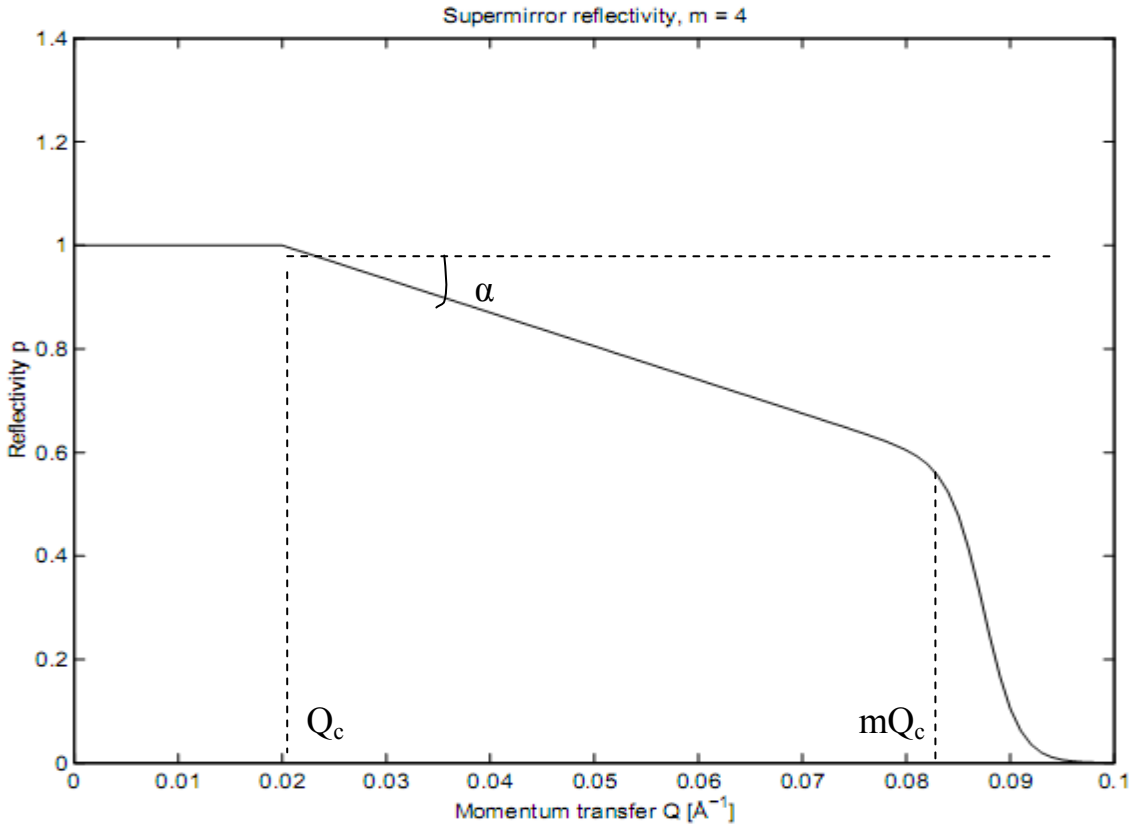

Fig.3.1 A typical reflectivity curve for a supermirror. The used values are: m = 4, R_0 = 1, Q_c = 0.02Å^{-1}, α = 6.49 Å, W = 1/300 Å^{-1}

The component Guide models a guide tube consisting of four flat mirrors. The guide is centered on the z axis with rectangular entrance and exit openings parallel to the x-y plane. The entrance has the dimensions (w1, h1) and placed at z = 0. The exit is of dimensions (w2, h2) and is placed at z = l where l is the guide length. See fig. 3.2. The reflecting properties are given by the values of R_0, m, Q_c, W and α, as defined above or alternatively from the reflectivity file.

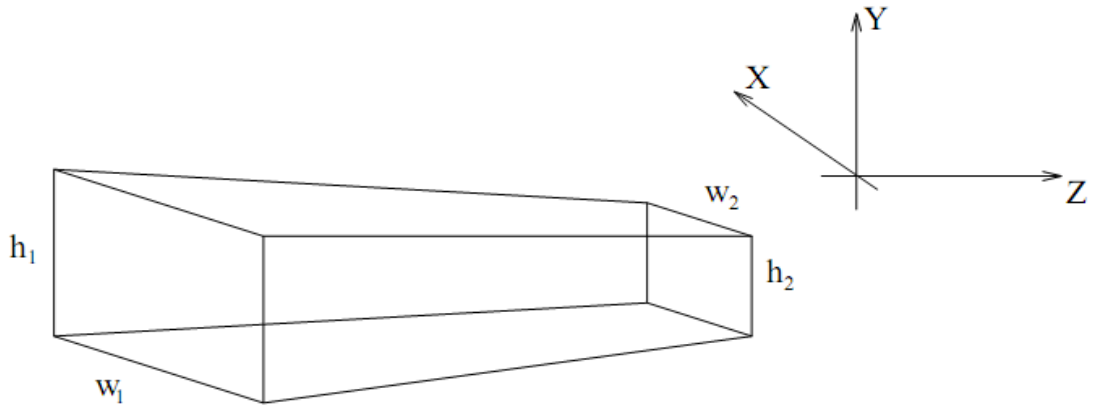

Fig. 3.2 The geometry used for guide systems

For computations on the guide geometry, the planes of the four guide sides are defined by giving their normal vectors (pointing into the guide) and a point lying in the plane:

$$\begin{array}{lcllcl} \mathbf{n}_1^v & = & (l, 0, (w_2 - w_1)/2) & \mathbf{O}_1^v & = & (-w_1/2, 0, 0) \\ \mathbf{n}_2^v & = & (-l, 0, (w_2 - w_1)/2) & \mathbf{O}_2^v & = & (w_1/2, 0, 0) \\ \mathbf{n}_1^h & = & (0, l, (h_2 - h_1)/2) & \mathbf{O}_1^h & = & (0, -h_1/2, 0) \\ \mathbf{n}_2^h & = & (0, -l, (h_2 - h_1)/2) & \mathbf{O}_2^h & = & (0, h_1/2, 0) \end{array} \quad 3.3$$

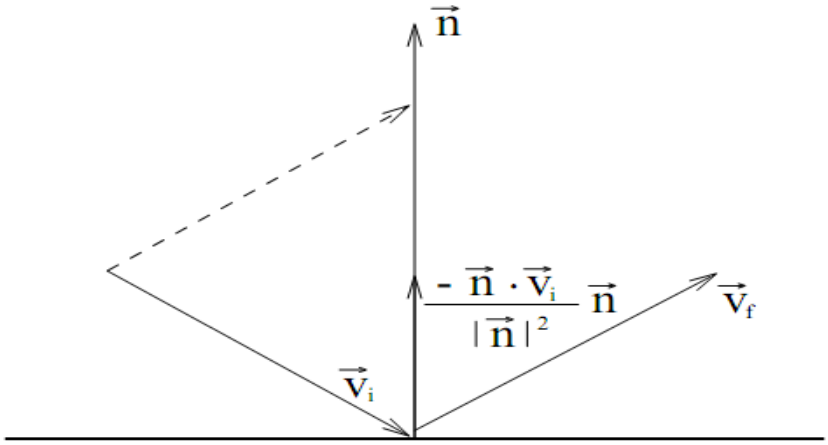

Fig.3.3.Neutron reflecting from mirror. v_i and v_f are the initial and final velocities, respectively and n is a vector normal to the mirror surface [Mont02]

In the following, we refer to an arbitrary guide side by its origin O and normal n.

With these definitions, the time of intersection of the neutron with a guide side can be computed by considering the projection onto the normal:

$$t_\beta^\alpha = \frac{(O_\beta^\alpha - r_0) \cdot n_\beta^\alpha}{v n_\beta^\alpha} \quad 3.4$$

where α and β are indices for the different guide walls, assuming the values (h,v) and (1,2), respectively. For a neutron that leaves the guide directly through the guide exit we have:

$$t_{exit} = \frac{l - z_0}{v_z} \quad 3.5$$

The reflected velocity v_f of the neutron with incoming velocity v_i is computed by the formula:

$$v_f = v_i - 2n \cdot \frac{v_i}{|n|^2} n \quad 3.6$$

The algorithm for the propagation of the neutron inside the guide is:

1. The neutron is initially propagated to the z = 0 plane of the guide entrance.
2. If it misses the entrance, it is ABSORBED.
3. Otherwise, repeatedly compute the time of intersection with the four mirror sides and the guide exit.

4. The smallest positive t thus found gives the time of the next intersection with the guide (or in the case of the guide exit, the time when the neutron leaves the guide).

5. Propagated the neutron ray to this point.

6. Compute the reflection from the side.

7. Update the neutron weight factor by the amount $\pi_i = R(Q)$.

8. Repeat this process until the neutron leaves the guide.

In addition to the linear guide a tapered guide can be implemented which has many divisions that can approach an elliptic or parabolic shape. The input parameters for such a guide are:

- w1(m) width at the guide entry
- h1(m) height at the guide entry
- linw (m) distance of 1. focal point and real guide entry - left and right horizontal mirrors
- loutw(m) distance of real guide exit and 2nd focal point-left and right horizontal mirrors
- l (m) length of guide
- linh(m) distance of 1st focal point and real guide entry -top and bottom vertical mirrors
- louth(m) distance of real guide exit and 2nd focal point -top and bottom vertical mirrors
- option (string) define the input function for the curve of the guide walls

  The options are:
  - "elliptical" - define elliptical function of guide walls
  - "parabolical" - define parabolical function of guide walls
  - "file = [filename]" - read in ASC-file with arbitrary definition for the curve of the guide walls
- d (m) thickness of subdividing walls
- k (1) number of channels in the guide (>= 1)
- R_0 (1) low-angle reflectivity
- Qcx ($Å^{-1}$) critical scattering vector for left and right vertical mirrors in each channel
- Qcy ($Å^{-1}$) critical scattering vector for top and bottom mirrors
- alphax (Å) slope of reflectivity for left and right vertical mirrors in each channel
- alphay (Å) slope of reflectivity for top and bottom mirrors
- mx (1) m-value of material for left and right vertical mirrors in each channel. Zero means completely absorbing.
- my:(1) m-value of material for top and bottom mirrors. Zero means completely absorbing.
- W ($Å^{-1}$) width of supermirror cut-off for all mirrors
- segno (1) number of segments (z-axis) for cutting the tube

A correlation between this parameters and those that define an ellipse a, b and f is presented in chapter 5.2.3.

4. Simulation results

In this chapter are presented a series of simulation using McStas for reaching the sub-mm range, for the optimization of the instrument PGAA at FRM II and for a first prototype based on the principles of adaptive optics, together with the interpretation of the results obtained.

4.1. Reaching the sub-mm range

The aim of the first Monte Carlo simulations using McStas was to produce focal spots with a diameter of the order of 0.1 mm. We will discuss the results of our simulations, i.e. the gains obtained, their variation with lambda as well as the evolution of the beam size.

4.1.1. The set up

Within the simulation program McStas, a component Tapering\guide.comp was developed that requires as input parameters the focal lengths of the entrance, f_{in} and the exit, f_{out}, of the guide, the value of the wave number that defines the critical edge of total reflection of the coating in units of m, the size of the aperture (width x height) and the length of the guide, L. The size of the exit is defined by these parameters. For obvious reasons, the smaller the focal length at the exit, the smaller the focal spot.
We have started our simulations with the cold source of FRM2, which is 22 cm x 14 cm large. In order to obtain focal points in the region of 1mm with symmetric elliptical guides it was necessary to start with a guide entrance area of 1cmx1cm. Due to the large loss in accepted intensity from the source, we have also used a source with reduced dimensions: 1cmx1cm. For this 2 sources we have used linear guides and elliptical guides with the initial length L 30m and same entrance areas at the beginning (height h 1cm and width w 1cm) placed at the distance d 0,2 m away from the source (see fig.4.1).

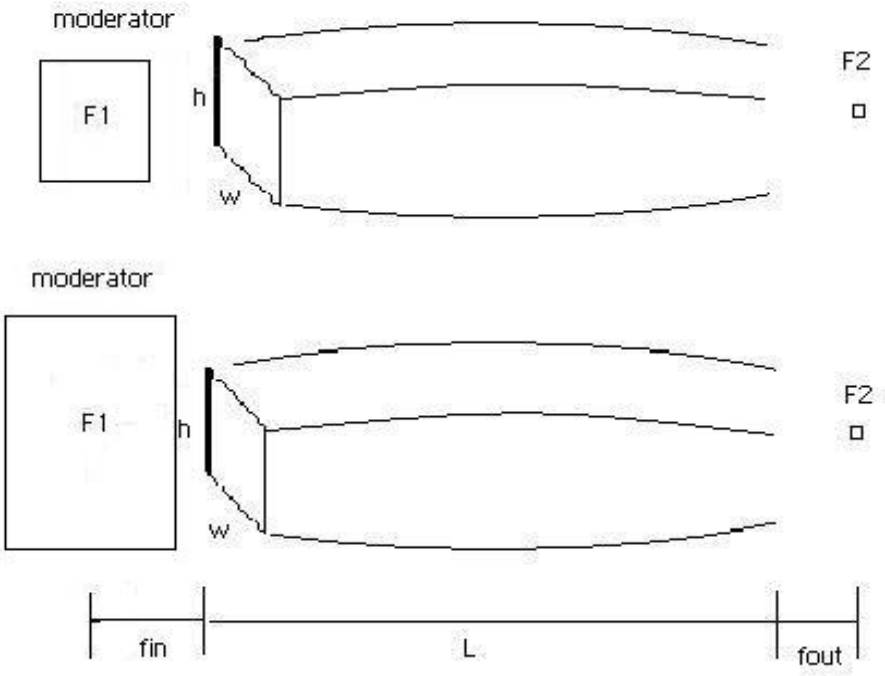

Fig.4.1 Schematic of the set up. Top: small moderator (10 mm × 10 mm). Bottom: cold moderator at FRM II (220 mm × 140 mm)

4.1.2.Simulation results

The gain distributions over lambda obtained for these two set ups are presented in fig.4.2 (Intensity distribution over lambda for the elliptical guide divided by the intensity distribution for the linear guide).

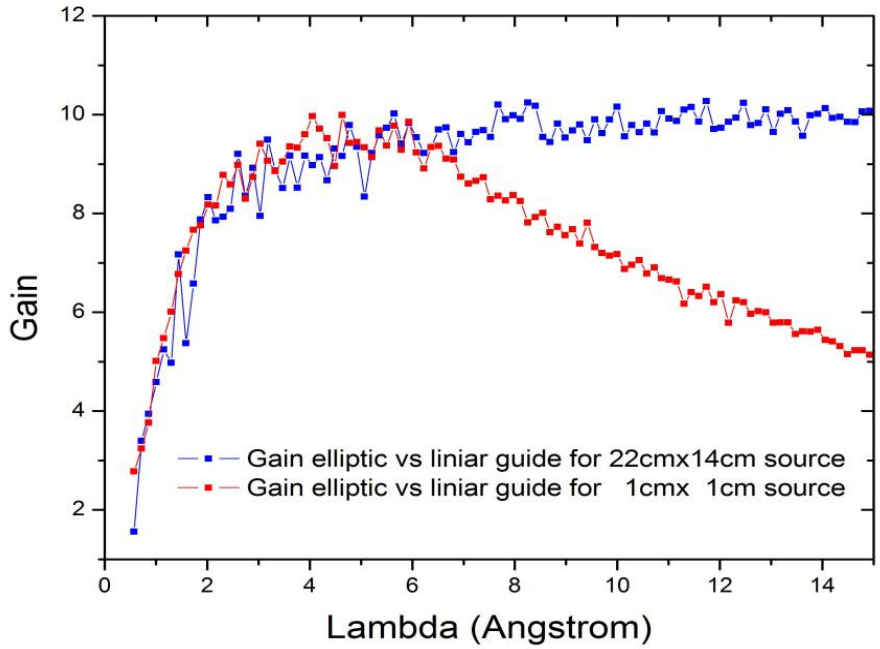

Fig.4.2 Gain in intensity for symmetrical elliptical, 30 m long, placed at 0,2 m after the source for a source 22 cm x 14 cm large blue color and 1cmx1cm large red color

If we compare the gain distributions in the two cases, a gain factor of around 10 is obtained in both cases small and big source, while in the case of the smaller source we only win in the case of small wavelengths due to multiple reflection that can occur for larger wavelengths.

In order to confirm this, we have chosen two bandwidths for the wavelength: first one from 1 to 5 Å and the second one from 8 to 15 Å and we have varied the distance d between the source and the entrance of the elliptic guide by keeping the ellipse symmetrical.

In Fig.4.3 is presented a comparison of the Position Sensitive Detector (PSD) in focal point of the elliptic guide on the left side for lambda from 1 to 5 Å and on the right side for lambda from 8 to 15 Å (from top 100 mm, middle 10 mm and bottom 5 mm distance between source and entrance of the elliptic guide) As one can see, we have a better focusing in the case of lower lambda regime, then in the case of larger lambdas, due to multiple reflections

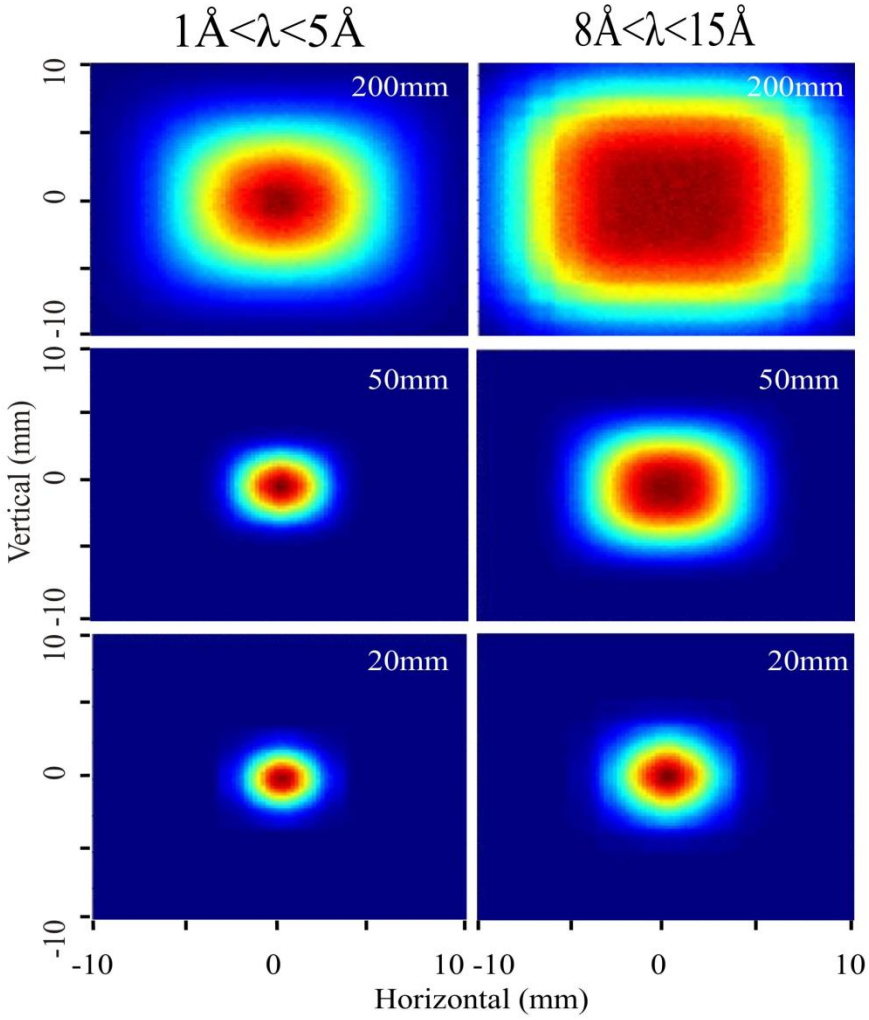

Fig.4.3 Comparison of PSD detectors in focal point left side for lambda from 1 to 5 Å and right side for lambda from 8 to 15 Å (from top 200 mm, middle 50 mm and bottom 5 mm distance between source and entrance of the elliptic guide)

In order to analyze the spot size in focal point we have varied the distance from the elliptical guide to the source, keeping the elliptical guide symmetrical (i.e. $f_{in} = f_{out}$).
The calculated values for the entrance dimensions of the elliptical guide (second column) for different distances between the focal point and the entrance of the ellipse (first column) are listed in table 4.1.

fin/fout(mm)	exit/entrance(mm)
200	10
100	7.08
50	5.01
20	3.17
10	2.24
5	1.59

Table 4.1 Entrance dimensions of the elliptical guide for different focal distances

The obtained intensities (PSD detector in focal point) are presented in fig.4.4 and one can observe that by going closer and closer to the source and correspondingly to smaller cross-sections for the guide entrance and exit we have a better focused beam.

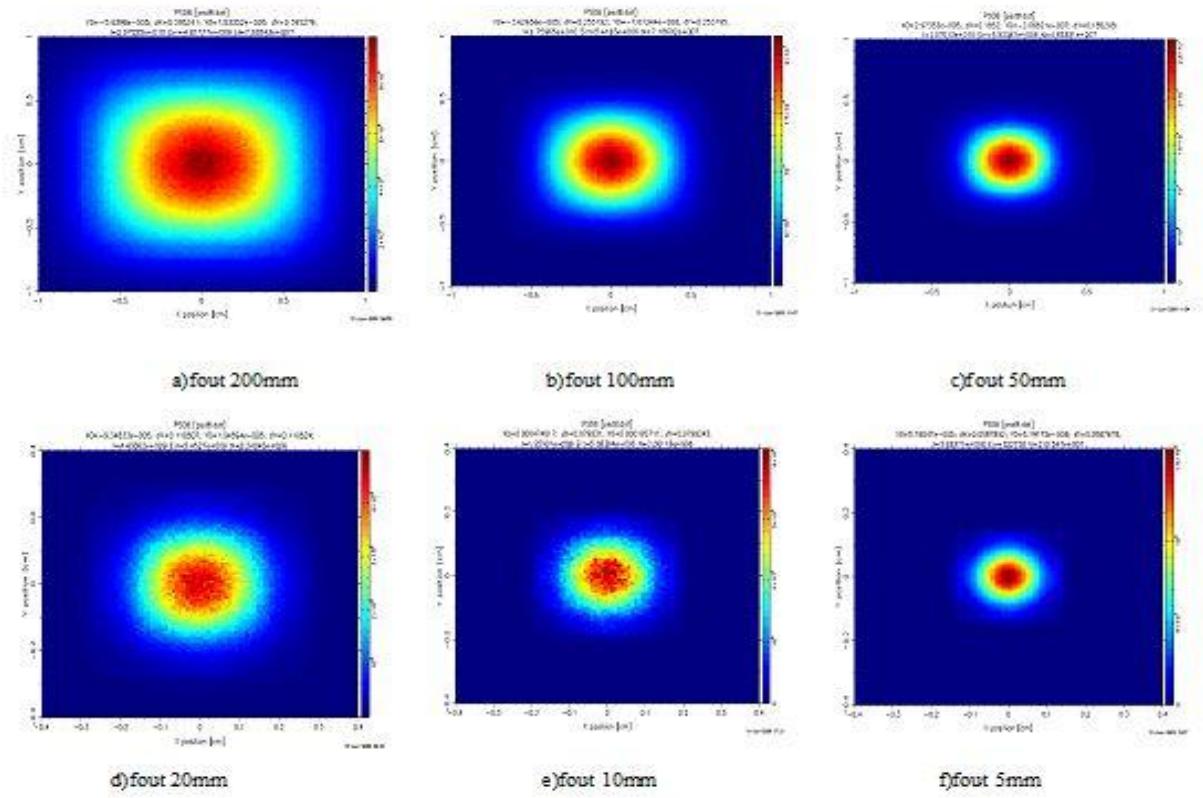

Fig.4.4 PSD detector in at the entrance and in focal point for different distances between source and entrance of the elliptical guide

In fig. 4.5.a are plotted the integrated intensity (we have chosen a 0,2 mm x 0,2 mm large area at the centre of the PSD detector and we have averaged the intensity over this central area) and the total flux for different distances from the source to the entrance of the elliptic guide. The decrease in peak width is explained by the corresponding decrease in the dimensions of the elliptic guide (see also table 4.1). A decrease in intensity is also observed as we get closer to the source, due to the intensity distribution over lambda (we may win in intensity only for a specific wavelength or for an interval).

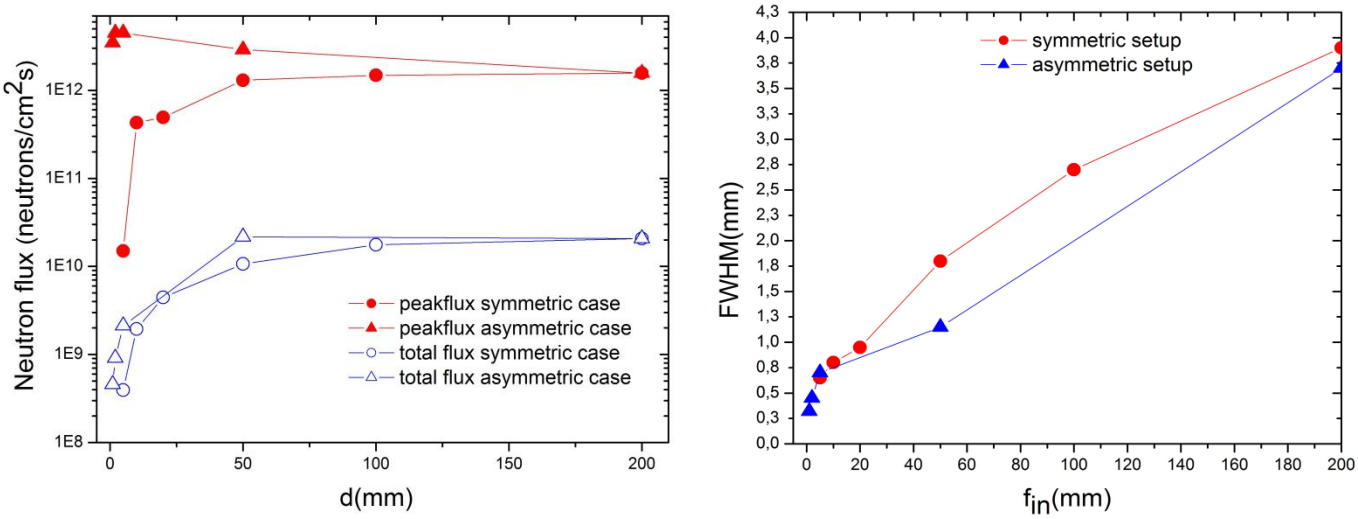

Fig.4.5. a.Integrated intensity for different distances from the source to the entrance of the elliptic guide

b. Peak width for different distances from the source to the entrance of the elliptic guide

The horizontal cuts through the PSD in focal point in order to determine the full width at half maximum are plotted in fig.4.5.b and we are already in the sub mm range with a total flux of $3.93 \cdot 10^8$ neutrons/cm^{2}s for d = 5 mm.

4.1.3.Non symmetric set up

All the results obtained up to this point were for symmetrical ellipses (i.e.$f_{in} = f_{out}$). Due to the fact that going 5mm away from the moderator for the maximum focusing meant an entrance of the ellipse with a cross section with 1,6mm x 1,6mm and correspondingly a decrease in the total flux as seen in fig.4.5.

The non symmetric set-up was to keep the distance between the primary focal point of the ellipse and the entrance of the guide (f_{in}) constant at 200 mm with a corresponding cross

section of 10 mm x 10 mm and to vary the distance between the exit of the elliptic guide and the secondary focal point (f_{out}). The results obtained for the total flux and for the peak flux (see table 4.2) show that an unsymmetrical ellipse with a f_{in} of 200 mm and and f_{out} of 5 mm is the best choice for obtaining a minimum beam size in focal point.

f_{in} (mm)	f_{out}(mm)	total flux (neutrons/cm^{2}s)	peak flux (neutrons/cm^{2}s)	Peak FWHM (mm)
200	200	$2.07 \cdot 10^{10}$	$1.57 \cdot 10^{12}$	3,70
200	50	$2.17 \cdot 10^{10}$	$2.90 \cdot 10^{12}$	1,15
50	50	$1.07 \cdot 10^{10}$	$1.30 \cdot 10^{12}$	1,10
200	5	$2.12 \cdot 10^{9}$	$4.50 \cdot 10^{12}$	0,70
5	5	$3.93 \cdot 10^{8}$	$1.50 \cdot 10^{11}$	0,65

Table 4.2 Intensities and FWHM for different f_{in} and f_{out}

Taking these values, the next step was to insert a pinhole to further reduce the dimensions of the focused beam. Without pinhole we have obtained a beam with a full width at half maximum of around 0,7 mm. First we have placed the slit of 0,5 mm radius at different distances between the exit of the ellipse and the secondary focal point. The FWHM and the intensity distribution varying with this distance are plotted in fig.4.6.

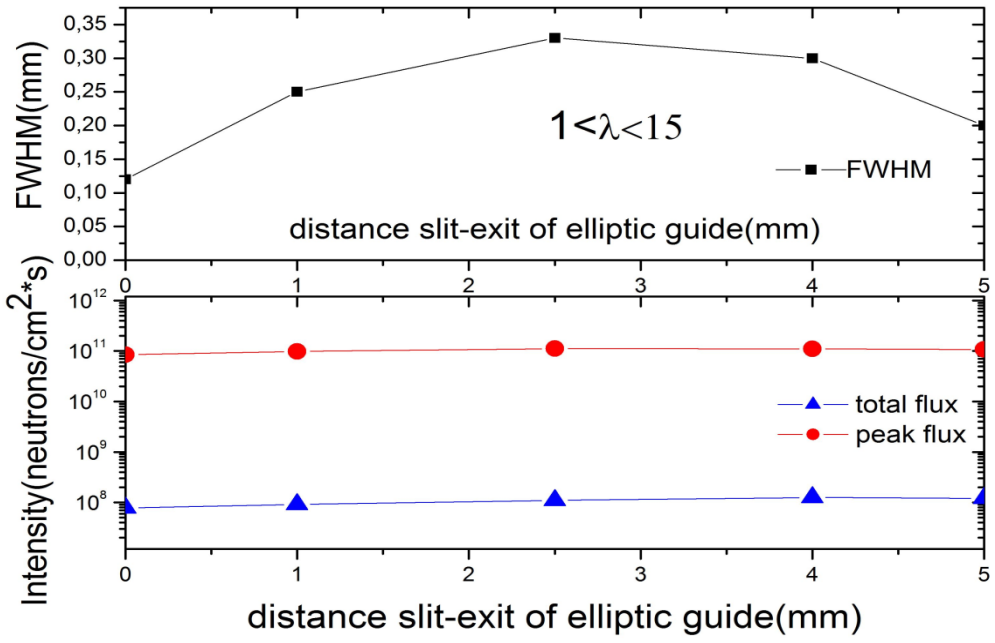

Fig.4.6. FWHM and Intensity distribution varying with the distance from the aperture to the exit of the elliptical guide

With the slit fixed at 1mm away from the guide exit, we varied the radius of the slit, with values lower than 0.5 mm. The beam profiles in focal point are presented in fig.4.7. The simulations were made for a lambda band from 3 to 5 Å.

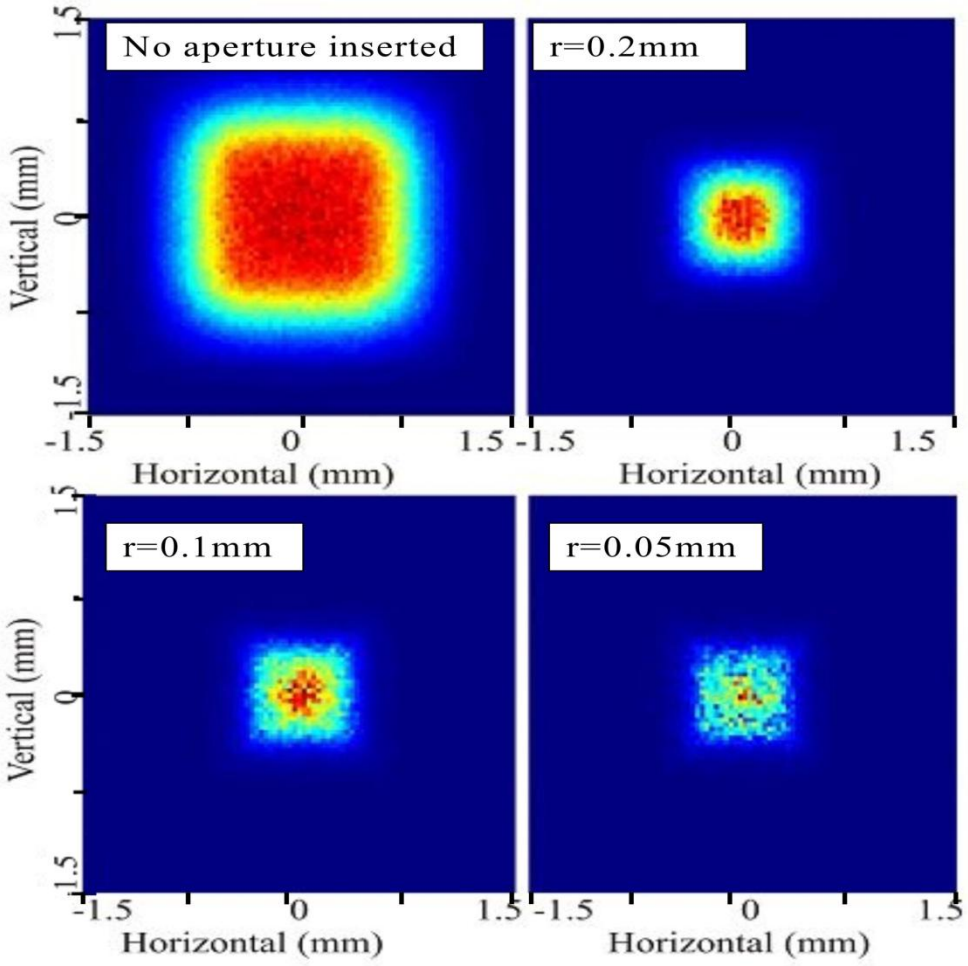

Fig. 4.7 PSD monitor in focal point for different radius of the slit

For the lowest FWHM of 0,15 mm, in the case of a radius of 0,2 mm of the slit, placed 1mm away from the guide exit, we have an intensity of 4.8×10^{7}n $cm^{-2}s^{-1}$

These simulations can find applications in elastic and inelastic neutron scattering as well as for neutron radiography and tomography. In elastic and inelastic neutron scattering for probing very small samples, since the new samples are usually small, in particular single crystals. Another application could be in the field of extreme environment experiments, like samples under very high pressure or high magnetic fields, when the neutron beam could be focused on the sample and again the reflected neutron beam collected so that the background noise and the scattering on the sample cell needs to be considerably reduced.

By this additional shaping with a pinhole the emerging beam can be used as bright neutron source for a cone beam geometry, allowing to increase the resolution and at the same time magnify the object for neutron imaging.

4.2 PGAA

In the following, the simulations were made for the prompt gamma activation analysis spectrometer, with the aim of obtaining better focusing. The focusing guide existing at the PGAA instrument is composed of 2 elliptical focusing neutron guides (with supermirrors coating with m = 3) first one with a length of 5.8 m and a second one with a length of 1.09 m separated by a thin aluminium window. With this configuration the performances of the instrument are:

Position	Neutron flux (n/cm^2s)	Beam profile (HxW) (mm^2)	
End of the guide:	$6.0 \cdot 10^9$	28 x 62	measured
Measurement position 1 (30-35 cm from the end of the guide):	$7.3 \cdot 10^9$	14 x 38	expected
Measurement position 2 (9-10 cm from the end of the guide):	$2.0 \cdot 10^{10}$	4 x 11	expected

Table 4.3. Performances of the existing elliptical guide at PGAA instrument

We have tried to obtain a better focussed beam by prolongation of the existing elliptic guide with a new part. First we have chosen a length of the additional guide of 7,5 cm and coatings for the neutron guide of supermirrors with m = 5 and 6 and calculated the flux using Monte Carlo simulation in the program McStas. We consider a wavelength band $1\ Å < \lambda < 21\ Å$ and a neutron flux of $10^7 n/cm^2 s$. The neutron distribution in focal point is presented in the next figures:

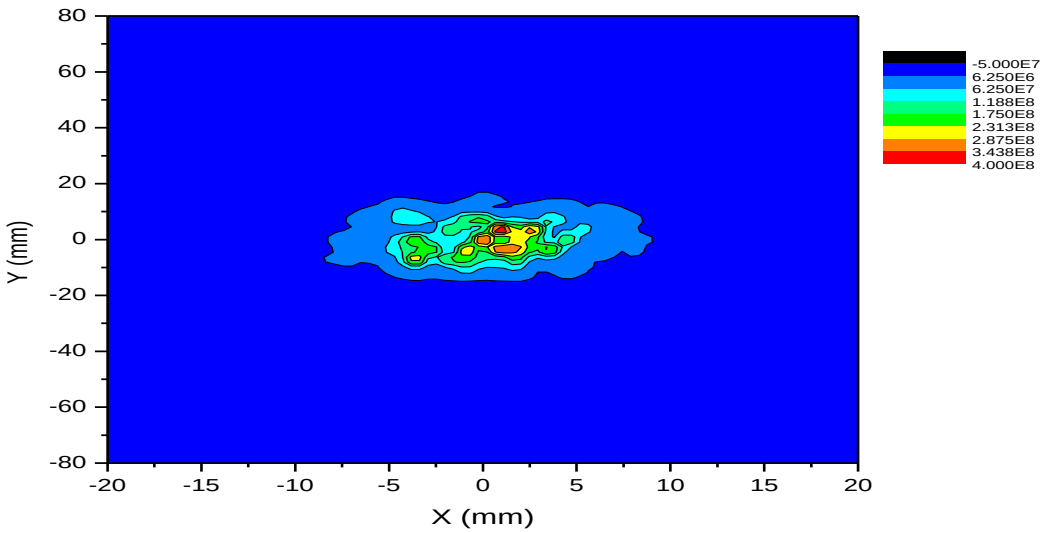

Fig.4.8 Neutron flux in focal point without the prolongation guide

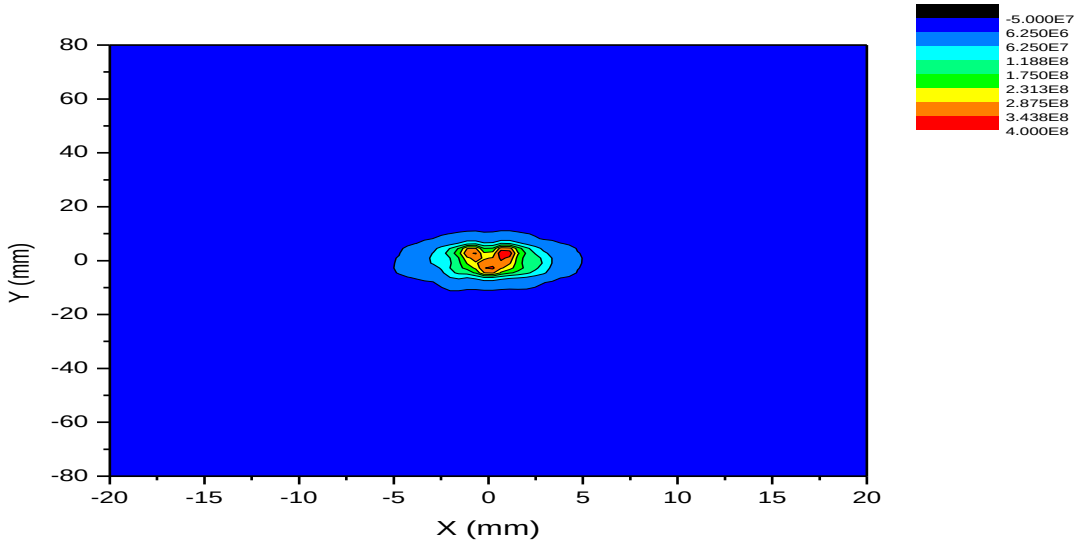

Fig.4.9 Neutron flux in focal point for m = 5 coating of the prolongation guide

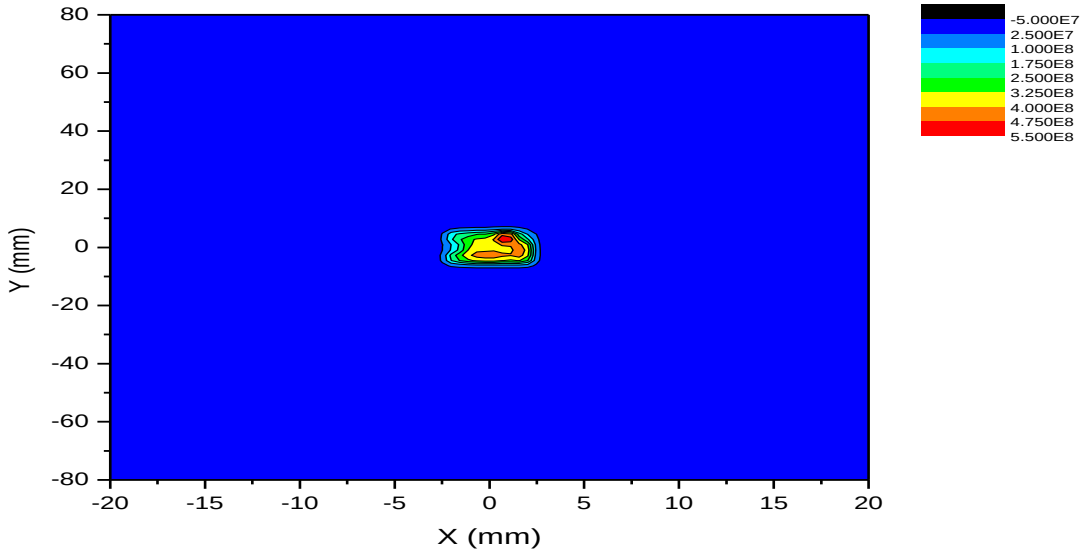

Fig.4.10. Neutron flux in focal point for m = 6 coating of the prolongation guide

One can observe from the figures above that we have a significant reduction of the spot size by adding a prolonging elliptical guide to the existing one. We have also calculated the gain by dividing the intensity averaged over a central area of 4 mm x 1mm of the position sensitive detector in the focal point after adding the guide by the initial intensity in focal point (that of the position sensitive detector without the 7.5 added elliptical guide). The results are presented in table 4.4 and as one can observe a gain of at least a factor of 2 is obtained in both cases:

	m = 5	m = 6	initial
Intensity in focal point (n/cm^2s)	$3.47 \cdot 10^8$	$3.89 \cdot 10^8$	$1.39 \cdot 10^8$
gain	2.49	2.79	1

Table 4.4 Gain calculated for a 7.5 cm long additional elliptic guide

The next step was to vary the length of the additional guide and to calculate the gain for each length in order to find the optimum length for the additional guide with a coating of m = 5. The calculations are presented in table 4.5.

	initial	1 cm	2 cm	3 cm	4 cm	5 cm	6 cm	7 cm	7.5 cm	8 cm	9 cm
Intensity in focal point (n/cm^2s)	$1.39 \cdot 10^8$	$1.19 \cdot 10^8$	$9.85 \cdot 10^7$	$1.14 \cdot 10^8$	$2.58 \cdot 10^8$	$3.37 \cdot 10^8$	$2.54 \cdot 10^8$	$3.24 \cdot 10^8$	$3.47 \cdot 10^8$	$4.51 \cdot 10^8$	$3.50 \cdot 10^8$
gain	1	0.86	0.7	0.82	1.85	2.42	1.82	2.33	2.29	3.25	2.51

Table 4.5 Gain calculated for various lengths of the additional elliptic part

As one can see a length of the additional guide of 8 cm brought the highest increase in intensity in the focal point, so we have chosen this length and varied the m value for the supermirror coating (m= 3, 4 and 5 respectively).The results of the calculated intensities and gains are presented in Table 4.6.

	initial	m = 3	m = 4	m = 5
Intensity in focal point (n/cm^2s)	$1.39 \cdot 10^8$	$2.94 \cdot 10^8$	$4.24 \cdot 10^8$	$4.51 \cdot 10^8$
gain	1	2.11	3.05	3.25

Table 4.6 Gain calculated for a 8 cm length of the additional elliptic part and various m-values for the supermirror coating

As we observed a small difference between a coating of m = 4 and m = 5 we decided to continue the simulation with a m = 4 coating for the prolongation of the elliptical guide and to introduce at half distance between the end of the guide and the focal point a small aperture in order to reduce substantially the dimension of the final spot. In table 4.7 are listed the beam profiles before and after the addition of the 8 cm elliptical guide coated with m = 4.

Position	Beam profile (HxW) (mm^2)
Beginning	50 x 110
End of the initial elliptical guide	28 x 62
End of the modified elliptical guide	4 x 9

Table 4.7 Beam profile before and after the continuation of the elliptical guide.

As one can see from Table 4.7 with the additional part we have reduced the beam profile to a dimension of 4 x 9 mm^2

For this configuration we have introduced the aperture 1cm far from the end of the prolonged elliptical guide and 1 cm in front of the focal position and varied the radius of this aperture.

Radius of the aperture(mm)	Intensity in focal point (n/cm^2s)	Beam diameter in focal point(mm)
0.1	$8.10 \cdot 10^6$	0.036
0.2	$1.94 \cdot 10^7$	0.12
0.3	$1.64 \cdot 10^7$	0.16
0.4	$1.50 \cdot 10^7$	0.18
0.5	$1.60 \cdot 10^7$	0.2

Table 4.8 Beam profile in focal point after the introduction of aperture

For an aperture of 0.1 mm radius the beam is focused with focus spot of around 40 micrometers in diameter. The simulated neutron flux for this case is presented in figure 4.11.

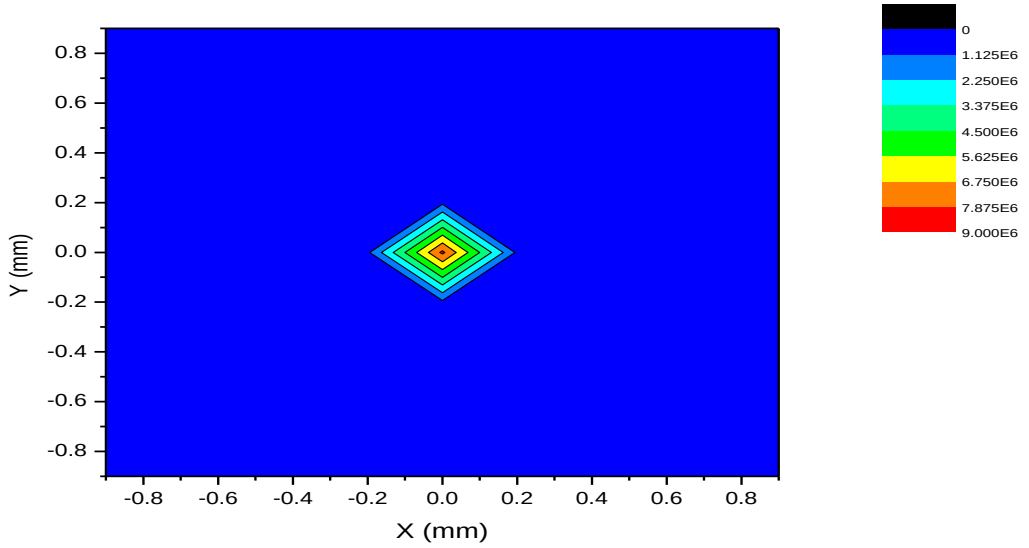

Fig.4.11 Neutron flux in focal point for m = 4 coating of the prolongation guide (with 8 cm length) and an aperture of 0.1 mm placed 10 mm in front of focal point

We have therefore obtained by McStas simulation a well focused neutron beam with a diameter around 30 micrometer and an intensity of $8.10 \cdot 10^8$ n/cm^{2}s, results that open wide possibilities in the field of neutron imaging and radiography as well as in probing very small samples.

4.3. Adaptive optics

The aim of the implementation of adaptive focusing neutron optics is to adapt the beam size as well as the beam divergence to the sample. The Monte Carlo simulations were made for testing the performances of an adaptive element, following the principles described in chapter 2.3. The evolution of the focal point as well as the properties of the beam is investigated using Monte-Carlo simulation. The results of these simulations are the base for first experiments with an adaptive prototype as presented in chapter 5.

As stated in chapter 2.3, a decrease of the curvature leads to an increased focal length with an increased width of the beam in focal point and a decreased divergence (as an example in fig. 4.12. are presented the beam profile in focal point and the divergence for two different f_{out} values).

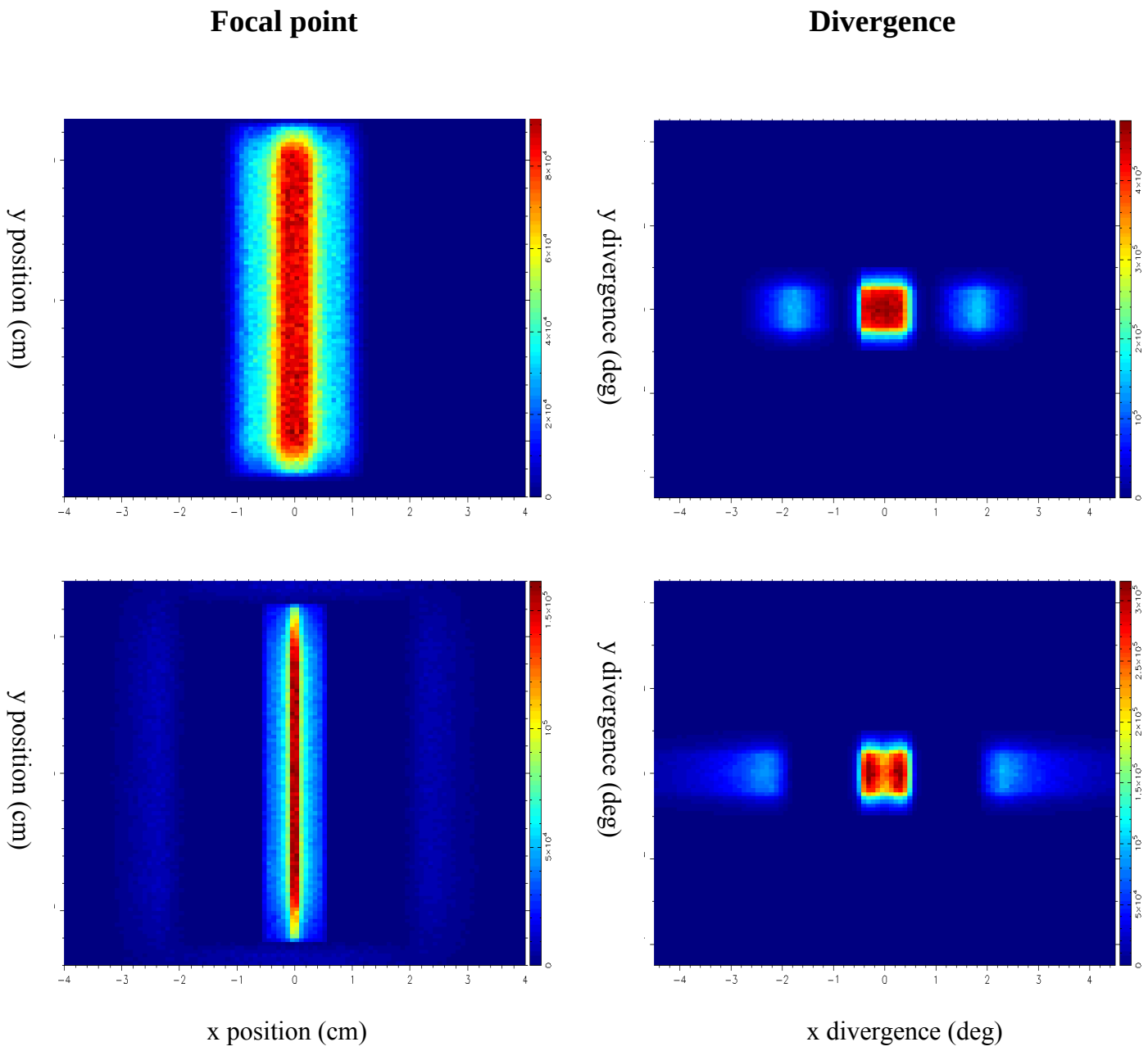

Fig. 4.12. Beam profile and divergence for f_{out} 250 mm (top line) and 50 mm (bottom line)

4.3.1. Monte Carlo simulations

First we discuss the results of Monte Carlo simulations followed by presenting possible applications for an adaptive parabolic focusing device.

In order to have the possibility to vary the curvature of the guide independently in x and y direction using simulations, it was necessary to develop a new McStas component that allows changing the properties of the four sides independently. The sides can have different types of

curvatures for each side (linear, elliptic or parabolic). The walls of this new component are truly curved and do not consist of multiple segments that approximate the desired shape as in previous implementations. Moreover, the inner and outer sides of each wall can be set as transparent, absorbing or reflecting [Mont03].

To implement such a focussing guide in the McStas program (3) one has to define for each side the following parameters: l = length of the guide (same for all sides), w_{in}= width of the entrance of the guide, f_{in} and f_{out}. All these parameters define the width at the exit of the guide if a parabolic or elliptic shape is chosen.

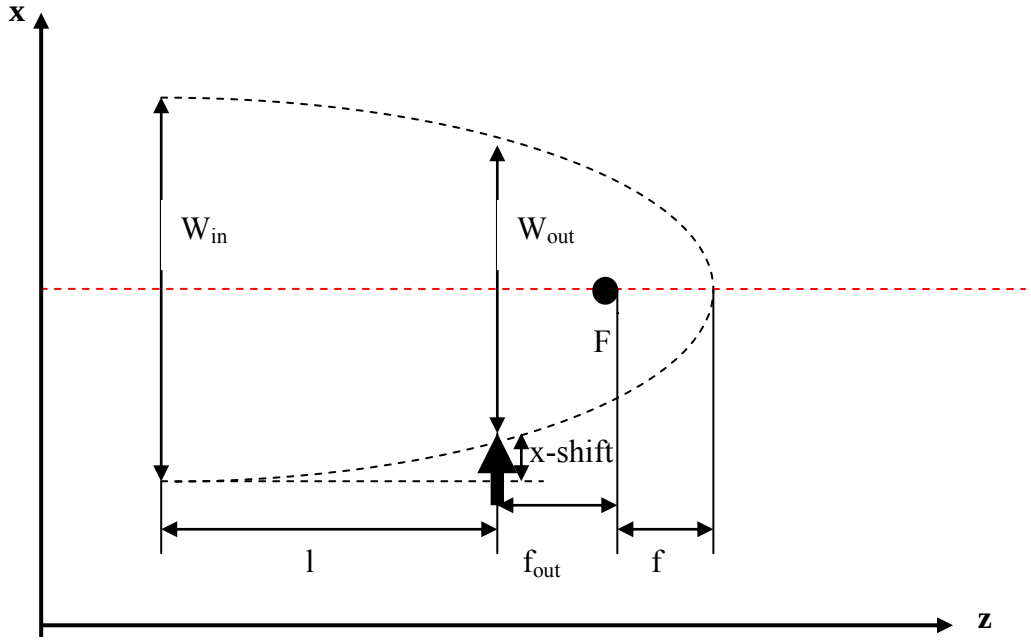

Fig.4.13 Parameters for defining a parabolic focusing guide using McStas. f_{in} designates the distance from the first focal point to the entrance of the guide (f_{in} = 0 for parabolic guide) and f_{out} the distance from the exit of the guide to the second focal point, respectively.

If the parabola is given by: $z = b - ax^2$,the parameters a and b can be calculated by:

$$a = \frac{1}{2(\sqrt{(l+f_{out})^2+w_{in}^2}-((l+f_{out}))} \quad 4.1$$

$$b = l + f_{out} + \frac{1}{4a} \quad 4.2$$

The tangent at any point is given by:

$$z = m \cdot x + n \quad 4.3$$

The parameters of this tangent can be calculated by:

$$m = -2 \cdot a \cdot w_{in}$$
$$n = a \cdot {w_{in}}^2 + b \qquad 4.4$$

To calculate the rotation angle and the movement x for adaptive optics one can use:

$$\alpha = arctg(-2 \cdot a \cdot w_{in}) \qquad 4.5$$

$$x - shift = \frac{l-n}{m} = \frac{f_{out}+\frac{1}{4a}}{2 \cdot a \cdot w_{in}} - \sqrt{\frac{1}{a} \cdot (f_{out} + \frac{1}{4a})} \qquad 4.6$$

In table 4.9 are calculated as example the shift in x direction (the direction perpendicular to the optical axis in horizontal direction) which is defined as (w_{in} - w_{out})/2 (marked in fig.4.13) with the variation of f_{out} from 500 mm to 50 mm the x-shift goes from 5.1 mm up to 12.2 mm shift for the last case. This calculations were done in order to see the correlation between the variation of the focal distance and therefore of the curvature of the guide and actual bending of the glass.

f_{out} (mm)	x-shift(mm)
50	12.2
100	10.4
200	8.2
300	6.8
400	5.8
500	5.1

Table 4.9. Variation of the x-shift with the f_{out} value calculated using equation 4.6.

4.3.2.Simulation results

We have simulated a 1-dimensional focusing guide, where the top and bottom sides are straight and transparent for neutrons. First we only varied the coating of the guide, second we have varied the distance d from the exit of the last linear guide to the entrance of the adaptive guide and finally we have varied the f_{out} for the left and right side.

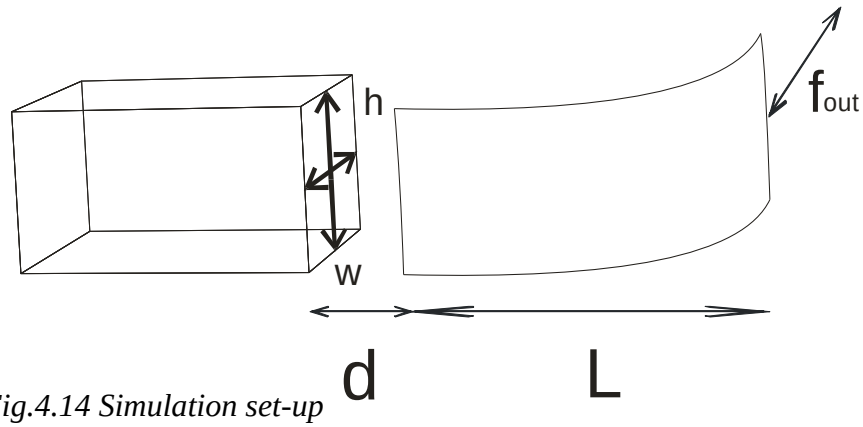

Fig.4.14 Simulation set-up

In the following we consider a 500 mm long guide with f_{out} = 250 mm that is placed 1 meter behind a straight guide with a cross section of 35 mm x 120 mm providing neutrons with a wavelength λ = 5 Å. By following the evolution of the beam, we observe 2 beams appearing at the exit of the guide (reflected from the coated guide walls) that converge towards a focal point with a width of 5 mm. Of course, further away the beam diverges again leading to two beams (see fig. 4.15)

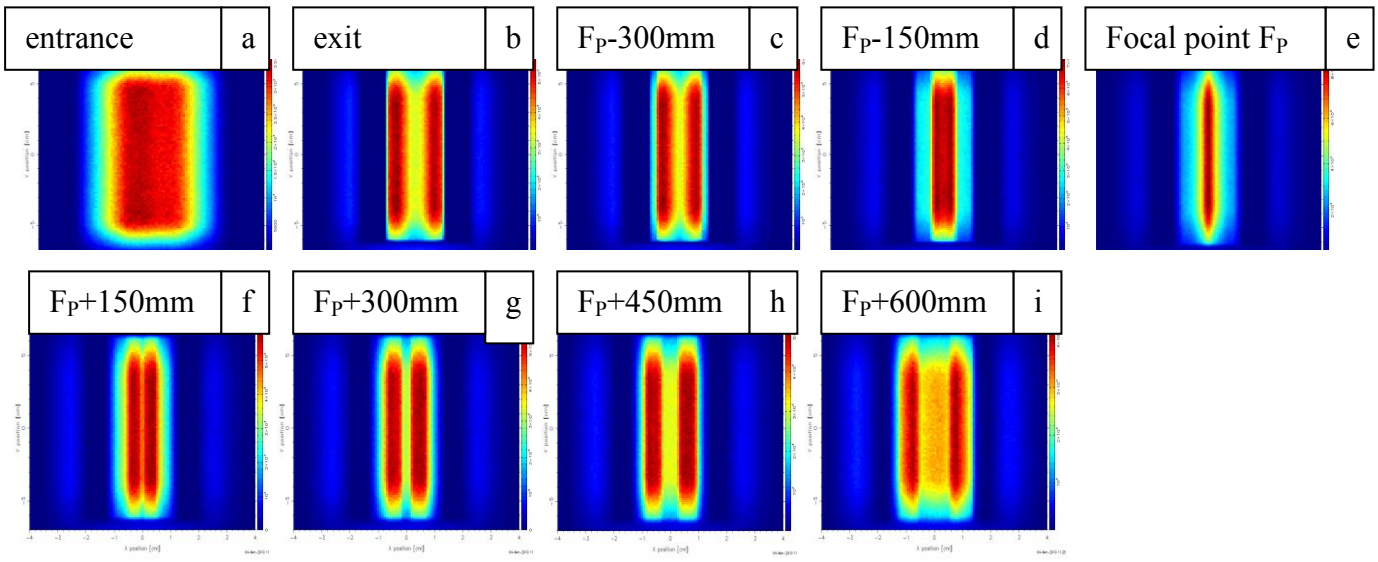

Fig.4.15 Evolution of the beam from the entrance of the parabolic focussing guide (figure a) to the exit (figure b) to the focal point F_P (figure e) up to 500 mm away from exit of the guide (figure i) in steps of 150 mm

Varying the coating of the guide with m starting from 2 up to 6 the intensity increases with the increase in m due to the increase in the accepted angle of incidence of the incoming neutrons. Therefore we have continued the simulations with an m value 6, and we varied the distance d from the exit of the linear guide to the entrance of the adaptive guide. For small d, the adaptive guide accepts neutrons with a large divergence, while for large d the divergence

is reduced (geometrical effect). Horizontal cuts through the PSD (position sensitive detector) were performed for each detector in the focal point and at the focal point position for the initial case (Fig.4.15). The intensity features can be easily followed if we look at one of the curves in Fig.4.16. Symmetrical starting from x = 7 cm down to 3.5 cm we are approaching the outer part of the guide from the outside. The 2 peaks from 4 cm to 2 cm are the reflected beam from the guide walls, the next drop in intensity is caused by the bent guide –shadowing" the incoming beam. The steep part represent the neutrons reflected by the coating, the plateau is the incident beam and finally the peak at x = 0 cm is our focused beam.

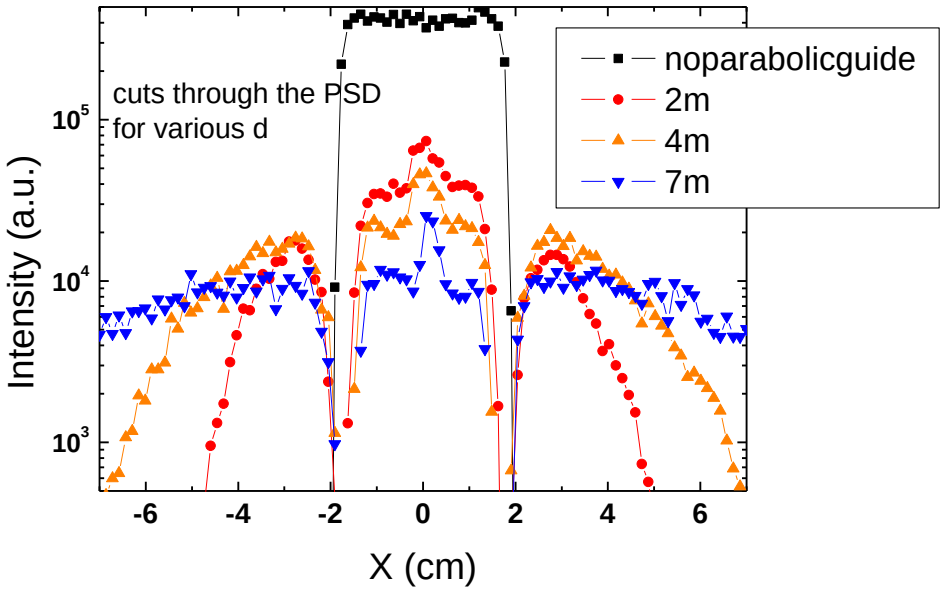

Fig.4.16 Horizontal cuts through the PSD in focal point for various d.

The intensity decreases with increasing distance of the elliptic guide from the feeding guide. Clearly the FWHM decreases as well because the divergence of the incident beam is reduced (Fig.4.17).

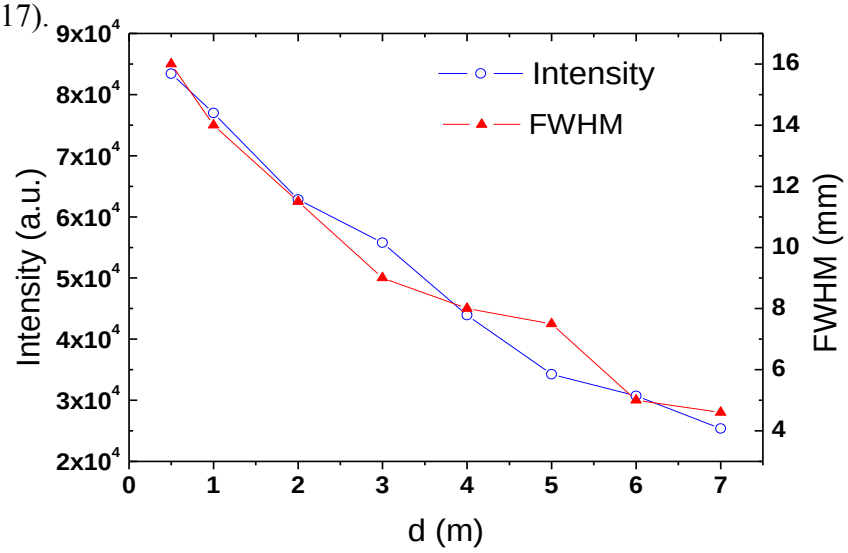

Fig.4.17 Intensity and FWHM for various d

For the following simulations we have chosen fixed d = 1m. In order to simulate the change in the curvature of the mirror we have varied the f_{out} value for the mirror, taking into account that McStas calculates automatically the shape and the exit dimensions of the guide from the entrance dimensions and the f_{out} value.

If we plot the horizontal cuts through the PSD in the focal point for each value of f_{out} and calculate the maximum intensity and the FWHM, we observe an increase in intensity for decreasing f_{out}, due to the increase in the accepted beam by increasing the curvature of the parabolic walls (see table 4.9, a bigger part of the beam is focused) and a sharpening of the beam, leading to a decrease of the FWHM, due to the decreased cross-section at the exit of the guide (fig.4.18).

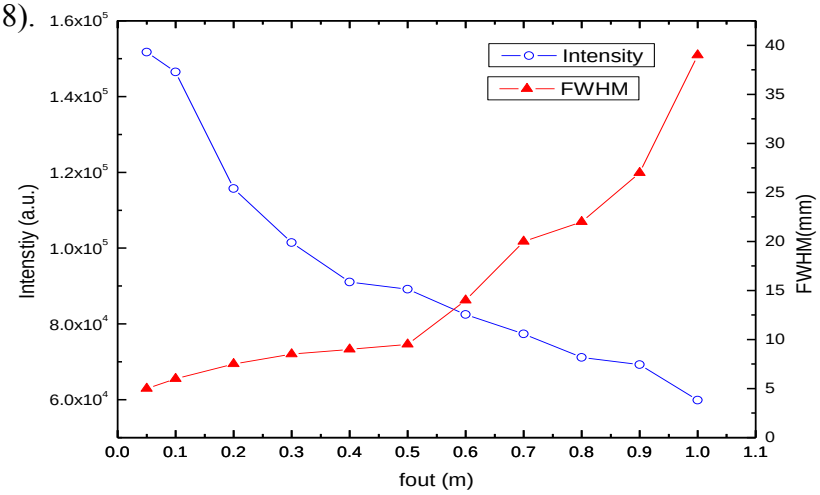

Fig.4.18. Intensity and FWHM for various values of f_{out}.

For example for a f_{out} = 0.1 m we obtain in the focal point a beam with a FWHM of 6mm and an intensity of $1.7 \cdot 10^5$ neutrons/cm^2·s.

It is very important to note that the shift of the thin side in x-direction and the angle alpha (defined as the angle made by the tangent at the parabola at the entrance and the optical axis) are correlated, when pressing against the mirror we also change the angle alpha(see fig.4.19).

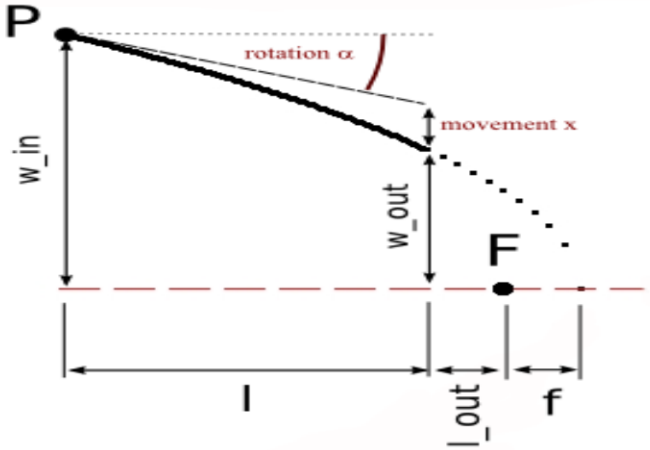

Fig.4.19. Scheme for the calculation of the relation between the rotation angle α and the movement in x direction.

If we press at the end of the parabola and the parabola shifts with x1, this corresponds to a shift in the angle of rotation alpha1. By pressing some more we change the shift in x2 but we also change the rotation angle so it is like we are sitting on a different parabola with a wider opening, but the same focal point.

4.3.3. Possible applications

One possible application of this prototype is the bending the beam out of the primary beam by tilting the component for a fixed alpha-x-setup. One can see as an example a simulation made for f_{out} = 0.3 m, length = 0.5 m, m = 6, d = 1m with only the right wall set as reflective and the other 3 walls as transparent. It is presented the divergence depending on the tilting angle in fig.4.20. By tilting the component the primary beam is more and more covered and the reflected beam appears, therefore the two beams can be separated by more than 3 degrees.

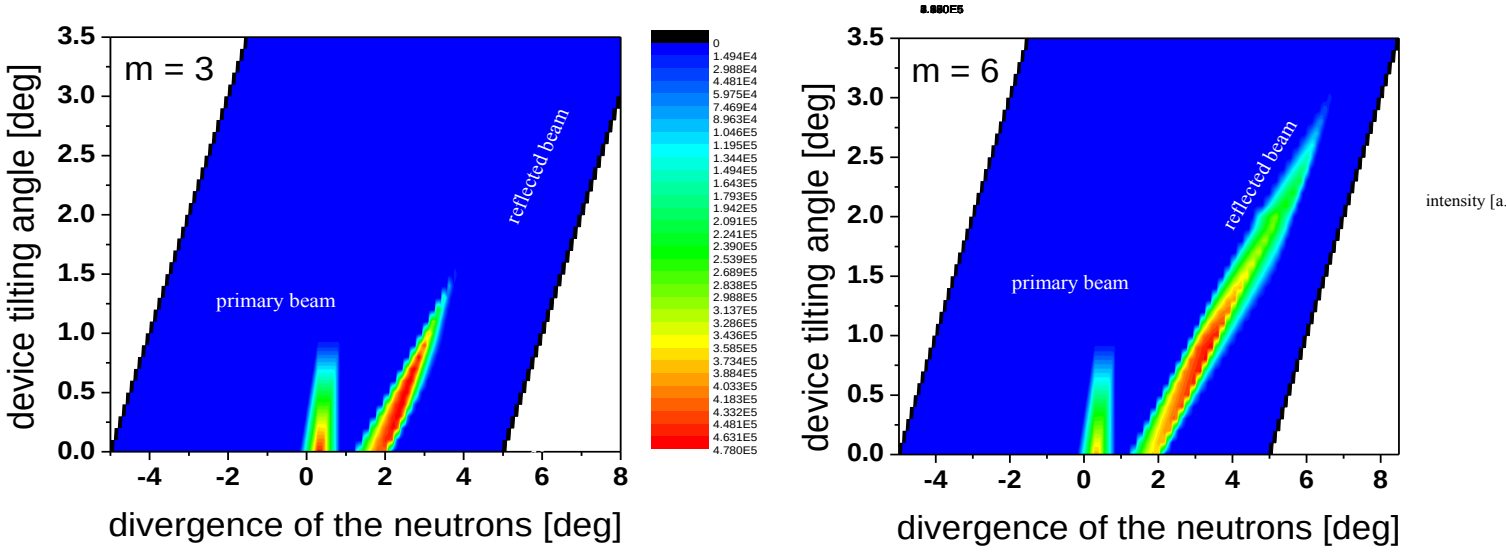

Fig.4.20. Simulation results for tilting the component for different m values. The curved guide does not cover completely the beam, this is why a primary beam can be observed.

New designs using one dimensional adaptive optics can be imagined for the triple axis spectrometer RITA and for the powder diffractometer DMC at PSI as well as for the reflectometer MIRA and the Time of Flight instrument TOFTOF at FRM II, for which the first simulation for improvement of the neutron optics were already performed and will be presented in chapter 5.

5. Simulations for TOFTOF

In this chapter are presented the Monte Carlos simulations made for optimizing the properties of the beam at the time of flight instrument TOFTOF at FRM II. The simulation results for different options are presented and discussed. After choosing the optimal shape, as resulting from the simulations, a prototype was constructed and mounted at the instrument. The characterization of the geometrical properties together with its performances during the neutron tests are also shown in this chapter.

5.1. The instrument

The simulations from chapter 4 can find applications to improve the beam of the TOFTOF instrument, a direct-geometry multi-disc chopper time-of-flight spectrometer, installed at the neutron source Heinz Maier-Leibnitz (FRM II). Moderated neutrons, arising from a liquid deuterium cold source (T = 25K), are transported to the sample by a primary S-shaped neutron guide (cross-section 44 x 100 mm^2, radius 2000 m) followed by a secondary, focusing, neutron guide (cross-section at its end: 23 x 46 mm^2). The use of the S-shaped neutron guide, which cuts off neutrons of wavelengths smaller than 1.4 Å, prevents the chopper system from the irradiation by too energetic neutrons, which would pass through the choppers and create an additional background [Unru01].

Neutron guide

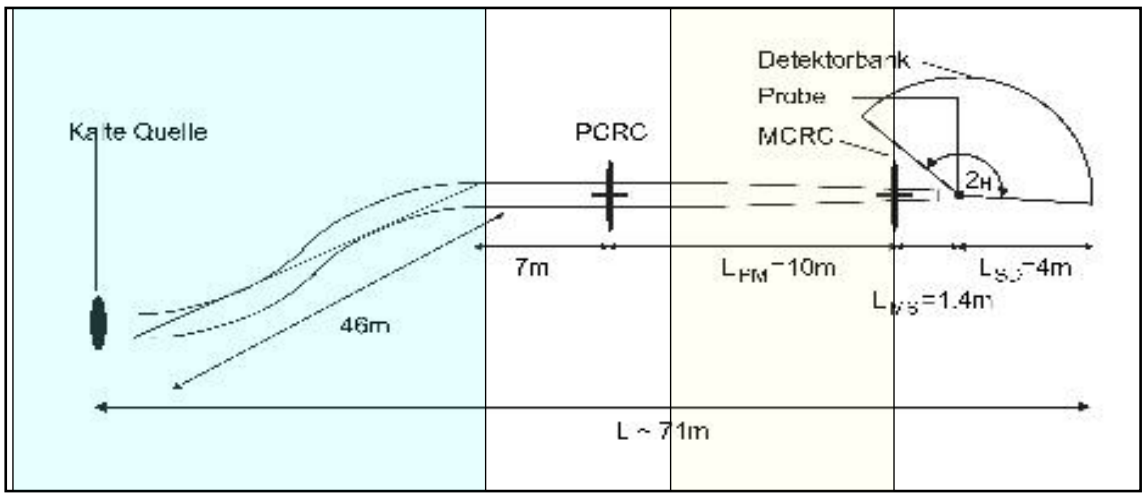

Primary S-shaped neutron guide

focusing neutron guide

Fig. 5.1. Neutron guide at TOFTOF

The main features of this instrument are:

- high signal-to-background ratio
- high intensity also at short incident wavelengths (10^8 neutrons/cm^{2}s for 1.5 Å see also Fig. 5.2.), with respect to comparable cold time-of-flight spectrometers
- possibility of achieving a very high energy resolution, down to 2 μeV

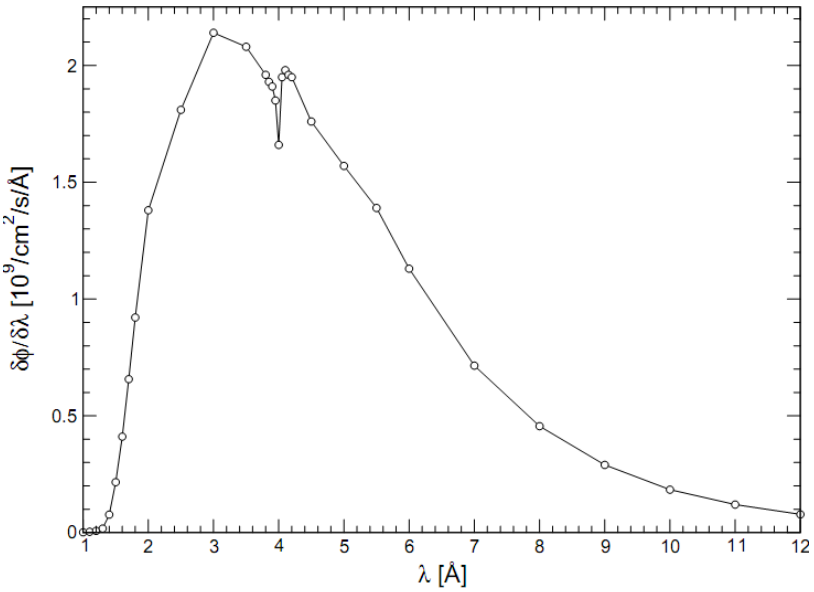

Fig. 5.2. Measured flux distribution at the time of flight spectrometer TOFTOF

5.2. Monte Carlo simulations

The future scientific perspective includes the investigation of magnetic systems as well as samples under extreme conditions (such as high-pressure cells electromagnetic and electrostatic levitators and magnetic or electric field). Since the typical samples for these investigations have dimensions of few mm^2, we aimed to focus the beam at the sample position on a cross section of 5 mm x 5mm with a significant gain.

5.2.1. Simulation setup

The present setup (see fig.5.1) imposes some geometrical restrictions: the neutron guide inside the chopper system cannot be changed, since this would affect the performances of the instrument. The only part that can be improved is the last one, just before the sample,

generally called the exchange guide, because it allows to switch between 2 options: a linear guide (represented in blue in fig. 5.3.a) and a collimator (in black in fig. 5.3.a).

For reaching the desired properties of the beam the best geometrical shape for the focusing nose replacing the linear collimator has to be decided (length and position). We started considering a non-linearly tapered nose (figure 5.3.b). For all the simulations we have chosen as initial wavelength 3Å due to the maximum in intensity for this value (see fig 5.2) and $d\lambda = 0.1$ Å.

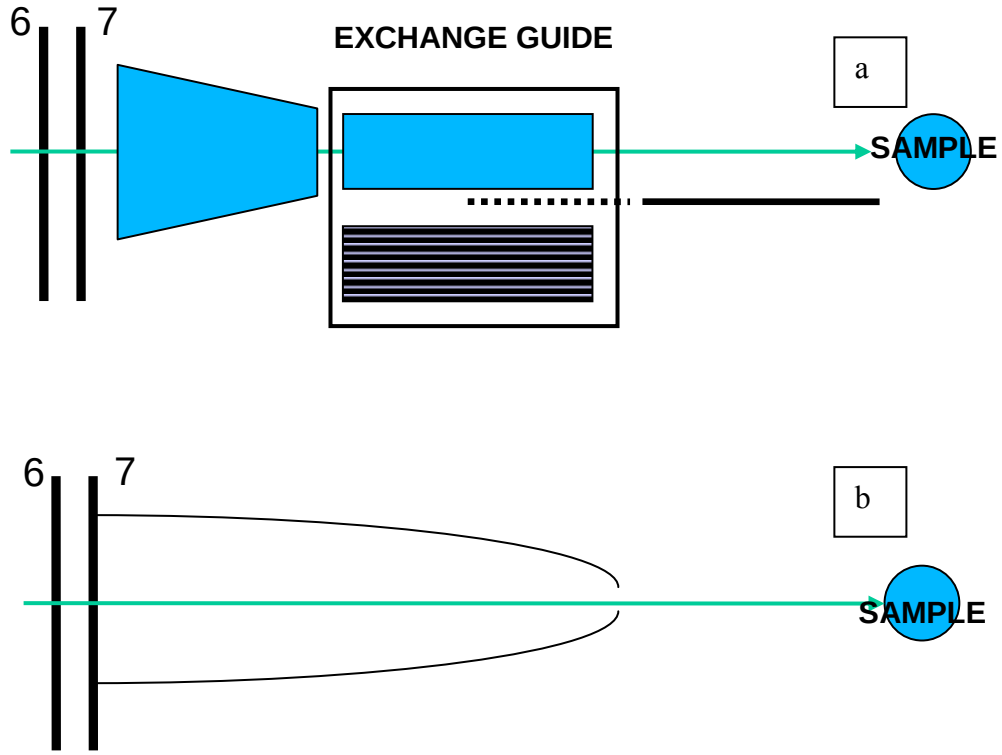

Fig. 5.3. Schematic of the simulation

We took into consideration 4 different options, whose shape and length looked like particularly convenient to match the dimensions of the existing neutron guide, the sample environment and the chopper system.

The parameters used for our simulations are defined as follows (see also fig 5.4):

H – height at the entrance of the elliptic guide

h - height at the exit of the elliptic guide

L – length of the guide

f_{in} – distance between the primary focal point and the entrance of the elliptic guide

f_{out} – distance between the secondary focal point and the exit of the elliptic guide

The correlation between these parameters and the factors a and b, describing an ellipse are given in chapter 5.2.3.

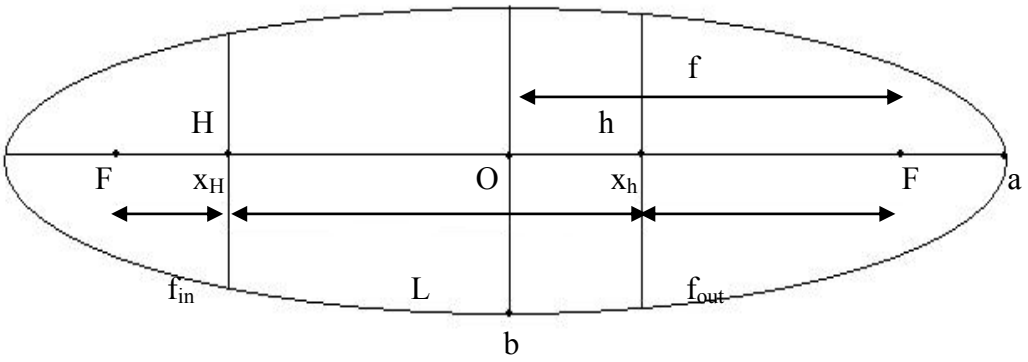

Fig. 5.4. Parameters which define the ellipse in McStas

For all four options f_{in} is fixed, whereas f_{out} is optimized in such a way to focus the beam on the sample (~~"ta~~pered component", vertical and horizontal curvature chosen independently).
The units of measurement that were used for the characterization of the properties of the guides are: neutron/(s·cm^2) for neutron flux density and neutron/s for intensity integrated over the corresponding area.
The 4 options have the following properties: f_{in} fixed at 21m, m value of the coating 6, elliptical shaped walls. The rest of the properties are summarized in the table below:

	Width at the entrance (mm)	Height at the entrance (mm)	Width at the exit (mm)	Height at the exit (mm)	Length (mm)	f_{out} (mm)
Option 1	23.00	55.15	10.50	25.30	783	199
Option 2	23.00	52.18	12.39	28.13	502	199
Option 3	23.00	55.15	17.87	42.85	400	582
Option 4	23.00	59.49	14.86	38.43	869	582

Table 5.1. Different options for simulation

Fig. 5.5 shows the differences among the 4 simulated options.

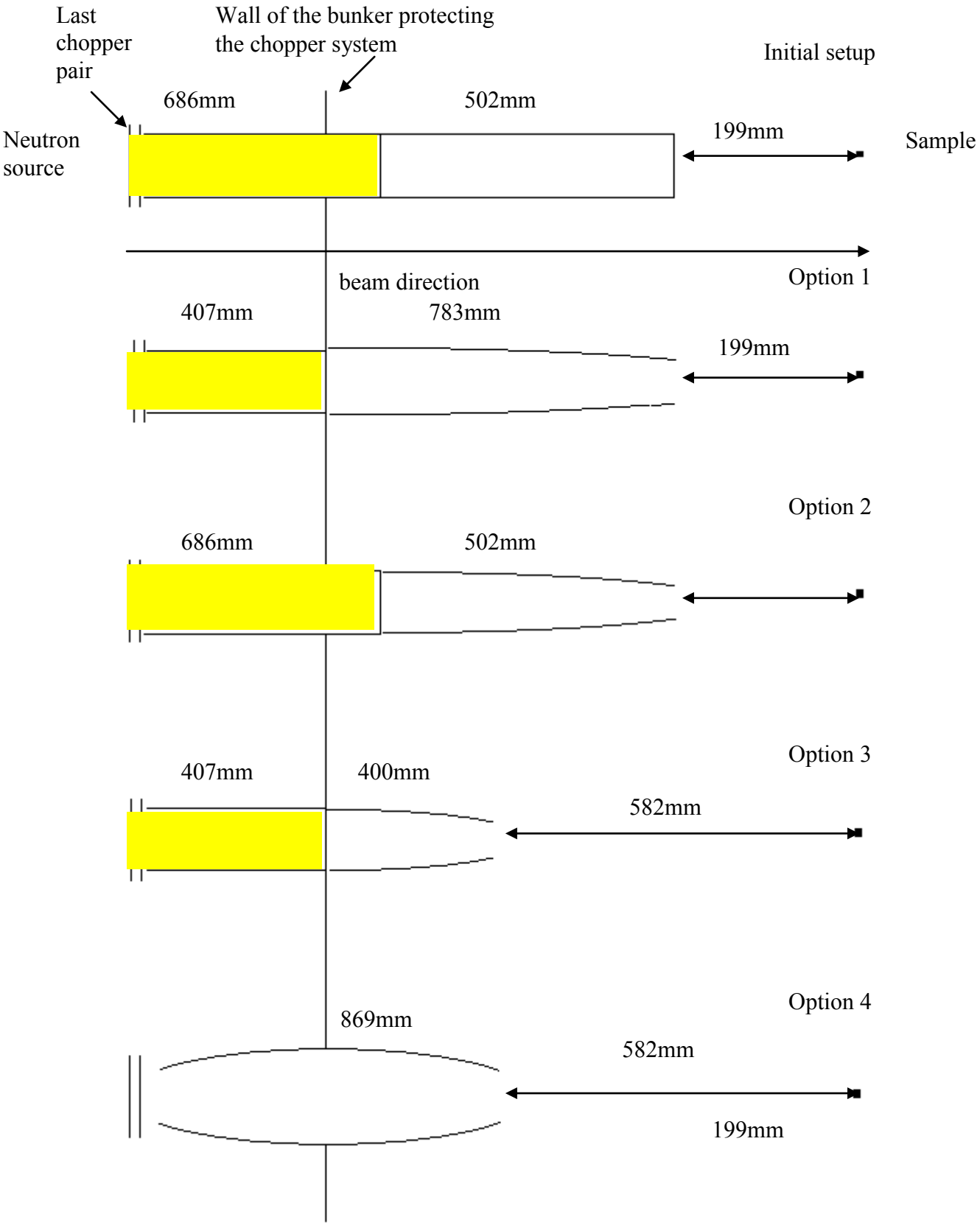

Fig. 5.5. Schematic view of the 4 options (in yellow are represented the existing parts)

5.2.2. Simulation results

The parameters used for comparing the performances of the different options with the existing exchange guide (initial setup) (see table 5.2) are:

1. neutron intensity integrated over the area satisfying I < 10% I_{max} and corresponding area [mm x mm]
2. neutron intensity integrated over the area satisfying I > 90%I_{max} and corresponding area [mm x mm]
3. homogeneity factor, defined as Area 10% / Area 90%
4. intensity integrated over an area of 1mm x 1 mm
5. intensity integrated over an area of 0.5 mm x 0.5 mm

option	Intensity integrated over 10%·I_{max} (neutrons/cm^2·s)	Area for 10%·I_{max} (mm x mm)	Intensity integrated over 90%·I_{max} (neutrons/cm^2·s)	Area for 90%·I_{max} (mm x mm)	Intensity integrated over 10mm x 10mm (neutrons/cm^2·s)	Intensity integrated over 5mm x 5mm (neutrons/cm^2·s)	Homogenity factor
initial setup	$4.95 \cdot 10^7$	25.0x 53.0	$7.26 \cdot 10^7$	15.0x 37.5	$6.86 \cdot 10^8$	$2.70 \cdot 10^9$	2.35
option1 sample/ foc point	$8.35 \cdot 10^7$	22.0x 32.0	$2.11 \cdot 10^8$	5.0x 6.0	$1.65 \cdot 10^{10}$	$7.80 \cdot 10^{10}$	23.46
option2 sample/ foc point	$8.41 \cdot 10^7$	18.0x 34.0	$1.99 \cdot 10^8$	4.0x 7.5	$1.87 \cdot 10^{10}$	$7.96 \cdot 10^{10}$	20.40
option3 sample/ foc point	$5.97 \cdot 10^7$	38.0x 58.0	$8.84 \cdot 10^7$	8.0x 10.0	$7.89 \cdot 10^9$	$3.30 \cdot 10^{10}$	27.55
option4 sample/ foc point	$5.44 \cdot 10^7$	42.0x 58.0	$8.39 \cdot 10^7$	10.0x 10.0	$7.53 \cdot 10^9$	$3.07 \cdot 10^{10}$	27.36

Table 5.2. Results of the first simulations

For all the simulations the value considered for the coating was m=6.
Comparing the 4 options with the present set-up of TOFTOF and the intensities obtained, option 2 turned out to be the best one with the following advantages:

- the exchange neutron guide is replaced by an elliptic nose, without need of cutting parts of the present neutron guide;
- intensity gain of the order of 2.5-3;
- the smallest area for integrated intensity satisfying $I > 90\%I_{max}$ among the 4 considered options.

In order to choose the optimal length of the guide, the length-dependence of the properties of the focal point has been studied (Table. 5.3)

Length of the guide (m)	Intensity integrated over $10\%\cdot I_{max}$ (neutrons/ $cm^2\cdot s$)	Area for $10\%\cdot I_{max}$ (mm x mm)	Intensity integrated over $90\%\cdot I_{max}$ (neutrons/ $m^2\cdot s$)	Area for $90\%\cdot I_{max}$ (mm x mm)	Intensity integrated over an area of 10x10mm (neutrons/ $m^2\cdot s$)	Intensity integrated over an area of 5x5mm (neutrons/ $m^2\cdot s$)
0.1	$1.36\cdot10^9$	32x58	$1.02\cdot10^8$	10x16	$1.67\cdot10^8$	$2.47\cdot10^8$
0.2	$1.47\cdot10^9$	30x56	$1.67\cdot10^8$	8x10	$2.00\cdot10^8$	$3.00\cdot10^8$
0.3	$1.50\cdot10^9$	28x54	$1.74\cdot10^8$	6x8	$2.53\cdot10^8$	$3.83\cdot10^8$
0.4	$1.65\cdot10^9$	26x48	$2.06\cdot10^8$	5x8	$3.11\cdot10^8$	$4.92\cdot10^8$
0.5	$1.12\cdot10^{10}$	18x34	$9.93\cdot10^8$	4x7.5	$9.89\cdot10^8$	$1.64\cdot10^9$
Initial	$1.06\cdot10^9$	28x53	$2.22\cdot10^7$	15x38	$1.77\cdot10^8$	$6.45\cdot10^7$

Table 5.3. Length-dependence of the properties of the focal point (intensities): keeping the wavelength fixed at 4 Å, changing the length and describing the properties of the focal point.

The length of the elliptical nose has to be kept at 500 mm due to the maximum in intensity for this value.
Dealing with elliptic mirrors, for given length and m-factor of the guide the position of the physical focal point (=minimum of the beam cross-section) doesn't straightforwardly coincide with the geometrical focal point of the ellipse described by f_{out}. It is indeed function of the wavelength (see fig.5.6) and of divergence and adaptive optics is therefore required.

Only in the case of the McStas simulations performed with a wavelength of 4 Å the physical focal point coincides with the geometrical focal point of the ellipse.

In order to determine the best geometrical shape of the elliptic nose we first characterized the wavelength-dependence of the position of the physical focal point by keeping the curvature of the component fixed (f_{out} = 199 mm), determining the position of the physical focal point in the wavelength-band 1.5-14 Å (sampling with a step of 0.5 Å).

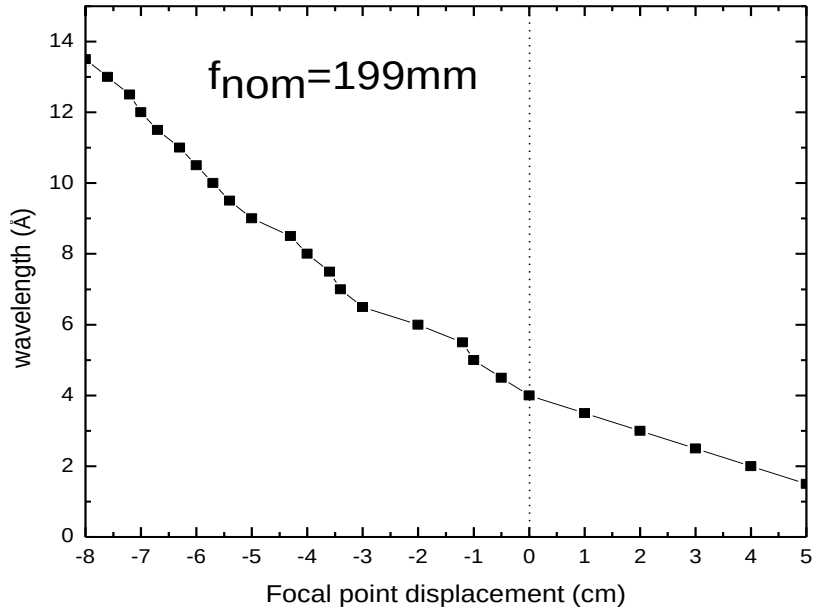

Fig. 5.6. Displacement of the physical focal point as a function of the wavelength. Zero displacement corresponds to the sample position (with a nominal focal length of 199 mm).

A dependency of the position of the focal point on the wavelength has been observed and only λ = 4 Å is focused at the sample position. Lower wavelengths are focused after the sample, whereas higher wavelengths before the sample. In order to keep the beam focused on the sample, one needs to change the curvature of the elliptic nose, by changing the f_{out} value.

Therefore, in a second moment, the curvature-dependence of the focal point has been characterized.

Table 5.4 shows the focal point displacement from the sample position for 4 significant wavelengths (1.5, 3, 6 and 12 Å) and at different f_{out} values.

Lambda (Å)	f_{out} (m)	Exit (mm x mm)	Displacement with respect to sample position
1.5	0.20	28.1 x 12.4	-0.05
1.5	0.25	30.4 x 13.4	-0.10
1.5	0.15	25.3 x 11.1	0.00
3	0.20	28.1 x 12.4	-0.02
3	0.17	26.5 x 11.7	0.00
6	0.20	28.1 x 12.4	0.02
6	0.23	29.6 x 13.0	0.01
6	0.24	30.0 x 13.2	0.00
12	0.17	26.5 x 11.7	0.09
12	0.20	28.1 x 12.4	0.07
12	0.25	30.4 x 13.4	0.03
12	0.23	29.6 x 13.0	0.02
12	0.27	31.2 x 13.7	0.00

Table 5.4. Variation of the f_{out} for different lambda values

Table 5.5. reports the features of the focal point for each one of these wavelengths, when the proper f_{out} value is chosen:

Lambda (Å)	f_{out} (m)	Intensity integrated over $10\%\cdot I_{max}$ (neutron/cm^2·s)	Area for $10\%\cdot I_{max}$ (mm x mm)	Intensity integrated over $90\%\cdot I_{max}$ (neutron/cm^2·s)	Area for $90\%\cdot I_{max}$ (mm x mm)	Intensity integrated over an area of 10mm x 10mm (neutron/cm^2·s)	Intensity integrated over an area of 5mmx5mm (neutron/cm^2·s)	Homogeneity factor
1.5	0.15	$1.51\cdot10^5$	20 x 36	$3.38\cdot10^5$	6 x 6	$1.98\cdot10^7$	$9.12\cdot10^7$	20.00
3	0.17	$6.40\cdot10^6$	16 x 25	$1.50\cdot10^7$	5 x 4	$1.02\cdot10^9$	$4.88\cdot10^9$	20.00
6	0.24	6.12•106	24 x 38	$1.45\cdot10^7$	6 x 8	$1.25\cdot10^9$	$5.60\cdot10^9$	19.00
12	0.27	$9.53\cdot10^5$	36 x 50	$2.17\cdot10^6$	8 x12	$2.08\cdot10^8$	$8.80\cdot10^8$	18.75

Table 5.5. Simulation results

There are 2 ways of obtaining the focusing at the same position for all wavelengths:

1) to displace the elliptical nose along the beam direction. The results for these simulations are presented in the following and
2) adaptive optics, which we will discuss later.

Due to the large range of lambda and change in curvature, one solution could be to use adaptive optics only for the lambda range 1.5 to 6 Å, whereas shifting the nose for focusing λ in the range 6 -12 Å. Therefore taking the optimized shape for 6 Å (f_{out} = 0.24 m), we translated the elliptical nose in the sample direction and determined the shift (of the order of mm up to 3 cm) necessary to bring the focus on the sample for each wavelength in the range 7-12 Å, (sampling with a step of 1 Å). For each one of this wavelength we calculate all the usual integrated intensities on the sample position, after imposing the shift of the elliptic nose required for focusing on the sample.

Wavelength (Å)	f_{out}(m)	Exit (mmxmm)	focal point (m)	shift (mm)
7	0.24	30x13.2	0.2	5
8	0.24	30x13.2	0.2	7
9	0.24	30x13.2	0.2	9
10	0.24	30x13.2	0.2	16
11	0.24	30x13.2	0.2	19

Table 5.6. Shift of the elliptic nose for different lambda values

The corresponding shifts are presented in Table 5.6. The corresponding intensities at sample position are presented in Table 5.7.

Wave length (Å)	Intensity integrated over 10%·I_{max} (neutrons/cm^2·s)	Intensity integrated over 90%·I_{max} (neutrons/cm^2·s)	Intensity integrated over an area of 10x10mm (neutrons/cm^2·s)	Intensity integrated over an area of 5x5mm (neutrons/cm^2·s)	shift (mm)
6	$1.12•10^9$	$1.16•10^8$	$1.25•10^9$	$5.60•10^9$	no shift
7	$9.19•10^8$	$1.06•10^8$	$9.26•10^8$	$4.12•10^9$	5
8	$7.39•10^8$	$6.07•10^7$	$6.73•10^8$	$2.96•10^9$	7
9	$7.16•10^8$	$7.01•10^7$	$5.92•10^8$	$2.48•10^9$	9
10	$4.72•10^8$	$4.53•10^7$	$3.54•10^8$	$1.52•10^9$	16
11	$3.79•10^8$	$4.13•10^7$	$2.62•10^8$	$1.08•10^9$	19
12	$3.05•10^8$	$2.85•10^7$	$1.93•10^8$	$8.10•10^8$	25
12	$3.21•10^8$	$3.69•10^7$	2.08•108	$8.80•10^8$	no shift

Table 5.7. Intensities for different lambda values

The integrated intensity over an area of 10 mm x 10mm is plotted in fig 5.7 together with the shift necessary for each lambda value. The integrated intensity for λ = 12 Å over 10mm x 10mm without a shift is higher then the intensity calculated for the same area in the case of the shift of 25 mm (see table 5.7).

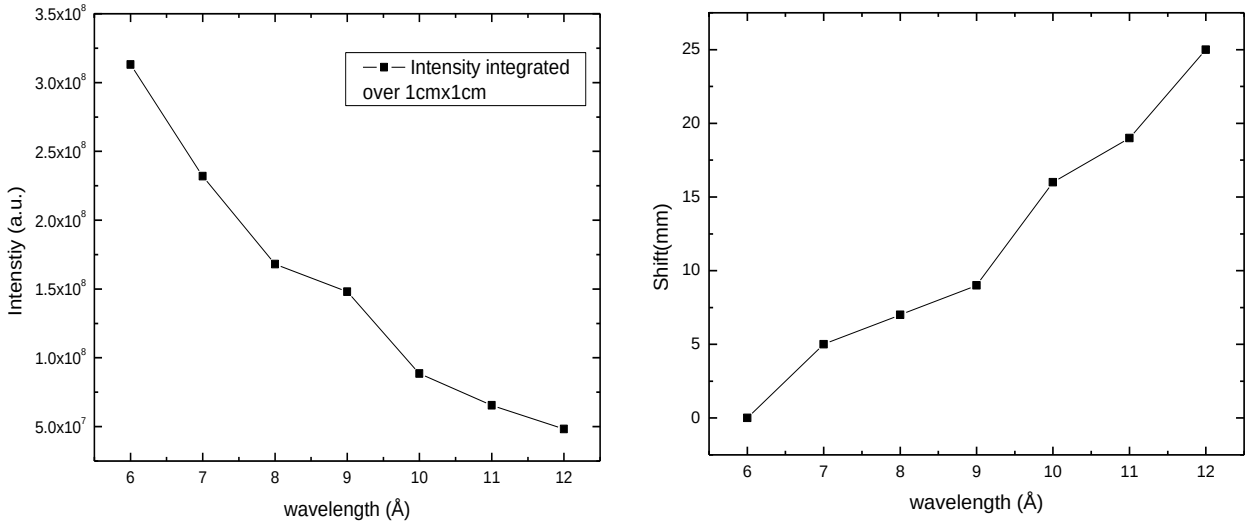

Fig. 5.7. The integrated intensity over an area of 10 mmx10 mm and shift necessary for each lambda value

The gain for the different lambda values are presented in the fig. 5.8. The gain was calculated as the report between the integrated intensity over
10 mm x 10 mm and 5 mm x 5 mm respectively for option 2 and the initial case for different lambda values. A maximum gain of around 3 was found for the integrated intensity over an area of 5 mm x 5 mm.

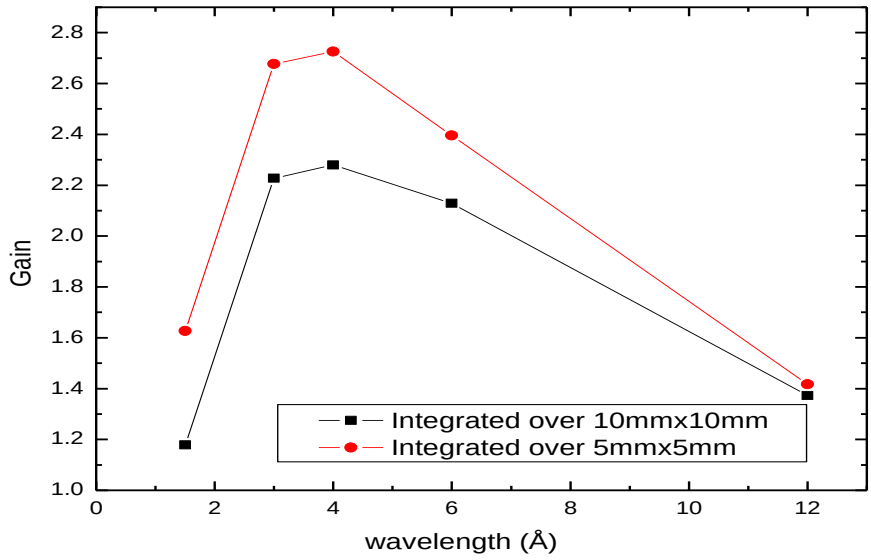

Fig.5.8. Intensity gain vs. lambda

5.2.3 Calculation of the radius of curvature

In order to build the neutron guides with the curvature resulting from the simulations, it is necessary to calculate the relationship between the parameters needed for the simulations (f_{out}, f_{in}, L) and the usual parameters used for an ellipse (a, b) in order to calculate the radius of curvature for the bent walls.

For the simulations an ellipse was used with the f_{in} value of 21.1m. Due to this large value we can approximate the ellipse with a parabola with the equation:

$$x = ay^2 \quad 5.1$$

where the factor a is given by:

$$a = 4L/(H^2 - h^2) \quad 5.2$$

with L the length of the parabolic part, H is the height at the entrance of the parabola and h the height at the exit.

The curvature of the parabola is then given by:

$$k = 2a/[1 + (2ay)^2]^{3/2} \quad 5.3$$

with a given above.

For an ellipse given by equation:

$$\frac{x^2}{a^2} + \frac{y^2}{b^2} = 1 \quad 5.4$$

With a,b and f as in fig 5.4.

$$L + f_{in} + f_{out} = 2f \quad 5.5$$

To obtain the relation between a,b and f the parameters of the ellipse and H, h, L and f_{in} and f_{out} we have to impose to the two point to belong to the ellipse:

$$\frac{{x_H}^2}{a^2} + \frac{H^2}{b^2} = 1 \quad 5.6$$

$$\frac{{x_h}^2}{a^2} + \frac{h^2}{b^2} = 1 \quad 5.7$$

with:

$$x_h - x_H = L$$

$$x_H = f_{in} - f$$

$$x_h = f - f_{out} \quad 5.8$$

From this we obtain the parameter b:

$$b^2 = H^2 + \frac{(H^2 - h^2)(f_{in} - f_{out} - L)^2}{4L(f_{in} - f_{out})} \quad 5.9$$

and a:

$$a^2 = b^2 + f^2 = \frac{(f_{in} - f_{out} - L)^2}{4} + \frac{H^2 L(f_{in} - f_{out})}{H^2 - h^2} \quad 5.10$$

The radius of curvature in a point $P(x_P,y_P)$ is given by:

$$R = a^2b^2(\frac{x_P^2}{a^4} + \frac{y_P^2}{b^4})^{\frac{3}{2}} \quad 5.11$$

5.2.4. Adaptive optics

In order to model the focusing nose, we calculated the deformation of a plate in the simple case fixed at one end and pressed by a force F at the other end. We then compared the action of a momentum instead of that of a force.

Mathematically the curvature (the inverse of the radius of curvature) is given by the formula:

$$\frac{1}{\rho} = \kappa = \frac{y''}{(1+(y')^2)^{\frac{3}{2}}} \quad 5.12$$

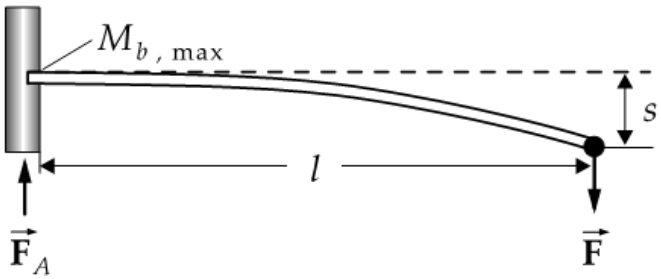

Fig. 5.9. Pressing with a force at the free end of a plate

For a bar fixed at one end and pressed with a force at the other end (fig. 5.9.) the tangent of the angle and the vertical difference with respect to the straight plate at each point are expressed respectively as [VanH01]:

$$y' = \frac{Fl^2}{2EI}\left[\frac{2x}{l} - \left(\frac{x}{l}\right)^2\right] \quad 5.13$$

$$y = \frac{Fl^3}{6EI}\left[3\left(\frac{x}{l}\right)^2 - \left(\frac{x}{l}\right)^3\right] \quad 5.14$$

In this case the curvature is given by:

$$\kappa = \frac{\frac{Fl(1-x)}{EI}}{\left[1+\left[\frac{Fl^2}{2EI}\left[\frac{2x}{l}-\left(\frac{x}{l}\right)^2\right]\right]^2\right]^{\frac{3}{2}}} \quad 5.15$$

The equation of the deformation of a plate fixed at one end and pressed by a force F at the other end is [Laep01]:

$$w(x) = \frac{Fl^3}{3EI}\left[1 - \frac{3x}{2l} + \frac{1}{2}\left(\frac{x}{l}\right)^3\right], \text{ with } x = 0 \rightarrow \Delta l = \frac{Fl^3}{3EI} \quad 5.16$$

with Δl being the maximum deformation of the plate and l the length of the guide l = 500mm. This transforms the equation in:

$$y = H - \Delta l\left[1 - \frac{3x}{2l} + \frac{1}{2}\left(\frac{x}{l}\right)^3\right] \quad 5.17$$

We calculate the profile of the guide (height and width at each point) by subtracting from the initial dimensions the deformation given by equation 5.16 and by replacing the unknown parameters force, inertia momentum and elasticity modulus by the maximum deformation, calculated as the difference between the dimension at the entrance minus the dimension at the exit (the dimensions at the exit are obtained from the simulations for each wavelength):

$$\Delta l = H - h \quad 5.18$$

The radius of curvature can be calculated in this case as:

$$R = \frac{(1+y'^2)^{\frac{3}{2}}}{y''} \quad 5.19$$

where:

$$y' = \Delta l\left[\frac{-3}{2l} + \frac{3}{2l}\left(\frac{x}{l}\right)^2\right]$$

$$y'' = \Delta l\frac{3x}{l^3} \quad 5.20$$

and substituting these into the expression for R we obtain:

$$R = \frac{\left[1+\left[\frac{3\Delta l}{2l}\left(1-\left(\frac{x}{l}\right)^2\right)\right]\right]^{\frac{3}{2}}}{\frac{3\Delta l x}{l^3}} \quad 5.21$$

x (mm)	Δl (mm)	Length (mm)	radius(m)
230	4.83	500	25.8841426
330	9.25	500	13.5167215
500	22.68	500	5.51146384

Table 5.8 Radius of curvature for different positions

In the table 5.8 are calculated the values for the radius of curvature at different positions (x) along the plate.

As seen in the equation 5.17, when one presses on a plate at one end and keeps the plate fixed at the other end the dependency of the vertical deformation from the horizontal position x goes with the third power exponent differently from what expected for the equation of a parabola or an ellipse. However we have plotted these curves and fitted with parabolic functions (red curves) as presented in figure 5.10. The 4 different curves are for 4 different heights at the exit of the guide of a length of 500 mm (the height at each point is calculated as

the difference between the initial height of the guide which is 52.18 mm and the deformation y given by the equation 5.17).

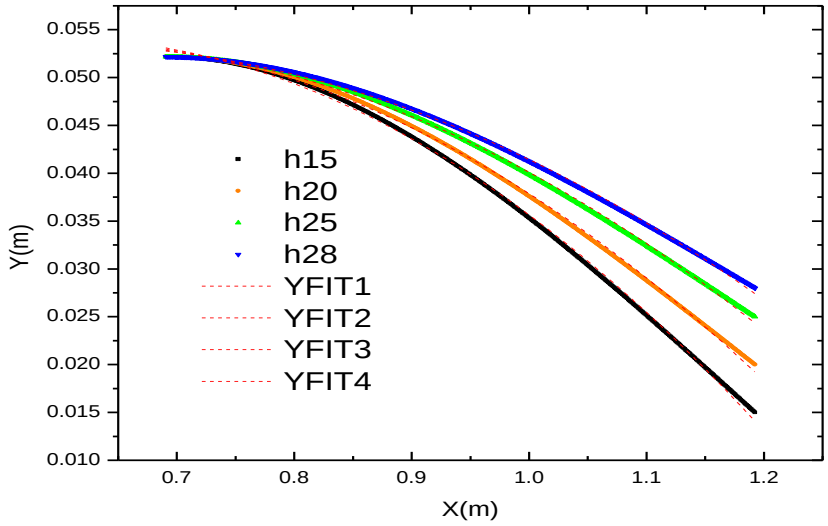

Fig. 5.10. Fit with parabolic functions

The fitting parabola is given by the equation: $y = A+Bx+Cx^2$ with the parameters:

Height (mm)	A	B	C
15	0.01568	0.13059	-0.11064
20	0.02059	0.11303	-0.09576
25	0.02550	0.09547	-0.08088
28	0.02844	0.08493	-0.07195

Table 5.9. Parameters for fitting parabola

After these considerations, we implemented in McStas a new guide shape, whose walls follow equation number 5.22, that has a parabolic shape:

$$y(x) = H - (H - h)\left[1 - \left(\frac{x}{l}\right)\right]^2 \qquad 5.22$$

We observe the properties of the beam and compare them with the ones obtained in the case of an elliptically shaped guide. In the following graph (fig 5.11) we present the comparison at 4 Å between the integrated intensity over an area of 10 mm x 10 mm in the center of the PSD detector placed at 0.2 m away from the exit of the guide (in red) and the integrated intensity over an area of 5 mm x 5 mm respectively (in green) and for the initial setup, as well as for an elliptic shape, a parabolic shape and for the walls following the equation 5.22 with different

values for the height at the exit of the guide (for example eqh28 means a height at the exit of 28 mm).

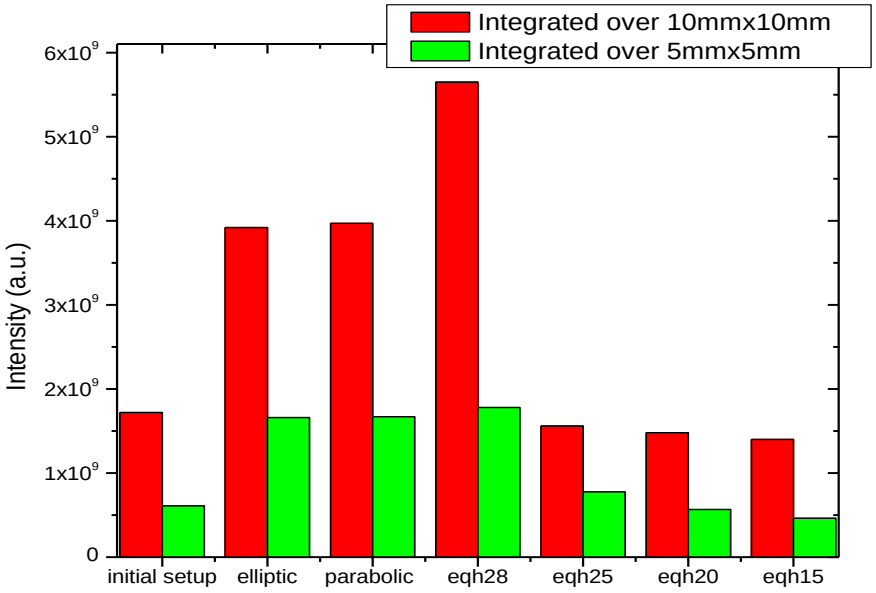

Fig. 5.11 Intensity comparison for different simulated cases

These calculations were made in order to choose the optimal height at the exit of the guide and therefore the optimal curvature. The same procedure was followed for lambdas 1.5 Å to 12 Å. The intensity as function of the wavelength for initial case (initial setup already existing at TOFTOF) in the following marked with a, walls having an elliptic shaped (named case b) and the walls following the equation 5.22. (named case c) are presented in the figures 5.12 up to 5.14 calculated for an area of 10 mm x 10 mm and 5 mm x 5 mm.

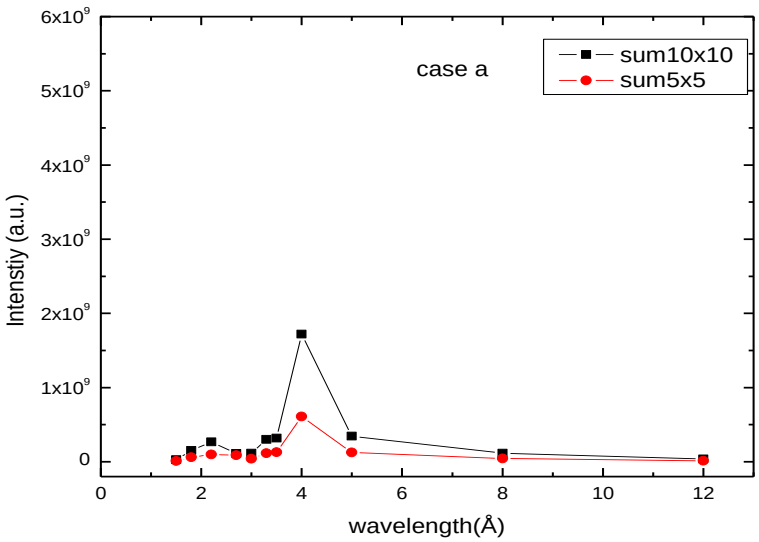

Fig 5.12. Intensity as function of lambda for the initial case

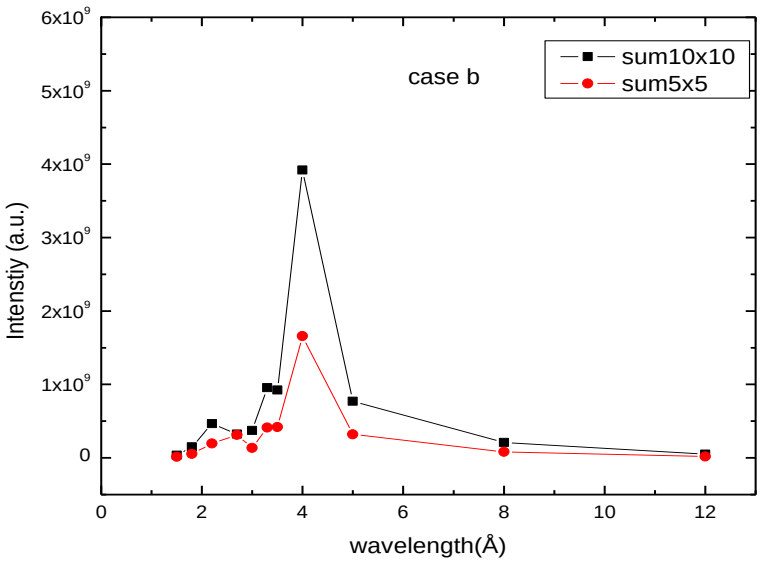

Fig 5.13. Intensity as function of wavelength for elliptic case(b)

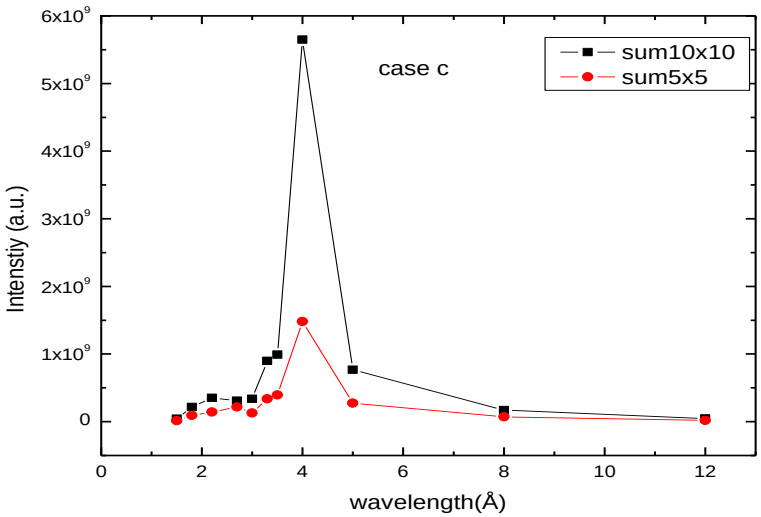

Fig 5.14. Intensity as function of wavelength for the equation case(c)

The intensity gain for both cases (elliptic and equation) calculated as the intensity in the different cases divided by the intensity in the initial case, are presented in the graphs 5.15 and 5.16:

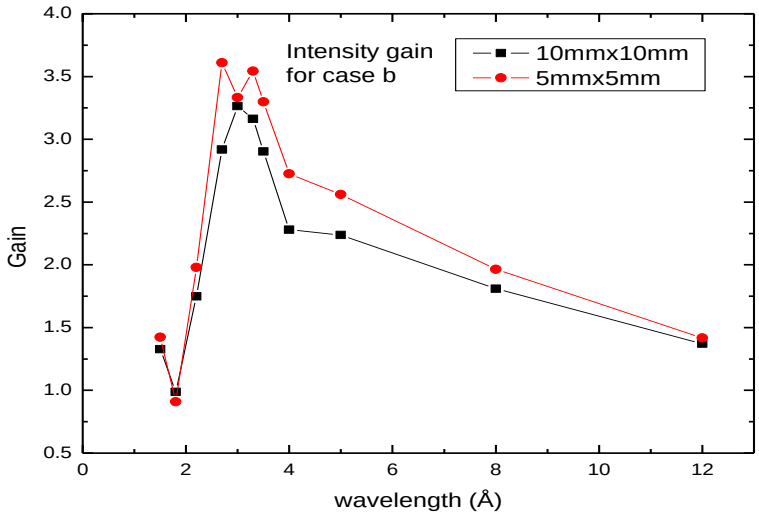

Fig 5.15. Intensity gain for the elliptic case (b)

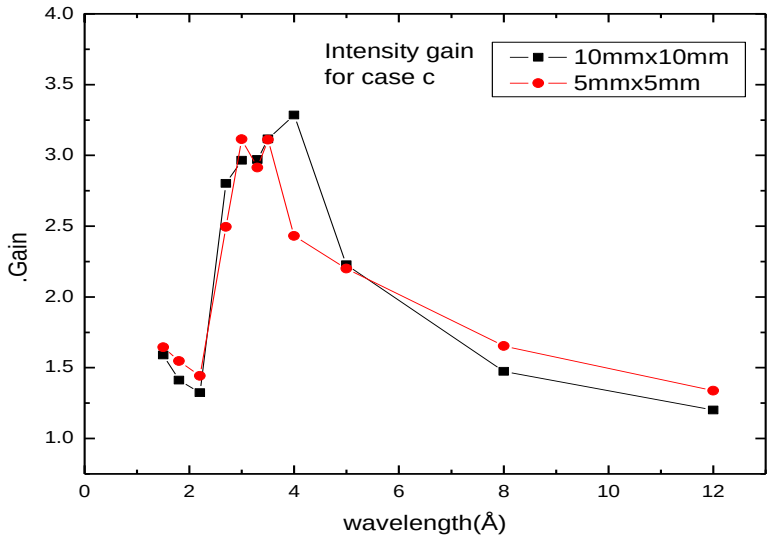

Fig 5.16. Intensity gain for the equation case(c)

Furthermore, the divergence obtained in the case when the walls follow the equation is homogenous and much smaller than in the case of the elliptic case (see fig. 5.17. This indicates as favorable the construction of the guide with the possibility to ~~a~~dapt" the walls by simply pressing at the end of the guide.

PSD at 0.2m from the exit Divergence

parabolic shape given by equation 5.22 height at the exit 28 mm

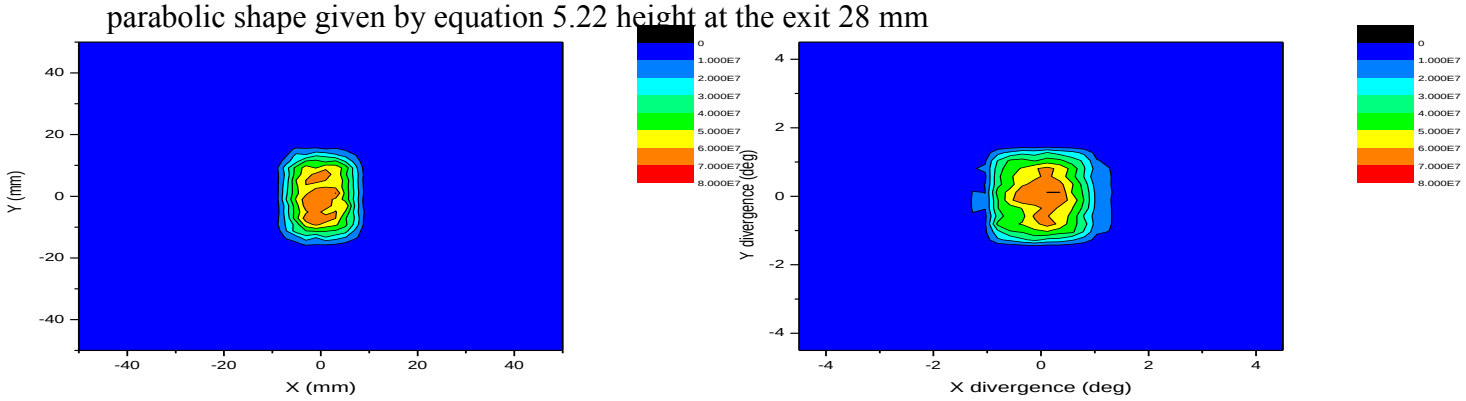

parabolic shape given by equation 5.22 height at the exit 20 mm

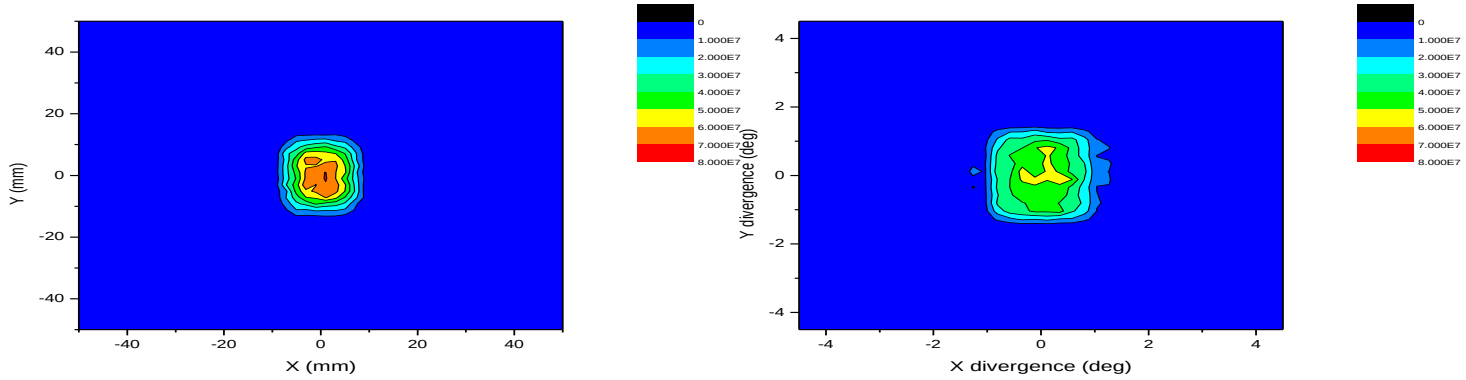

parabolic shape given by equation 5.22 height at the exit 15 mm

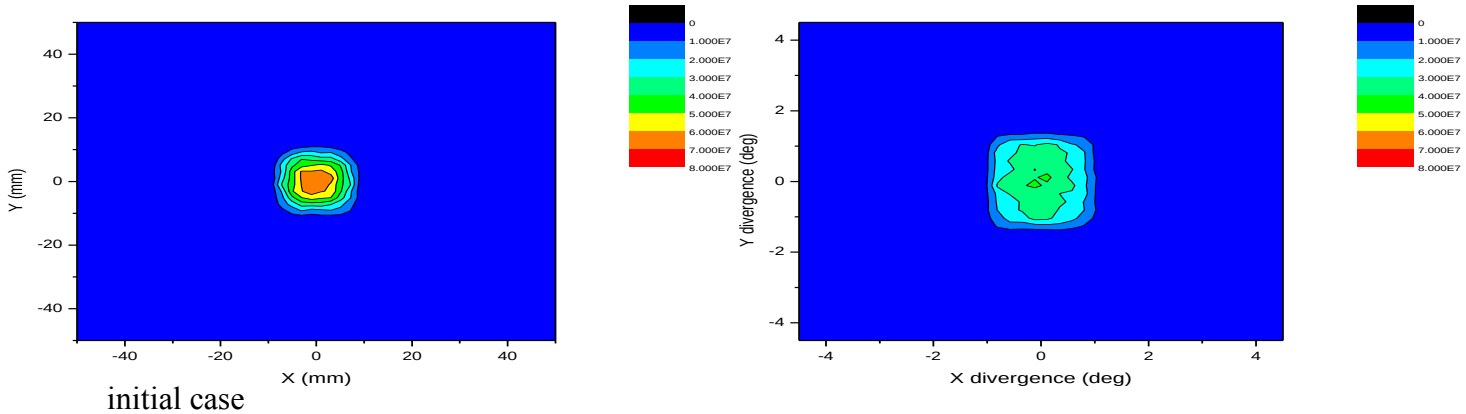

initial case

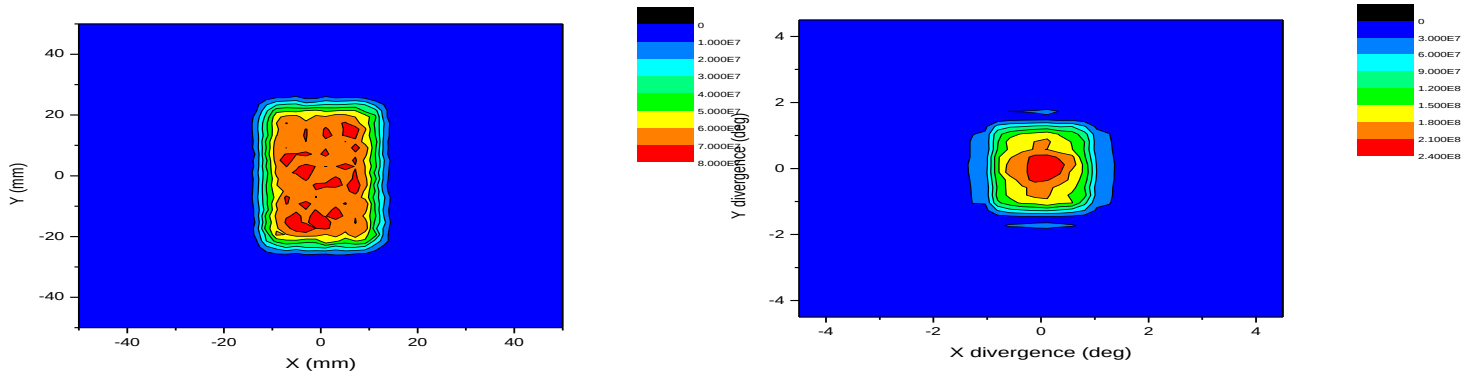

Fig. 5.17. PSD and Divergence monitor for Lambda 4 Å and different shapes of the guide

5.3. Prototype construction

The simulation results presented in chapter 5.2.4 have shown promising results for constructing a prototype to be tested at the time of flight Spectrometer TOFTOF, where it should bring a gain of a factor 3 in intensity at the focal position for a wavelength of 4 Å.

5.3.1. Prototype design

Taking into account the geometrical restriction at the instrument (see anex 5.a) we have designed the following prototype. The drawing in fig.5.18.a is made for a wavelength of 1.5 Å (the maximum curvature), therefore the guide is completely ~~–e~~losed" (no gaps appear) .
The prototype is surrounded by 4 rods made out of 10mm glass used for stabilizing the structure and for mounting the motors. The rods are glued together with pieces of glass into a rectangular shape to make the entrance dimensions fixed and immobile. The other end of the glass is free and can be moved with the help of motors. The thickness of the glass for the 495mm long movable glass plates was chosen to be 3 mm for a better waviness, elasticity and stability of the system.

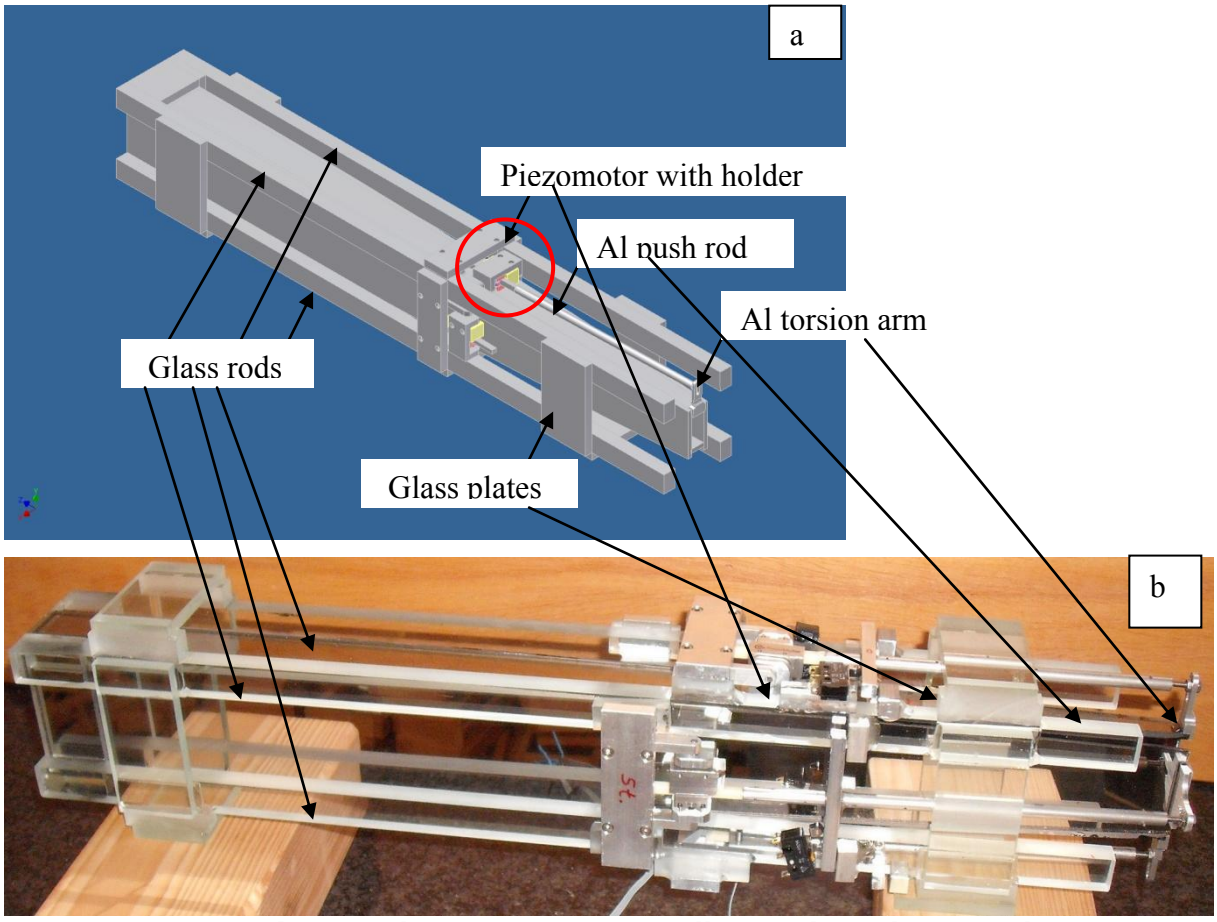

Fig.5.18. Prototype design with piezomotors (a) in yellow vs. the real protype (b)

For placing the motors additional glass pieces were glued at 140 mm away for the exit of the prototype (the 140 mm were chosen due to geometry consideration: adjusting screws that already exist). Each motor is fixed to the external glass case by a glass holder (mounted parallel to the guide walls and connecting two adjacent glass rods). The motor, moving, presses an Al rod, whose end pushes of small vertical Al plate, orthogonal to the Al rod and glued at the end of the guide wall (see fig.5.20). These motors, operated by a dedicated software, offer the possibility to adapt the curvature of the guide (see also chapter 5.3.5).
The motors have also the possibility to rotate around their own axis (see fig. 5.19.) and a rotation point is located where the Al push rod presses on the torsion arm. This prevents the rod to bend and the motor to remain blocked.

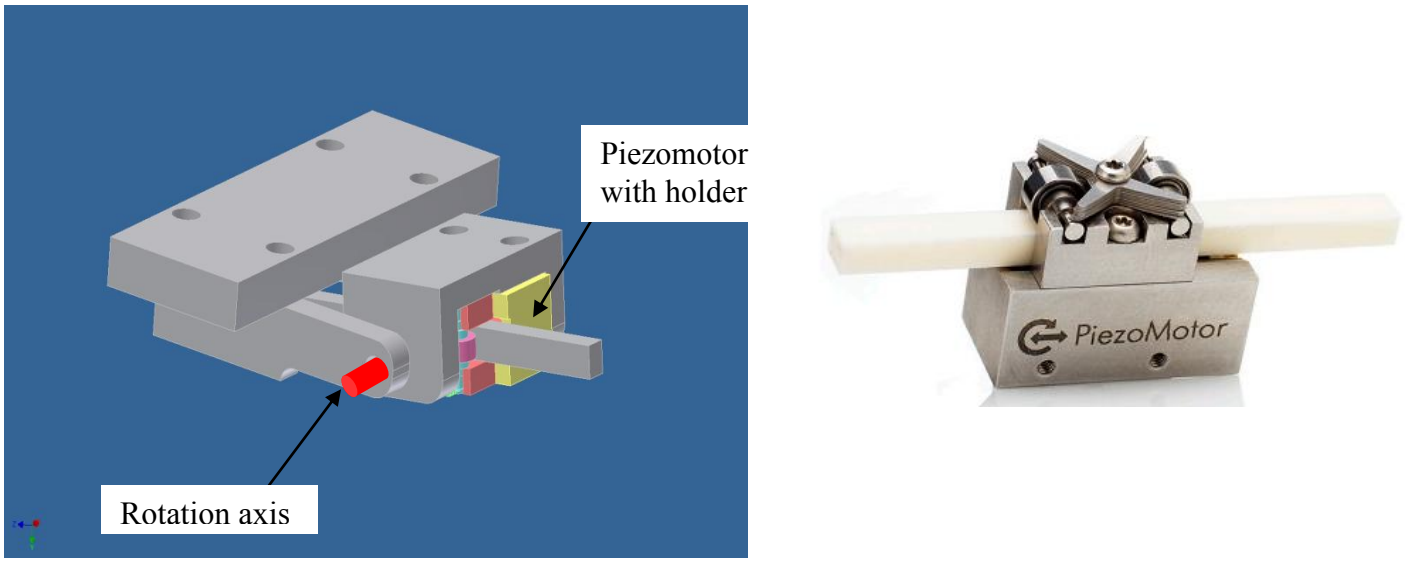

Fig.5.19. Motor holder as detail (red circle) from fig.5.18 and real motor

In fig 5.20. is represented schematically one plate of the prototype together with the forces that act on it. The force F_0 presses under the angle α. Therefore we have two components of the force: one perpendicular to the torsion arm creating the momentum $M = h \cdot F_0 \cos\alpha$ and a second one parallel to the torsion arm $F = F_0 \sin\alpha$, which also contributes to the bending of the plate. To eliminate the effect of this last force we have chosen the dimension H and h in such a way that the rod is parallel to the plate. Using this momentum we obtain the desired shape of the glass. The coating of the walls of the prototype was m=3.5.

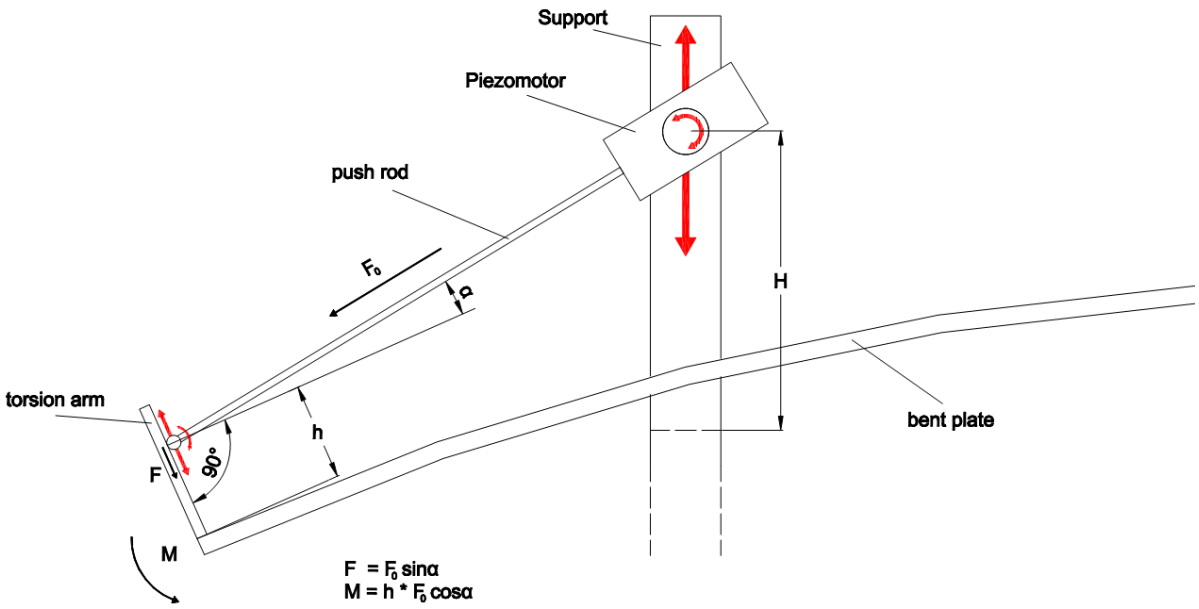

Fig. 5.20. Schematic representation of the glass with the motor holding. The double red arrows mark the adjustment screws that allow us to vary H and h and fix them after finding the optimum values.

5.3.2. Testing the geometry – characterization of optical properties

Before assembling the prototype, the 4 walls have been tested separately. First of all we tested the elastic behavior of the glass support and then we tested the coated glass. The properties of the coating were tested separately.

5.3.2.a. Using the height-profilometer

We have fixed one end and we have pressed using the Al road onto the torsion arm in order to modify the curvature of the glass like during its normal operation (as shown in fig.5.19). Using a height-profilometer we measured the height of the curved glass at different positions. The tests were performed for the wavelengths 1.5 and 12 Å and the results are plotted in fig. 5.21 and 5.22. The values measured with the height profilometer are plotted in red and the theoretical curves in black (theoretical curve is the equation 5.22). There is a very good match between the theoretical and the measured curve (as seen from the difference between the theoretical and the measured curve plotted in blue), showing that using this method we simulate very well the action of a momentum on to the wall and that the wall reproduces very well the desired shape.

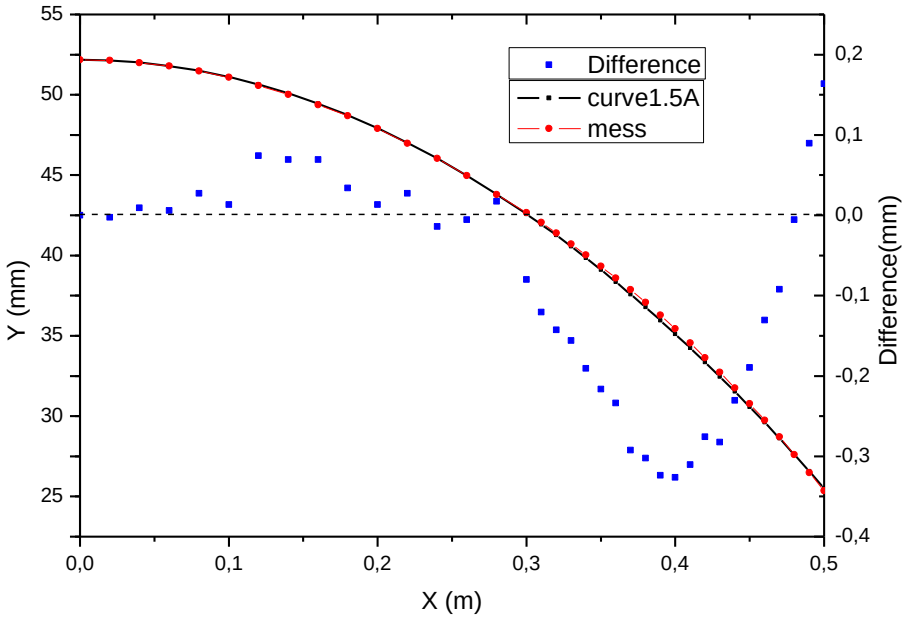

Fig.5.21 Theoretical (black) and measured curve (red) for a wavelength of 1.5 Å

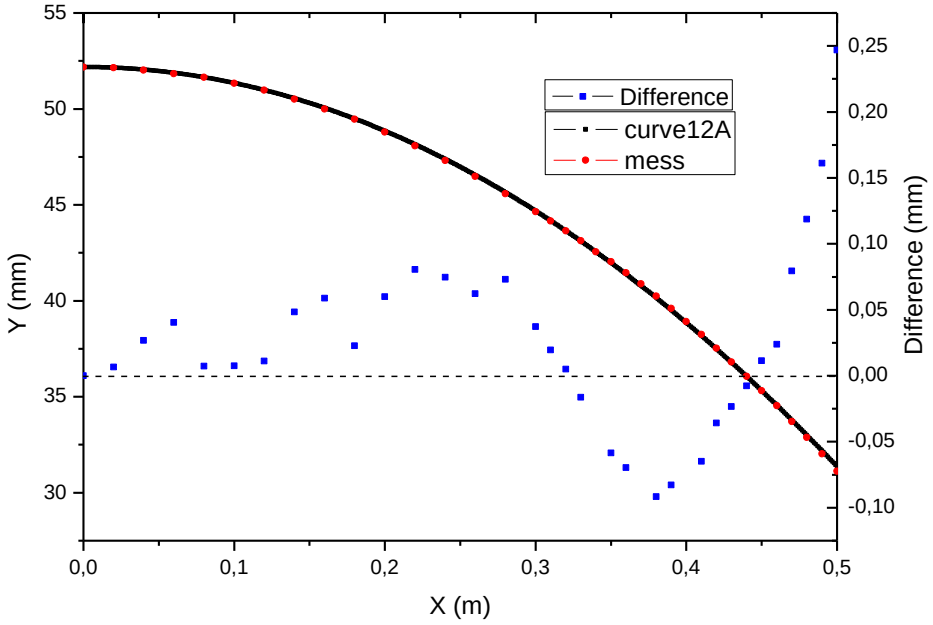

Fig. 5.22 Theoretical (black) and measured curve (red) for a wavelength of 12 Å

Using this method we have determined the parameters needed to reach the proper curvature: the thickness of the glass: either 2 or 3 mm, the distance at which we should press on to the Al tortion arm (h) that together with the length of the road with which we press and H gives us the tilting angle of the road.

5.3.2.b. Using the theodolyte

All of the above measurements were performed with uncoated pieces of glass. For a non invasive characterization of the coated walls we have measured the curvature with a theodolyte.

For the first test we kept the Al screw road used in the previous tests and pressed on the torsion arm (without using motors) and characterized the coated glass with a theodolyte. We have measured a plate 495 mm long, starting 30 mm away from the entrance of the plate and measuring 15 points. Calculating the correlation between the angles measured by the theodolyte and the tangent at each point at the theoretical curve (the first derivative of the equation 5.22) we were able to compare the theory with the experiment.

Lambda (Å)	H (mm)	h (mm)	Difference (H-h)/2 (mm)
1.5	52.18	25.3	13.44
3	52.18	27.6	12.29
6	52.18	29.5	11.34
9	52.18	30.6	10.79
12	52.18	31.2	10.49

Table 5.10. Maximum deformation (calculated as height at the entrance H minus height at the exit h) for the upper and lower plates

Lambda (Å)	H (mm)	h (mm)	Difference (H-h)/2 (mm)
1.5	23	11.16	5.92
3	23	12.19	5.405
6	23	12.8	5.1
9	23	13.23	4.885
12	23	13.6	4.7

Table 5.11. Maximum deformation (calculated as height at the entrance H minus height at the exit h) for the side plates

We have represented in the following diagrams the comparison between theory and experiment for the lower and upper plate where we have the larger deformations from the horizontal (listed in the tables 5.10 and 5.11 in comparison with the maximal deformations for the plates placed on the side of the prototype). If we calculate the first derivative (tangent) from equation 5.22 we obtain:

$$y'(x) = 2(H-h)\frac{1}{l}\left[1-\frac{x}{l}\right] \qquad 5.23$$

From equation 5.23 one can calculate the angle at each point for the theoretical case.

The standard deviation from the theoretical formula (equation 5.23) presented in graphs 5.23 and 5.24 correspond to a standard deviation from the theoretical curve of under 0.1mm.

Lambda 1.5 Å

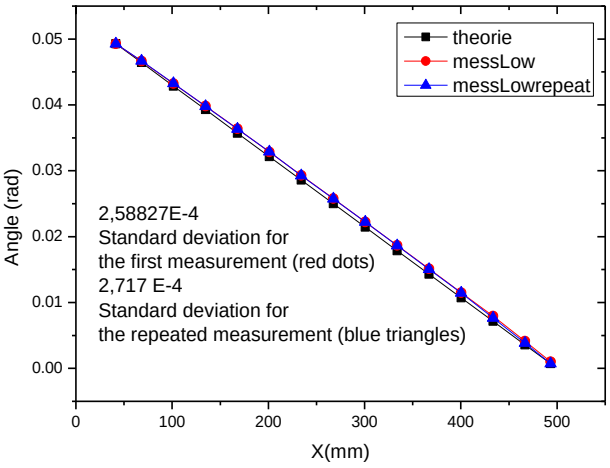

Lambda 12 Å

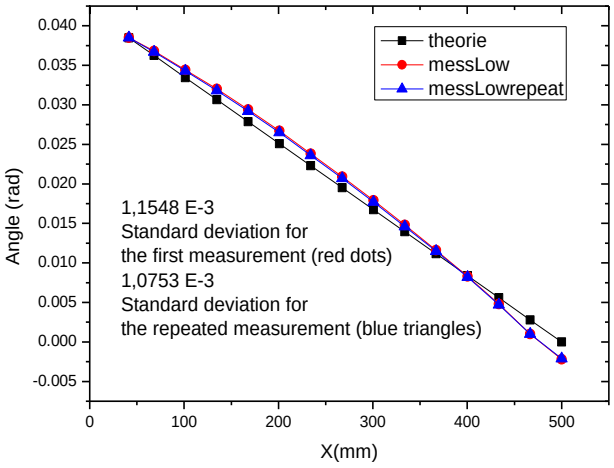

Fig. 5.23. Comparison between theory and measurements with theodolyte for the lower plate

Lambda 1.5 Å

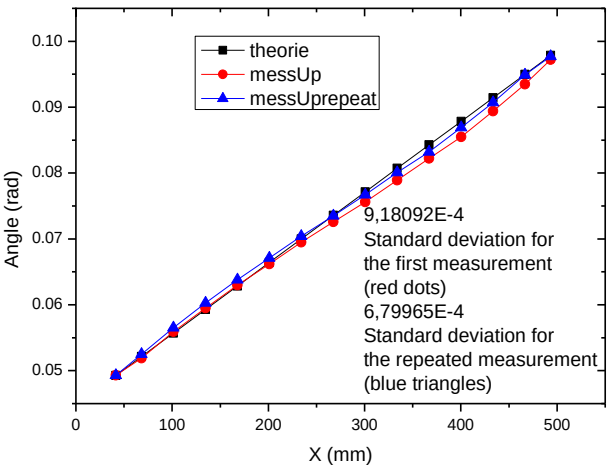

Lambda 12 Å

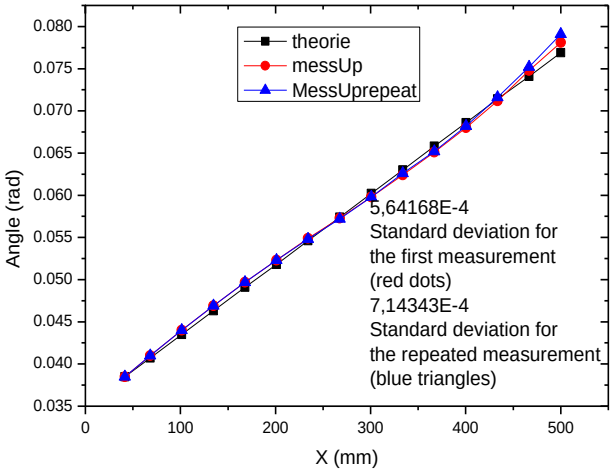

Fig. 5.24. Comparison between theory and measurements with theodolyte for the upper plate

In all of the above graphs the black curve represents the angle in radian calculated from the theoretical equation, while the red and the blue curves are 2 measurements made with the theodolyte for the different wavelengths. The standard deviation from the tangent values is also depicted. This deviation from the theoretical curve leads to a decrease of less then 0.5%

in intensity in the focal point (simulated with McStas program) and is therefore neglectable. There is also a loss in intensity caused by the gap that appears when we ~~–o~~pen" the guide, meaning when we go from 1.5 Å (the biggest curvature) to 12 Å (the lowest curvature).
If we consider all walls curved for 1.5 Å no gaps appear (the guide is ~~–c~~losed").
Moving all 4 walls to the configuration for 12 Å we have gaps appearing in the horizontal and in vertical position. We have approximated the losses that result from these gaps as the report between the area that remains ~~–o~~pened" (calculated as the difference between the integral of the equation for the curvature of the guide for 1.5 Å and 12 Å) and the area corresponding to the horizontal or vertical plate. With respect to this approximation we have obtained:

$$I_{losshorizontal} = \frac{A_{1,5} - A_{12}}{A_{horizontal}} = 2{,}22\%$$

$$I_{lossvertical} = \frac{A_{1,5} - A_{12}}{A_{vertical}} = 3{,}61\% \qquad 5.24$$

That makes a total loss of intensity due to the appearing gaps of:

$$I_{losstotal} = \frac{I_{losshorizontal}A_{horizontal} + I_{lossvertical}A_{vertical}}{A_{horizontal} + A_{vertical}} = 2{,}64\% \qquad 5.25$$

This means that we will expect a gain of 2,92 instead of 3 at focal point (calculated for 4 Å)
We have also tested the reproducibility of our measurements by making more measurements and the standard deviations show that the measurements can be very well reproduced. From these measurements we were able to confirm the established parameters for each wall, meaning the height where the motor will be placed and the position where this will press. The table 5.12 summarizes these parameters for each wall.

Wall	H (mm)	h (mm)	L (mm)
Up	17	18	150
Side	22	21	170
Down	18	15	150

Table 5.12 Parameters for each wall. The parameters H, h, and L are defined in fig. 5.20

5.3.4. Corrections

The equations that we have used so far for simulations were those for a plate of rectangular shape and without taking into account the gravity. We have therefore analyzed the influence of taking into account the real shape of the glass and the gravity compared to the results obtained using the theoretical curve.

5.3.4.a. Due to the real shape of the glass

The equation from which our formula for the deformation is:

$$w''(x) = -\frac{M_y(x)}{EI_y} \qquad 5.26$$

where w is the deformation, M the momentum, E the elasticity modulus and I the second area momentum. For a rectangular plate the second area momentum is defined as:

$$I_y = \int_A z^2\, dA \qquad 5.27$$

$$I_y = \frac{b \cdot h^3}{12} = A \cdot \frac{h^2}{12} \qquad 5.28$$

is a constant and therefore we obtain the equation:

$$M(x) = -EIw''(x) \qquad 5.29$$

That leads to the theoretical equation that we have used: (see also chapter 5.2.4)

$$y(x) = Factor\left[1 - \left(\frac{x}{l}\right)\right]^2 \qquad 5.30$$

In the case of a trapezoid shaped glass (the real form of the glass) we have:

$$I_y = h^3 \cdot \frac{(b_1+b_2)+2 \cdot b_1 \cdot b_2}{36 \cdot (b_1+b_2)} \qquad 5.31$$

That leads to a difference from the theoretical curve (equation 5.22) presented in fig.5.25 for the side walls and in fig.5.26 for the up and down wall.

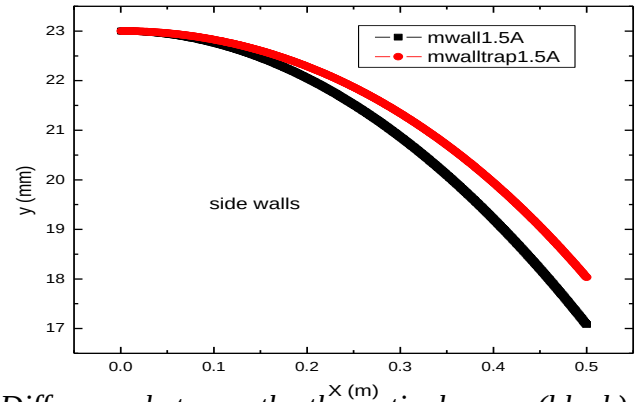

Fig. 5.25 Difference between the theoretical curve (black) and the theoretical curve obtained in case of considering a trapezoidal shape of the glass (red) for the side walls

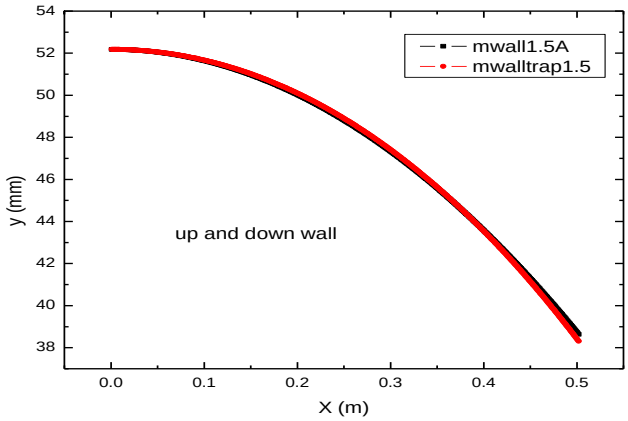

Fig. 5.26. Difference between the theoretical curve (black) and the theoretical curve obtained in case of considering a trapezoidal shape of the glass (red) for the up and down walls

The difference between the two graphs in fig. 5.25 and 5.26 is due to the different geometries of the plates: at the entrance for the up and down wall 23 mm and for the side walls 52.18 mm as well as at the exit that must be inserted in equation 5.31 (the entrance and the exit dimensions constitute the b1 and b2 values for the trapezoidal form).

5.3.4.b. Due to gravity

For calculation of deformation in case of the gravity (which influence only the up and down wall) we have measured the curvature of the glass (using the theodolyte) placing it on the side and than as it should be placed up or down. The difference between these two measurements is presented in fig.5.27.

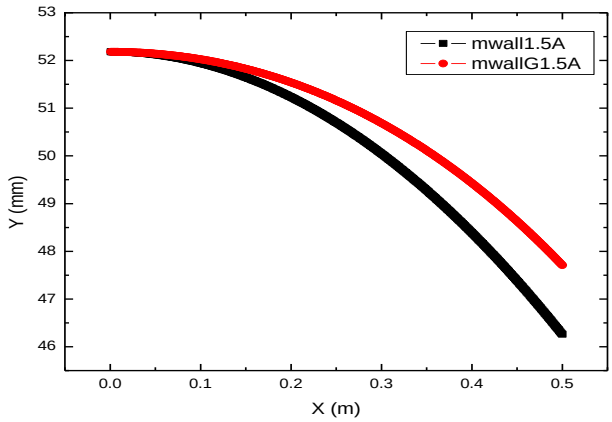

Fig. 5.27. Difference between the theoretical curve (black) and the theoretical curve obtained in case of considering the gravity effect (red) for the up and down walls

Taking these deformations into account we have simulated and evaluated the evolution of the beam using McStas. The results are presented in table 5.13 and fig 5.28. First graph in fig. 5.28 presents the beam distribution in focal point (a PSD placed at focal point) obtained from simulating a focusing guide which walls following the equation 5.22 and having a rectangular shape and no gravity effect is considered. The next two graphs show the beam distribution in case of considering first a trapezoidal shape of the glass and then add the effect of gravity.

a) Theoretical curve with rectangular shaped walls and no gravity effect –ideal case

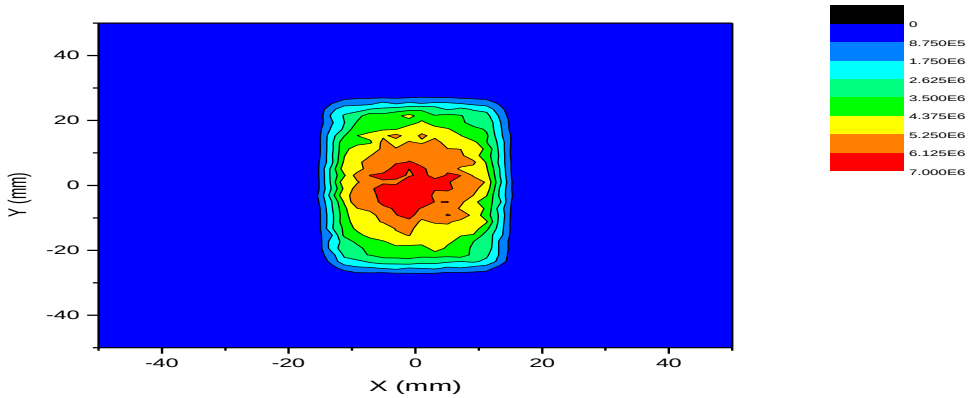

b) Theoretical curve with trapezoidal shaped walls and no gravity effect

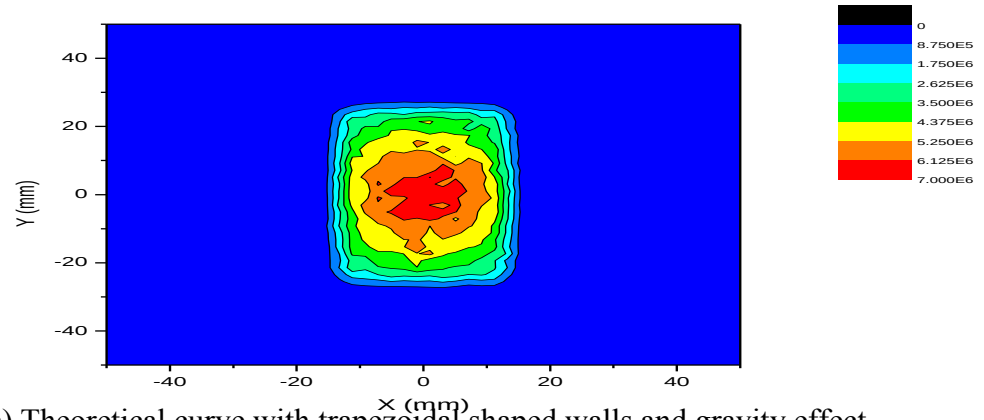

c) Theoretical curve with trapezoidal shaped walls and gravity effect

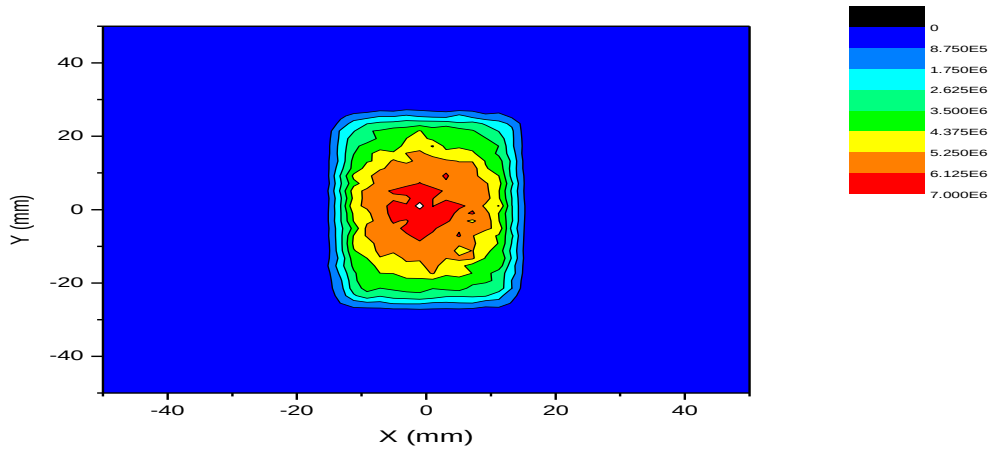

Fig. 5.28 Comparison of PSD detectors placed at focal point for different shapes of the glass

Integrated Intensity over 10mmx10mm	Integrated Intensity over 5mmx5mm	FWHM(mm)	
$1.59 \cdot 10^8$	$5.85 \cdot 10^7$	12.5	Ideal case
$1.63 \cdot 10^8$	$5.86 \cdot 10^7$	12.3	Trapez
$1.57 \cdot 10^8$	$5.91 \cdot 10^7$	12.7	Trapez plus gravity

Table 5.13 Intensity and FWHM calculated for the above simulations

Therefore comparing the ideal case of rectangular shaped glass and no gravity effect with the case when we consider the walls having a trapezoidal shape and we add the gravity effect, we observe no significant difference in intensities (they are comparable within the error bars given by the McStas simulation program) or in FWHM. This allows us to continue the simulations considering the walls following the equation obtained for the ideal case (equation 5.22).

5.3.5. Inserting the motors

The Piezomotors were supplied by the company with a controlling software. They can be operated by setting the waveform and the number of steps.
For our calibration we have chosen the option that offers us the possibility to vary the speed between 60 and 10 000 μm/s and is optimized for the maximum force of the motor.
As optimum speed we chose 60 μm/s, that is the minimum speed in the interval given by the waveform. With this speed we can run between 0 and 200 000 microSteps which corresponds to a movement between 0 and 37 500 μm. For each wavelength we have varied the number of steps keeping the speed constant for reaching the theoretical curves.

5.3.5.a. Determination of the parameters for each wavelength

Each motor is operated in such a way to reach a reference curvature and then to move back to the wished curvature, thus preventing back clash. We have then ran the motors at the end of each end point and then we have calculated the number of steps to run back to reach each curvature. Each motor has a different force therefore the parameters and the equations will also differ. In annex 5.c is presented the procedure for operating each wall: the number of steps necessary to reach the reference, the speed and the measurements with the theodolyte.
Plotting the number of steps as a function of the wavelength we obtained the equations below that allows then to calculate the number of steps for each desired wavelength for each wall:

$$y = 1782.72-976.23\cdot\exp(-x/6.3) \quad \text{(equation for the upper wall)} \qquad 5.32$$

$$y = 944.38-1099.54\cdot\exp(-x/3.42) \quad \text{(equation for the lower wall)} \qquad 5.33$$

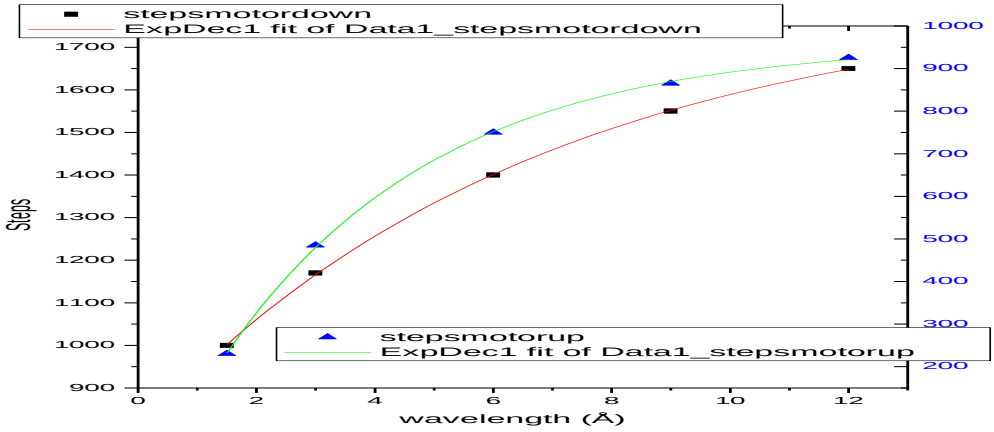

Fig. 5.29 Calibration of step number as function of lambda for the up and down wall

$$y = 943.93 + 21.28 \cdot x \quad \text{(equation for motor left)} \qquad 5.34$$

$$y = 893.14 + 21.56 \cdot x \quad \text{(equation for motor right)} \qquad 5.35$$

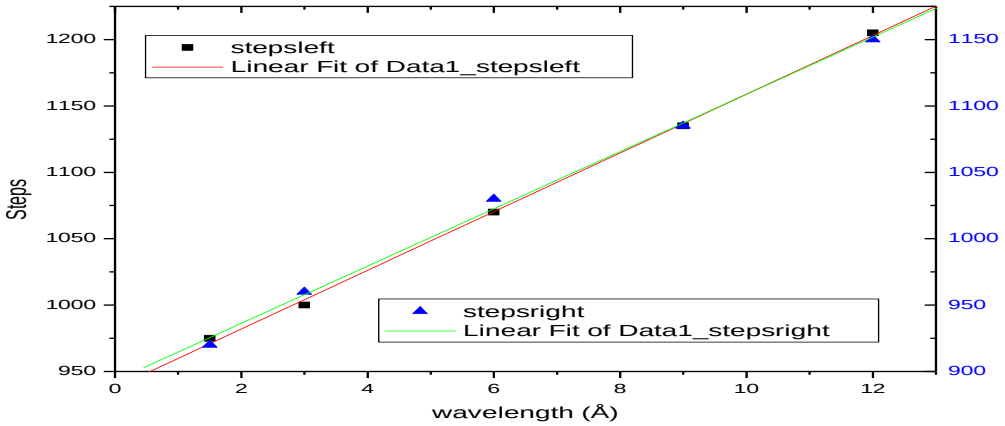

Fig. 5.30. Calibration of step number as function of lambda for motor left

5.3.5.b. Estimation of errors

We have performed more than one measurement to test the reproducibility of our runs (for a wavelength of 1.5 Å and for the upper wall since there we had the larger deformations). 5 of these measurements are presented in fig.5.31 in comparison with the tangent of the theoretical curve (equation 5.23).

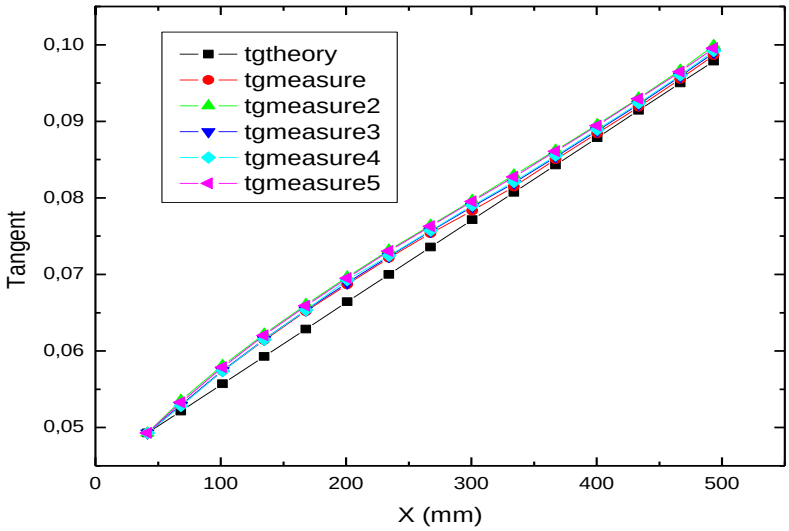

Fig.5.31 Repeated measurements with the theodolyte in comparison with the theoretical curve (black)

We have calculated the standard deviation from the theoretical curve (in black in fig.5.31) and we have chosen measurement number 2 (see table 5.14) as heaving the maximum difference from theory. We have calculated the maximum difference for the factor F (where F is the factor in the equation that defines our curvature $y = F\cdot (1-x/L)^2$, that we can calculate from the equation of the tangent $tg = 2\cdot F/L\cdot (1-x/L)$ represented in fig.5.31)

	Measurement 1	Measurement 2	Measurement 3	Measurement 4	Measurement 5
Standard deviation (rad)	$7{,}47636\cdot 10^4$	$8{,}42\cdot 10^4$	$7{,}35057\cdot 10^4$	$7{,}51602\cdot 10^4$	$8{,}24751\cdot 10^4$
Factor (mm)	0,37382	0,42081	0,36753	0,3758	0,41238

Table 5.14 Standard deviation for the different measurements

With the factor difference calculated as in the table above we were able to calculate the difference from the theoretical curve (equation 5.23) and to implement this into a Monte Carlo simulation.

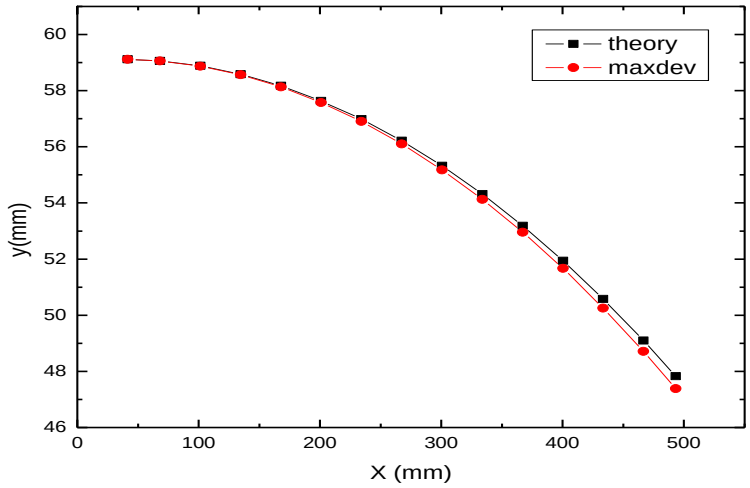

Fig.5.32 Comparison between the curve with maximum difference (red) with theory (black)

In the fig.5.32 one can see the difference from the theory for all the measurements with the maximum deviation. All the other measurements are between the black line (theory) and the red curve (the maximum difference). For this measurement in red (that has the largest difference) we have performed a Monte Carlo simulation to observe the variations in intensity and in dimensions of the beam

The results of the simulation are in the fig.5.33 on the left being the beam at sample position for the walls described by the curve that has the maximum difference from the theory and on the right the beam (a position sensitive detector placed at the sample position) in case that the walls of the guide are described by the theoretical curve (the simulations were performed for a wavelength of 1.5 Å)

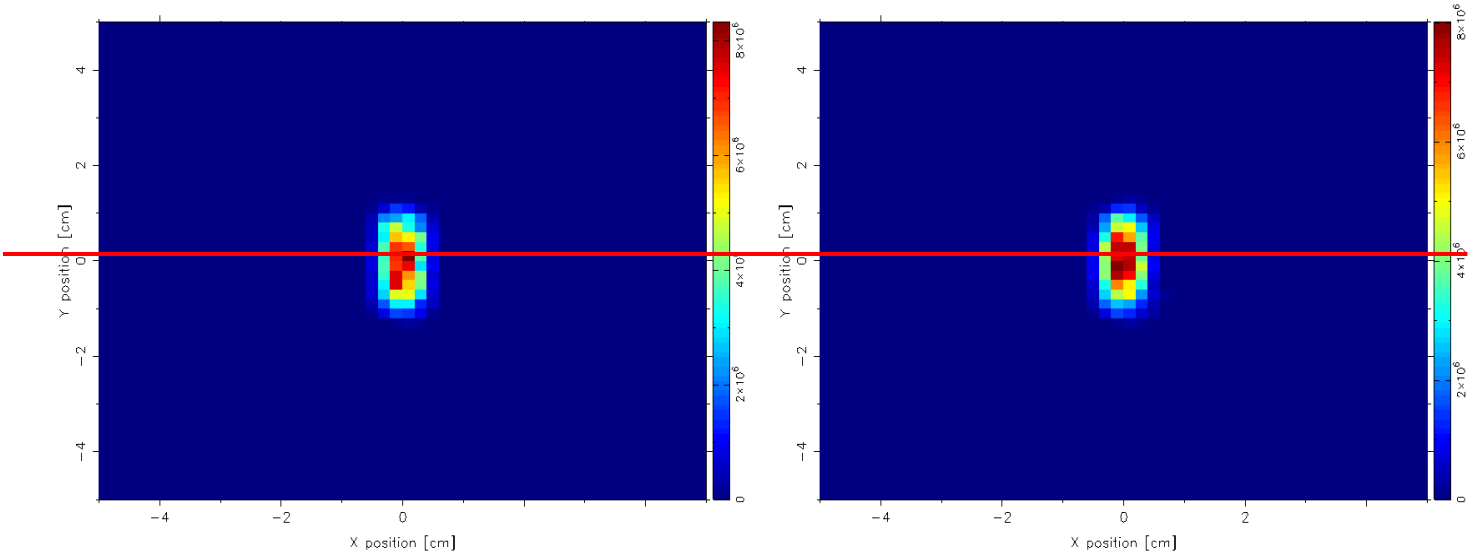

Fig.5.33. PSD in focal point for the 2 cases described above

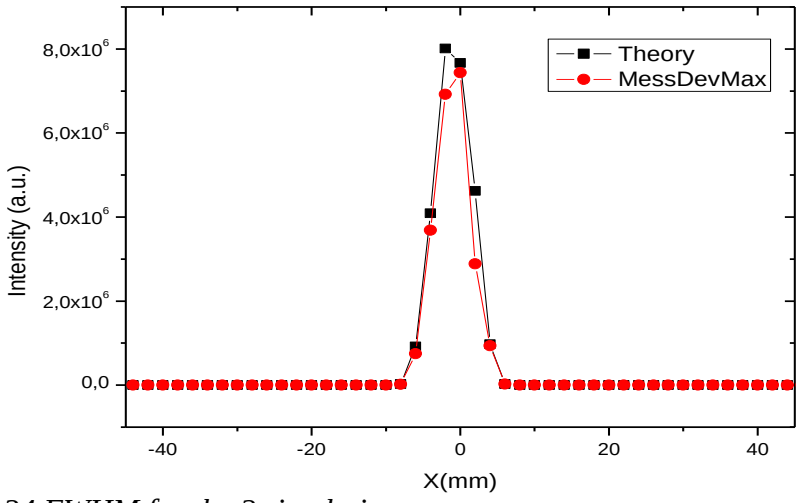

Fig.5.34 FWHM for the 2 simulations

By performing horizontal cuts through the simulated images (fig 5.33) we were able to determine the FWHM (fig. 5.34) and we have also calculated the integrated intensity over the entire area of the detector as well as for areas of 5 mm x 5 mm and 10 mm x 10 mm. The results are summarised in the table 5.15:

	Integrated intensity over the area of the entire detector (a.u.)	Integrated intensity over an area of 10mmx10mm (a.u.)	Integrated intensity over an area of 5mmx5mm (a.u.)	FWHM (mm)
Theory	$2.002 \cdot 10^8$	$1.15 \cdot 10^8$	$5.74 \cdot 10^7$	6.1
Measurement Max. Difference	$1.950 \cdot 10^8$	$1.10 \cdot 10^8$	$5.42 \cdot 10^7$	5.8

Table 5.15. Intensities and FWHM

There is therefore almost no difference either in intensity or in the width of the beam if we take into account the largest difference possible resulting from the measurements

Another way to evaluate the losses in intensity is by using the McStas program. All of the simulations presented in chapter 5.2.4 were made for both up and down and left and right following either the given equation or the equation of the ellipse.

To simulate the losses that will appear, we have kept fixed the curvature of the left and right walls, according to the requirements for lambda 4 Å (corresponding to a height of the guide of 28.1 mm) and we have changed the upper and lower walls both for ellipse and equation case (up and down focusing). Analogously we kept fixed the curvature of the upper and lower walls optimized for 4 Å (corresponding to a height of the guide of 12.4 mm) and varied the

f_{out} value for the left and right walls (left and right focusing). The results of the gains obtained are presented in the figures below

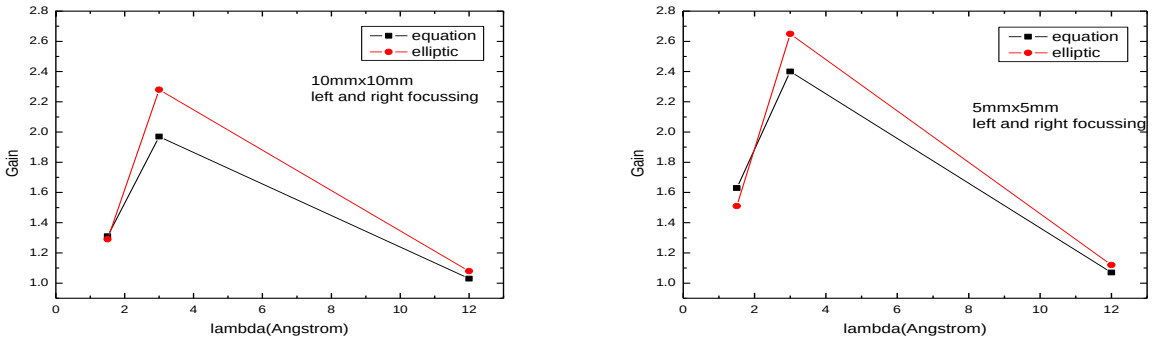

Fig.5.35. Gains obtained for the case of horizontal focusing for λ = 4 Å

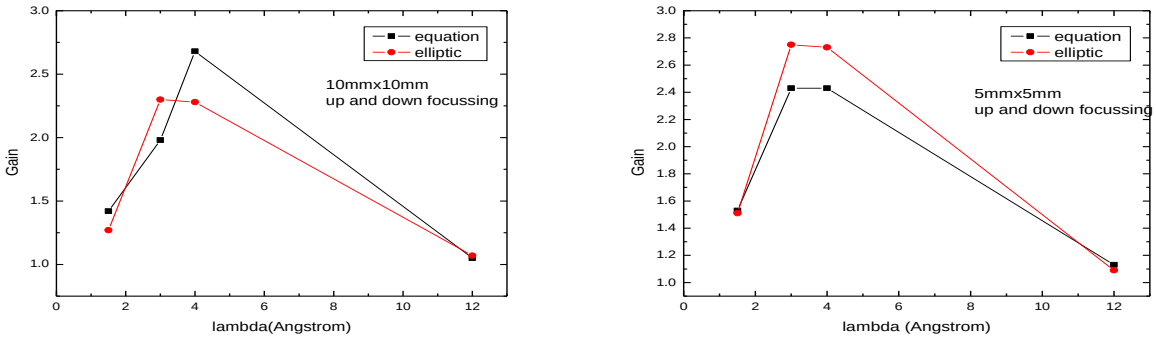

Fig.5.36. Gains obtained for the case of vertical focusing λ = 4 Å

Although the gains are comparable in both focusing cases, we have continued with focusing in vertical direction and we fixed the left and right walls to follow the parabolic shape given by equation 5.22 for lambda 1.5 Å corresponding to a width of the guide of 11.16 m (the largest curvature for the left and right walls) and varied the f_{out} value for the up and down walls. The gains for elliptic and equation case for the 2 integrated areas of 10 mm x 10 mm and 5 mm x 5 mm are presented in the following graphs:

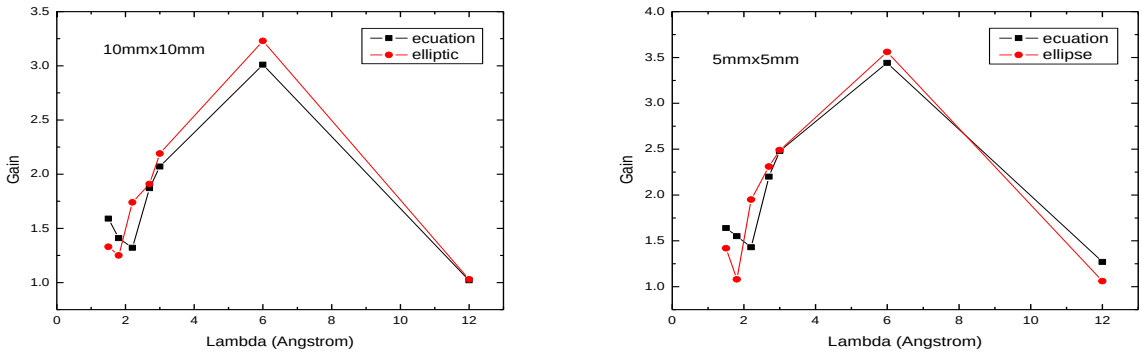

Fig.5.37. Gains obtained for the case of vertical focusing λ = 1.5 Å

The divergences in the case of elliptic and parabolic shape equation case are presented below for different wavelengths:

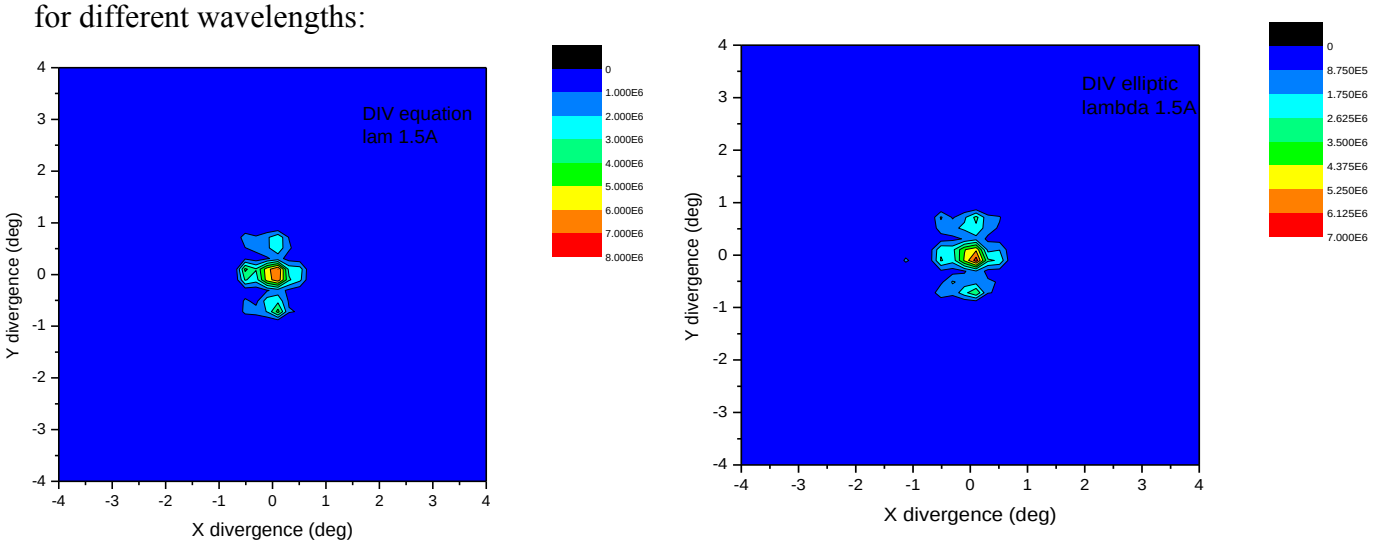

Fig.5.38.Divergency for λ =1.5 Å for parabolic shape (left) and elliptic (right) case

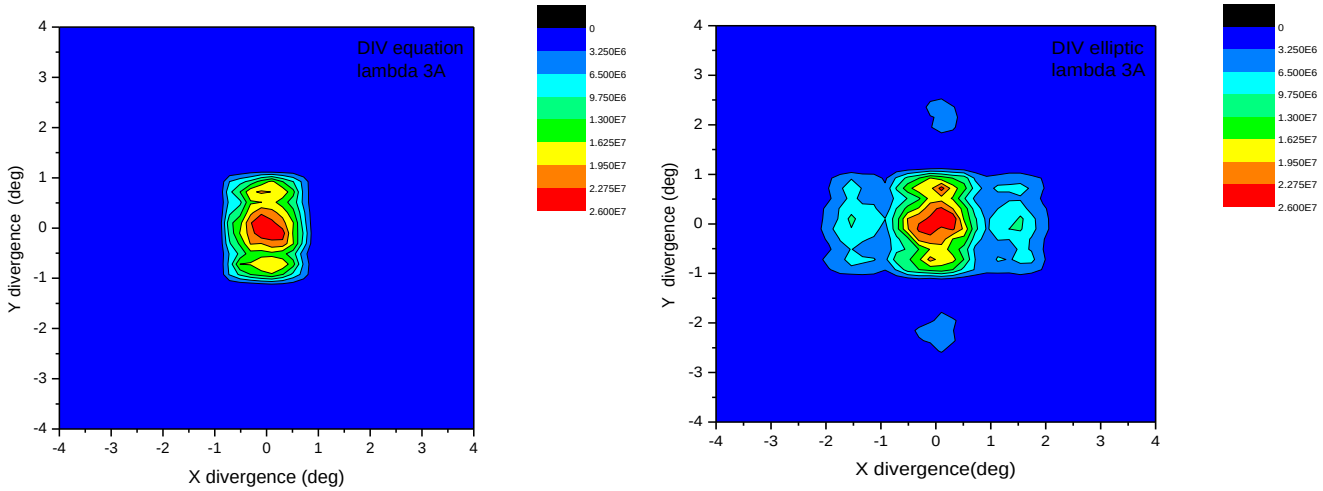

Fig.5.39.Divergency for λ = 3Å for parabolic shape (left) and elliptic (right) case

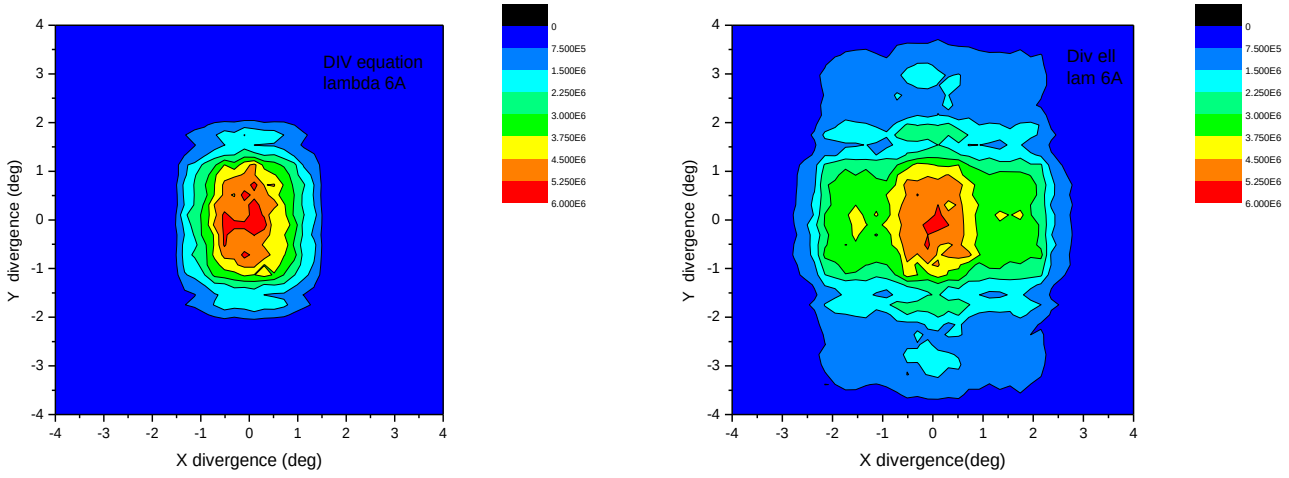

Fig.5.40.Divergency for λ = 6 Å for parabolic shape (left) and elliptic (right) case

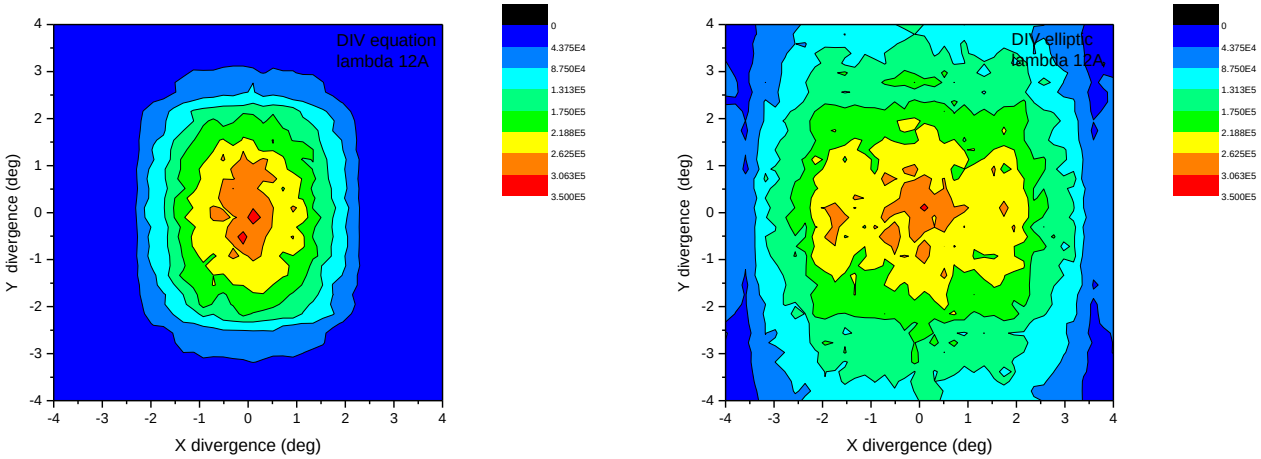

Fig.5.41.Divergency for λ =12 Å for parabolic shape (left) and elliptic (right) case

For all simulated wavelengths the divergence for the walls following the equation is much smaller than that for the walls following the elliptic curvature, whereas the gains are comparable. For this reason we have chosen the option given by equation shape. If we now consider λ = 4 Å and we calculate the loss in intensity for the case when we focus only up and down and the case when we focus with all the 4 walls we obtain a loss of 0.085% in Intensity and a difference in FWHM of 0.093%.

5.4. First tests of the prototype at TOFTOF

The prototype has been developed in order to replace the existing linear collimator at TOF TOF, at the present located in the exchange guide. The latter consists of two vertical switchable stages: a linear collimator namely and a linearly focusing guide. Fig 5.42 shows the prototype mounted in the place of the collimator and aligned with the centre of the beam.
As resulting from the Monte Carlo simulations which have been performed, the adaptive guide is expected to work in the whole typical range of TOFTOF wavelengths (from 1.5 up to 12 Å). Independently from the wavelength, it will be able to keep the beam focused at the sample position, located 200 mm away from the exit of the prototype, with an intensity gain. Considering the integrated intensity over an area of 10 mm x 10 mm a factor 2 of improvement will be achieved.

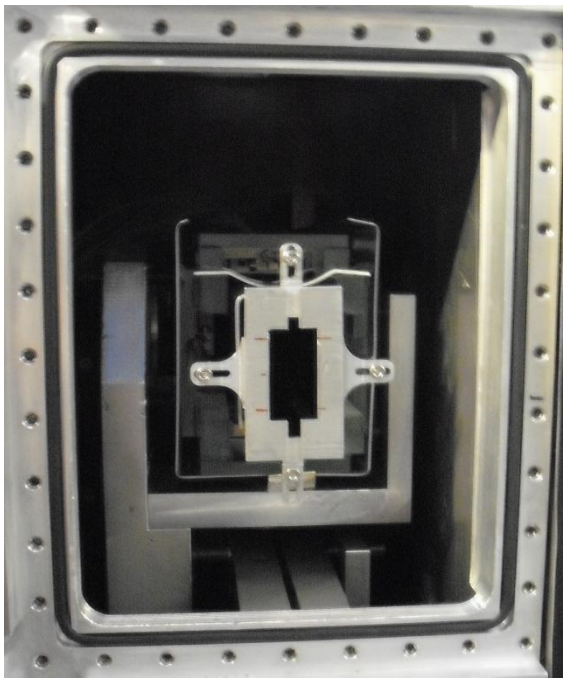

Fig. 5.42. Prototype mounted at TOFTOF

For testing the beam properties a neutron camera (Del Cam) has been placed at the sample position. The neutron camera detects neutrons making use of a ^{6}LiF/ZnS scintilator and covers an area of 98 mm x 65 mm. Placing the camera at the sample position, we have set the curvature of the walls up to the optimal curvature. In fig. 5.43 are the pictures taken with the DelCam at the sample position (focal point) for different wavelengths. On the left side is the beam distribution with the old guide (linear guide) and on the right side of fig. 5.43 with the prototype. For testing the beam homogeneity, we have performed horizontal and vertical cuts through the centre of the beam, as well as at position +5 mm and -5 mm both in horizontal and in vertical direction.

Initial linear guide at sample position *Prototype at sample position*

a) Lambda 2 Å

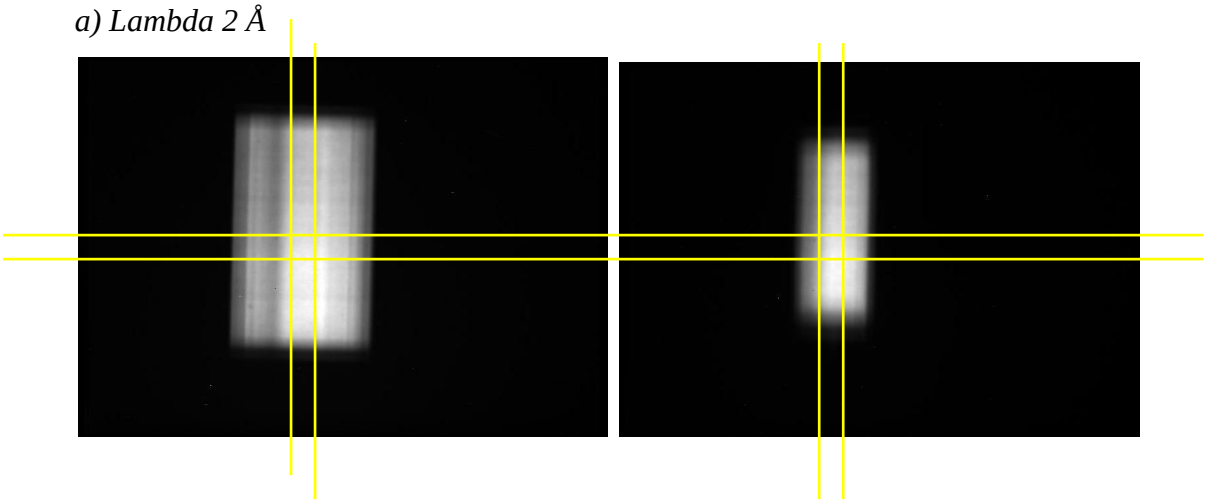

λ= 2Å R=2 v=12000 rpm

horizontal cuts vertical cuts

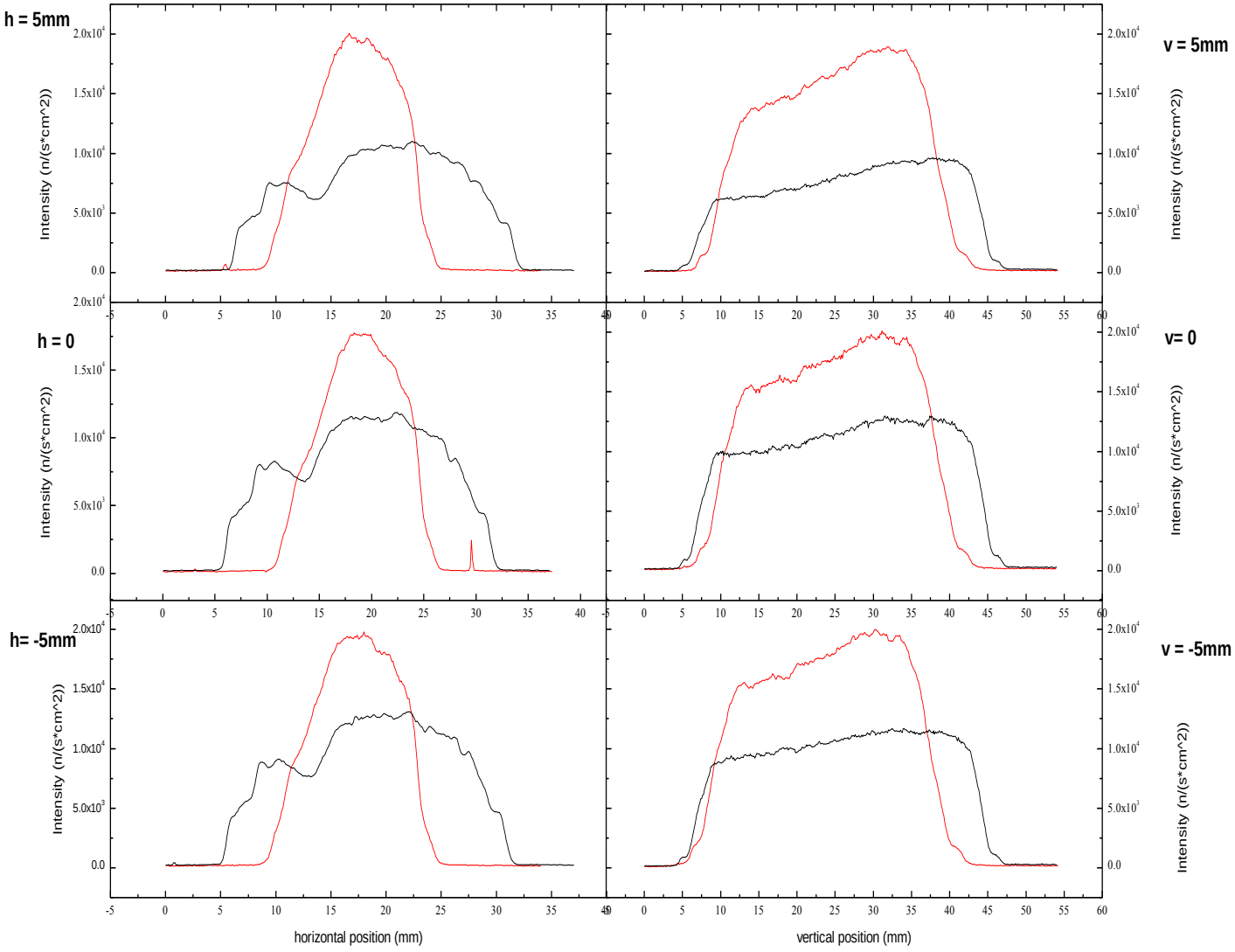

Initial linear guide at sample position *Prototype at sample position*

b)Lambda 3 Å

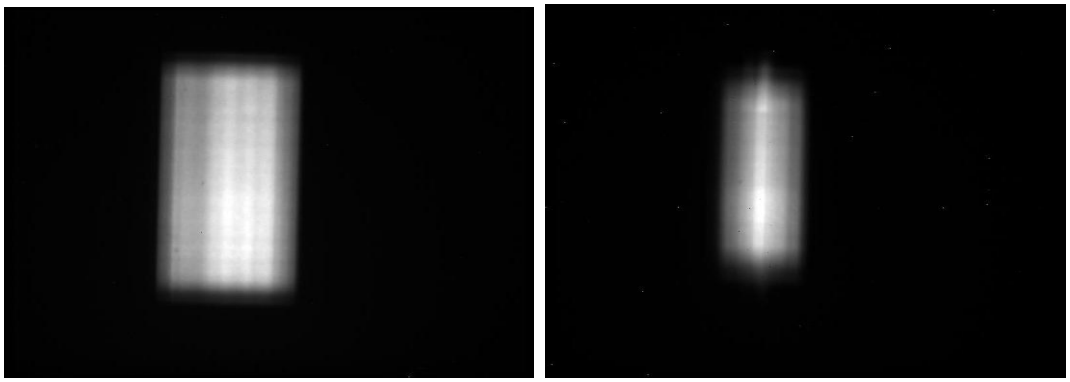

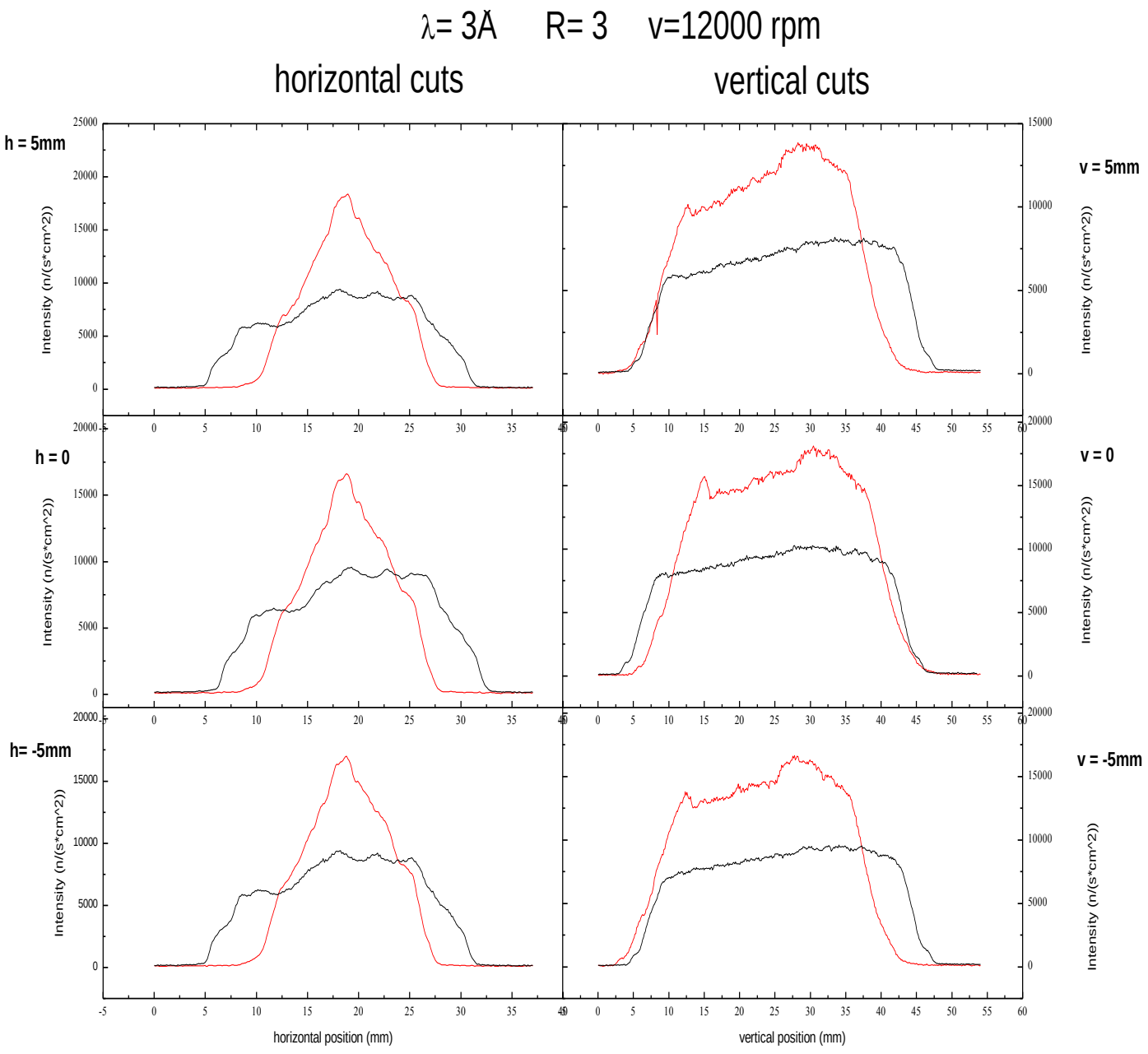

Initial linear guide at sample position *Prototype at sample position*

c) Lambda 6 Å

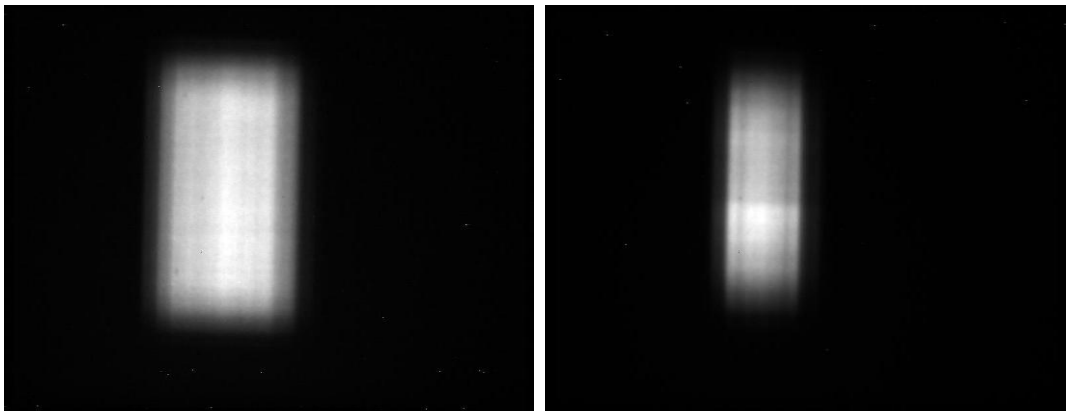

λ= 6Å R= 4 v=12000 rpm

horizontal cuts vertical cuts

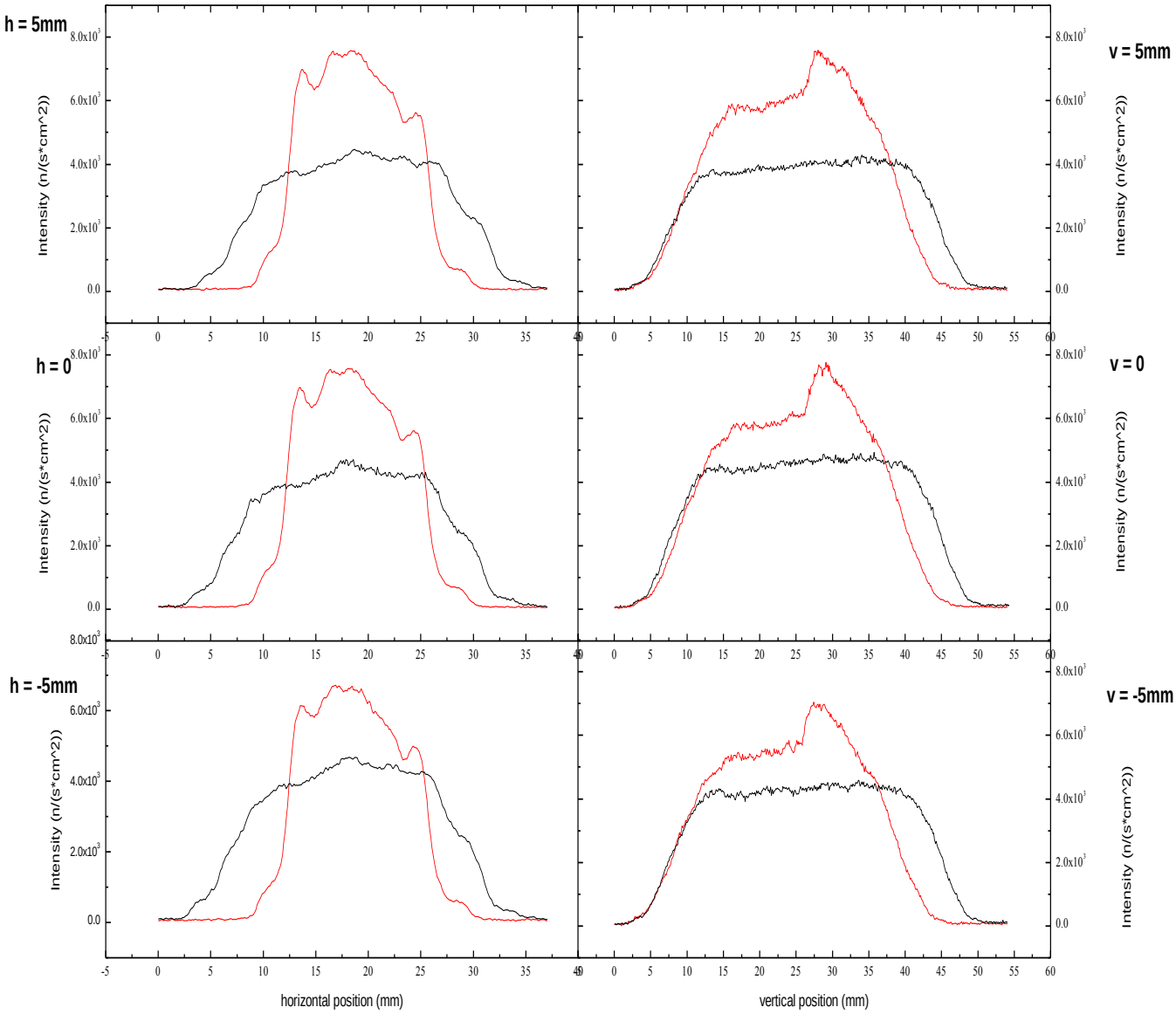

Initial linear guide at sample position *Prototype at sample position*

d) Lambda 8 Å

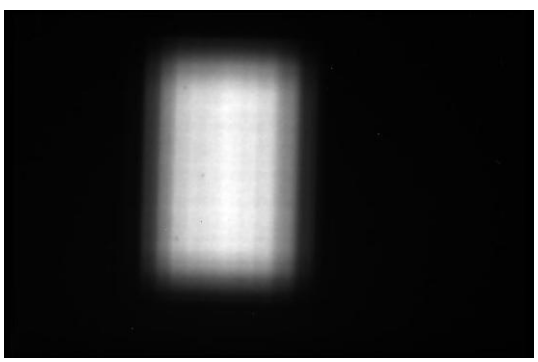

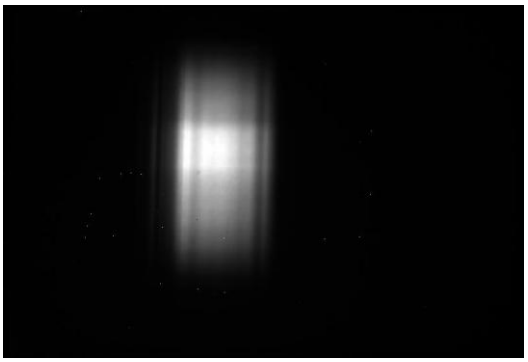

λ= 8Å R= 5 v=12000 rpm

horizontal cuts vertical cuts

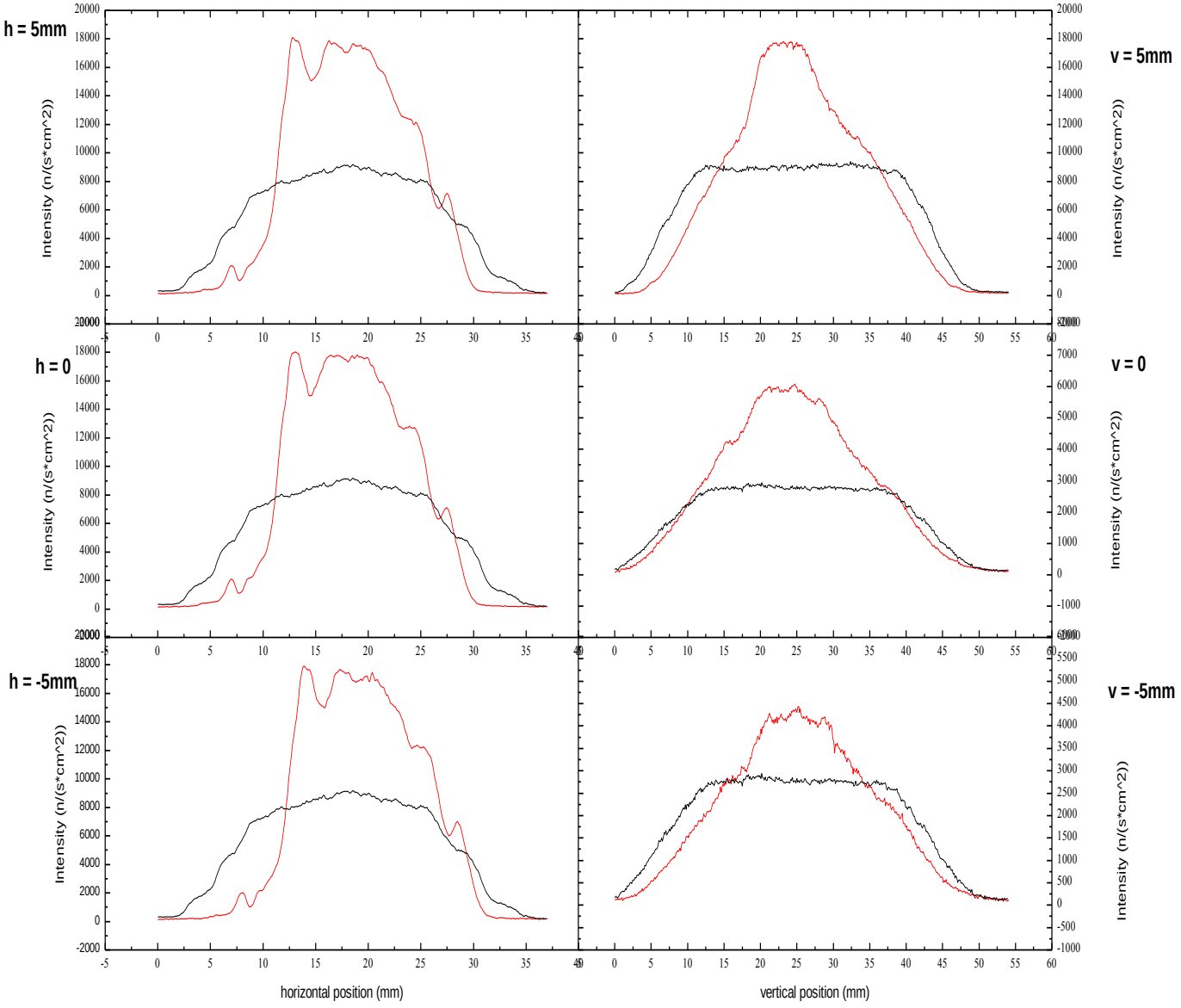

Initial linear guide at sample position *Prototype at sample position*

e) Lambda 12 Å

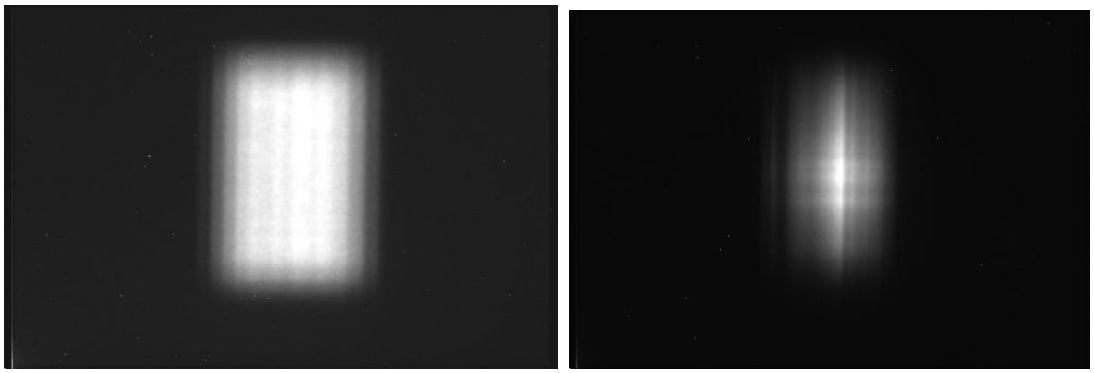

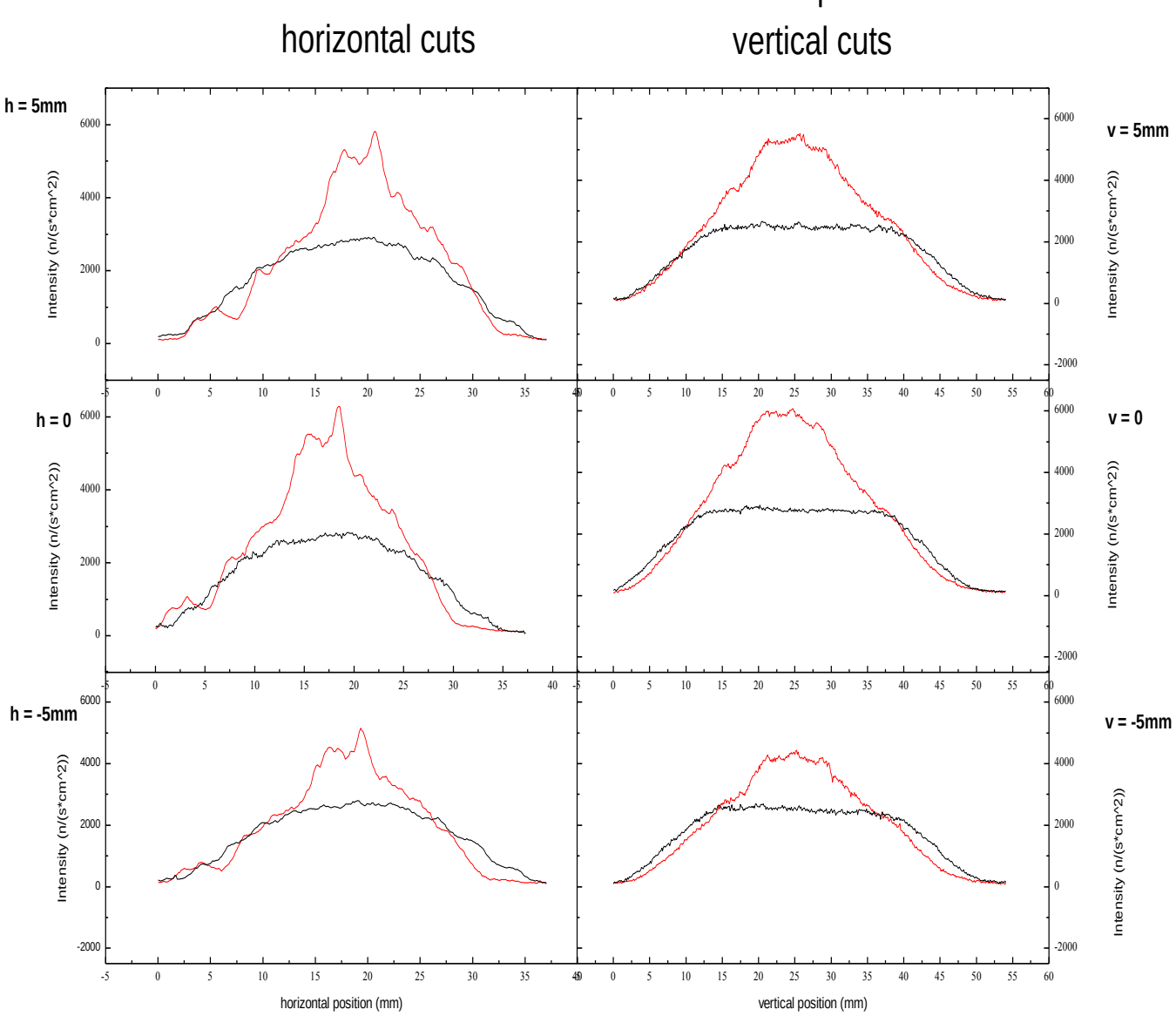

Fig. 5.43 Pictures taken with the DelCam for different wavelengths, together with horizontal and vertical cuts (black- curves for the initial guide, red- curves for the prototype)

From the cuts in fig.5.43 we calculated the horizontal and vertical FWHM of the beam (presented in fig. 5.44). There is a reduction of the FWHM of the beam from 23 mm x 39 mm in the initial case to 11 mm x 26 mm in the case of the prototype.

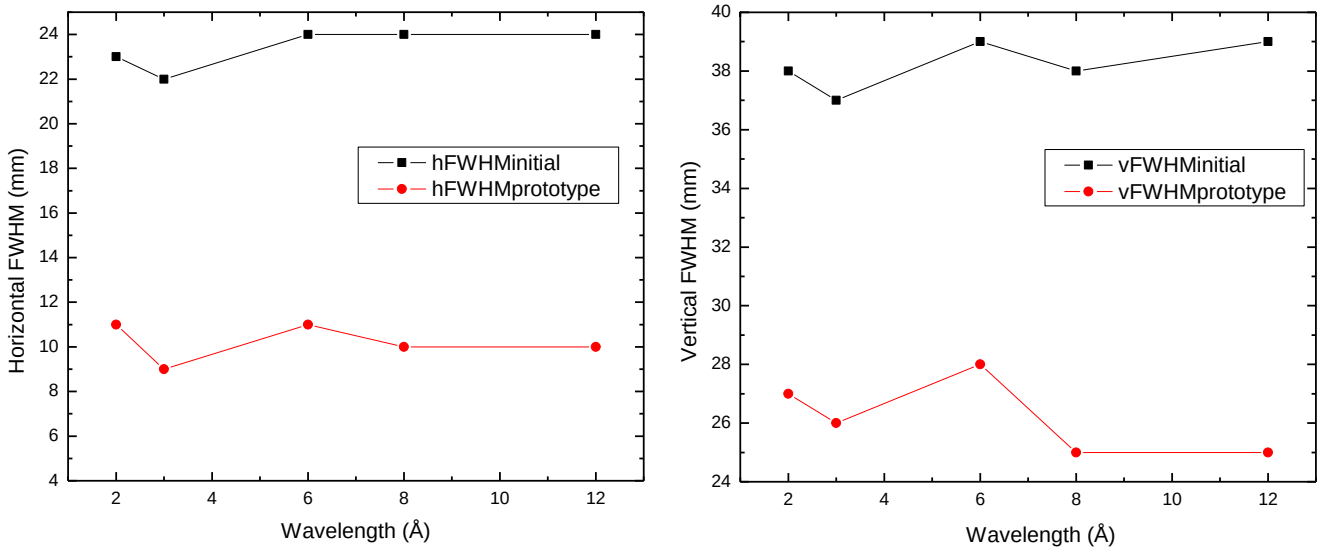

Fig.5.44 Horizontal (left) and vertical (right) FWHM calculated for the initial (in black) and for the prototype (in red)

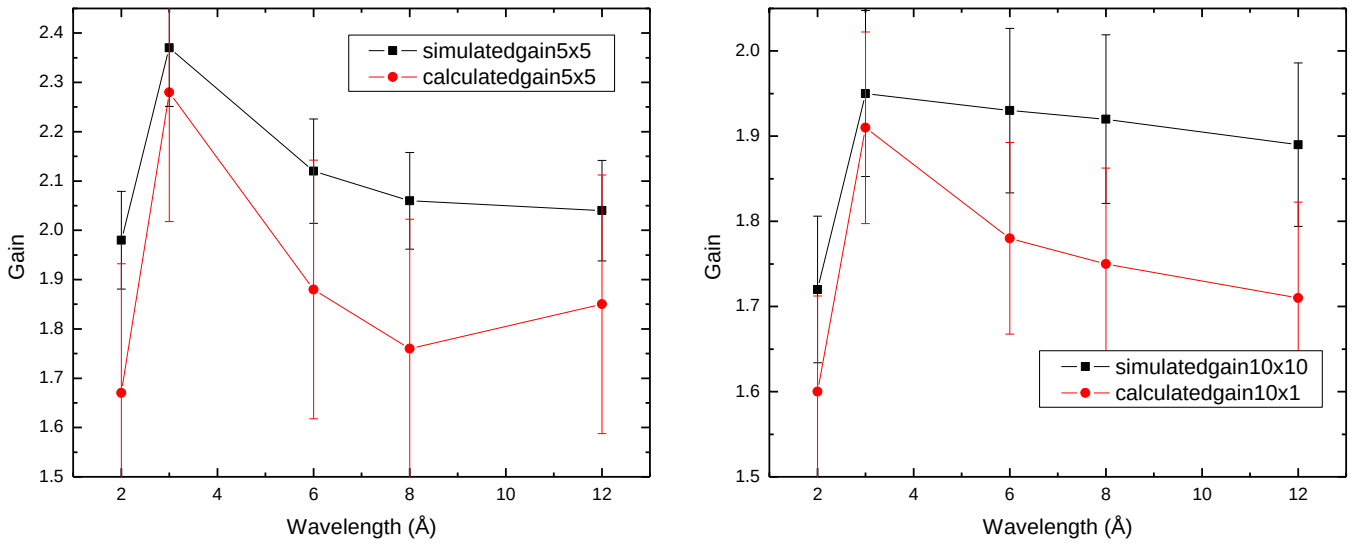

Fig.5.45 Comparison between the gain resulting from the simulation (in black) and the gain calculated from the measurements with the DelCam (in red) for an area of 5mm x 5mm (left) and 10mm x 10mm (right)

Gain factors (calculated as intensity integrated over an area of 10 mm x 10 mm and 5 mm x 5 mm correspondingly for the prototype divided by the integrated intensity over the same area for the linear guide) between 1.6 and 2 were calculated from the DelCam measurements (see fig.5.45). The decrease in gain for larger wavelengths may be explained by the Garland reflections that smear the beam at focal point or to the m-value of the coating that was only 3.5. There is also a loss in intensity due to the gaps appearing when the curvature of the adaptive guide is varied.

An inhomogeneity of the beam was observed (this inhomogeneity was already present and known at the instrument). This may be due to the gravity effects and to the S-shaped curved primary neutron guide. Generally, when dealing with small samples, the beam cross-section which illuminates the sample is chosen smaller accordingly with the samples dimension (in our case 10 mm x 10 mm) in order not to illuminate the sample environment (a large source of background). In the same time the centre of the beam should meet the centre of the instrument for a proper calculation of the time-of-flight and the energy of the scattered neutrons. Because of this inhomogeneity, closing the slits (reducing the incoming beam cross section from 40 mm x 25 mm to 10 mm x 10 mm) the flux of the incoming neutrons doesn't scale with area. If for example for an area of 25 mm x 10 mm we have an incoming neutron rate of 10 counts/s, doesn't mean that for an area of 10 mm x 10 mm -10 times smaller, the incoming neutron rate will be 1 count/s. Taking all of the above into account the comparison of the linear guide with the prototype has been done with the slits closed (10 mm x 10 mm).

As sample a hollow cylinder made of Vanadium, 60 mm height, external diameter 25 mm and a thickness of 2 mm) was chosen. This is actually the standard reference for measurements at the instrument). Vanadium was chosen because of it is purely incoherent scattering, therefore only the elastic line was observed with each detector expected to count the same number of neutrons. The measurements were performed for the same wavelengths as with the DelCam, meaning 2, 3, 6, 8 and 12 Å, with the instrument parameters listed in Table 5.16 for each wavelength

wavelength (Å)	Ratio	velocity (rpm)
2	2	12000
3	3	12000
6	4	12000
8	5	12000
12	8	12000

Table 5.16 Parameters for setting each wavelength at the instrument TOFTOF

The information that was extracted from the experiment at the time of flight instrument was the scattering function S(q,ω) shown at significant q-values represented in the following figures for all the wavelengths. The intensity of all spectra has been normalized to the intensity of the incoming beam.

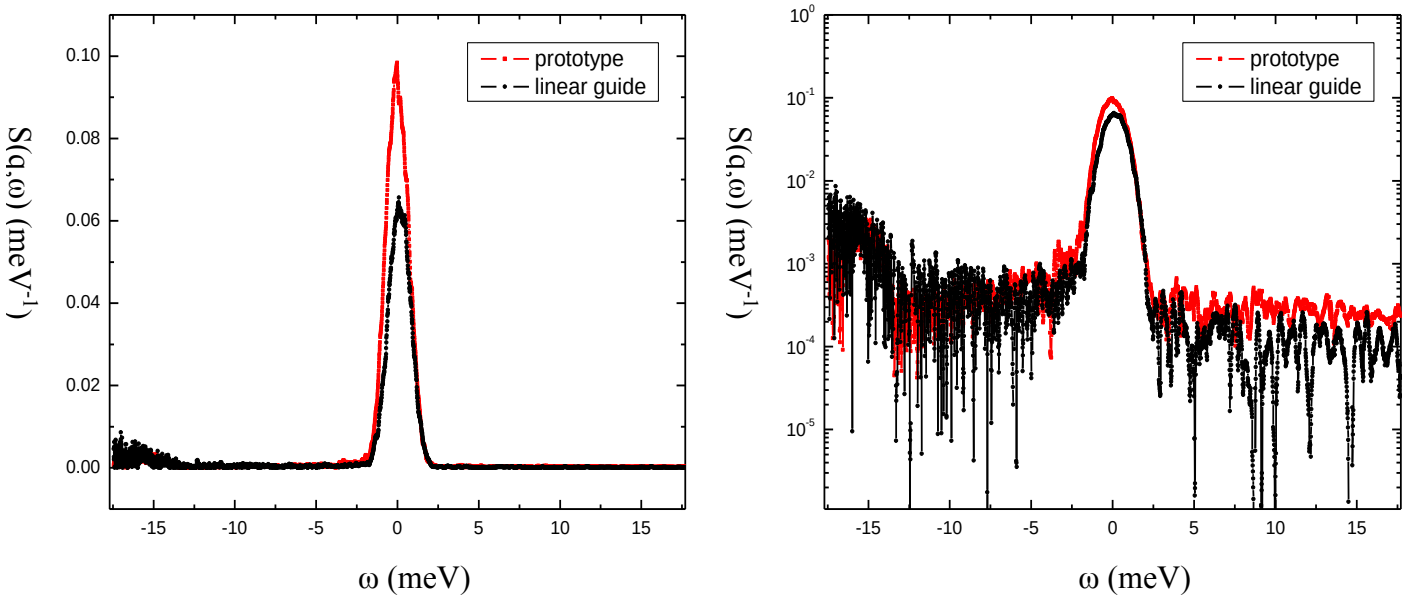

Fig.5.46. Scattering function for 2 Å neutrons (left) and logarithmic representation for a better distinction of the background difference for the two cases (right) at q = 3.1 A^{-1}

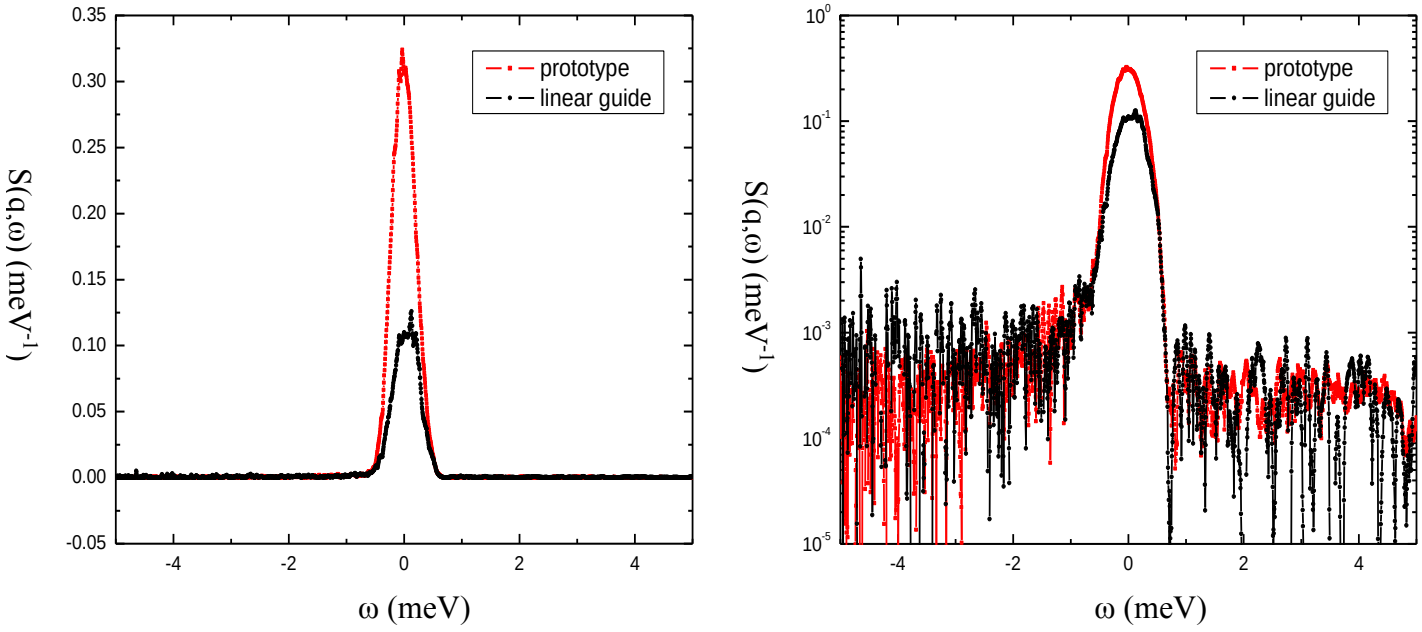

Fig.5.47. Scattering function for 3 Å neutrons (left) and logarithmic representation for a better distinction of the background difference for the two cases (right) at q = 2.1 A^{-1}

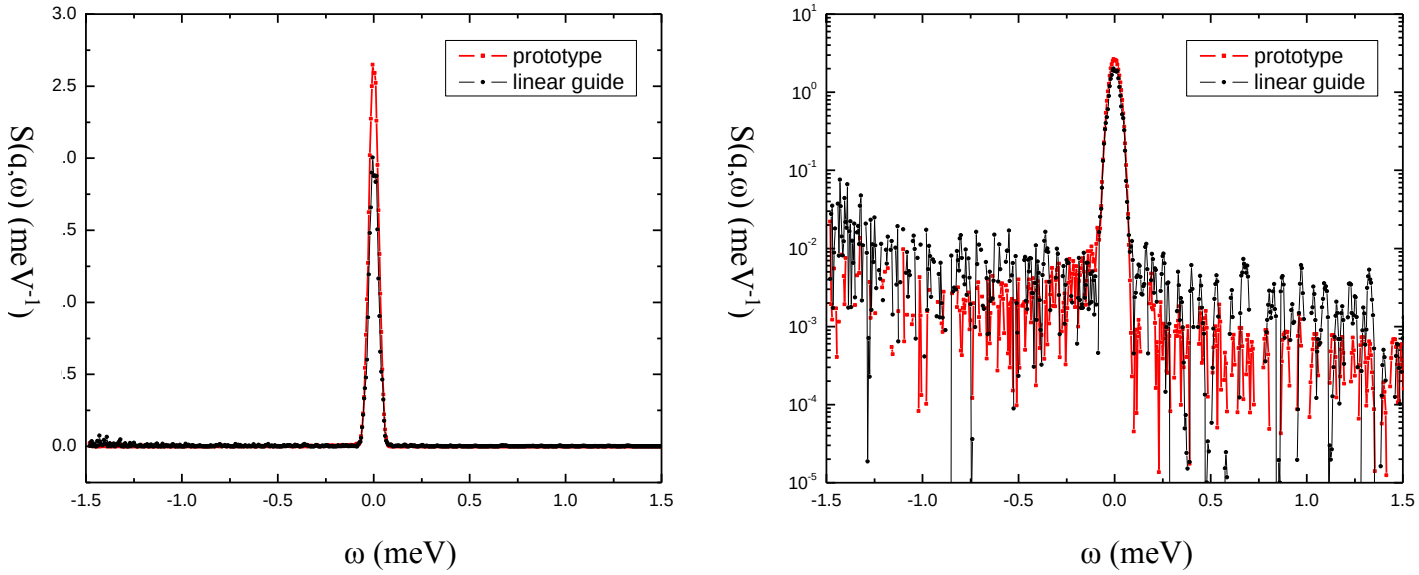

Fig.5.48. Scattering function for 6 Å neutrons (left) and logarithmic representation for a better distinction of the background difference for the two cases (right) at q = 1 A^{-1}

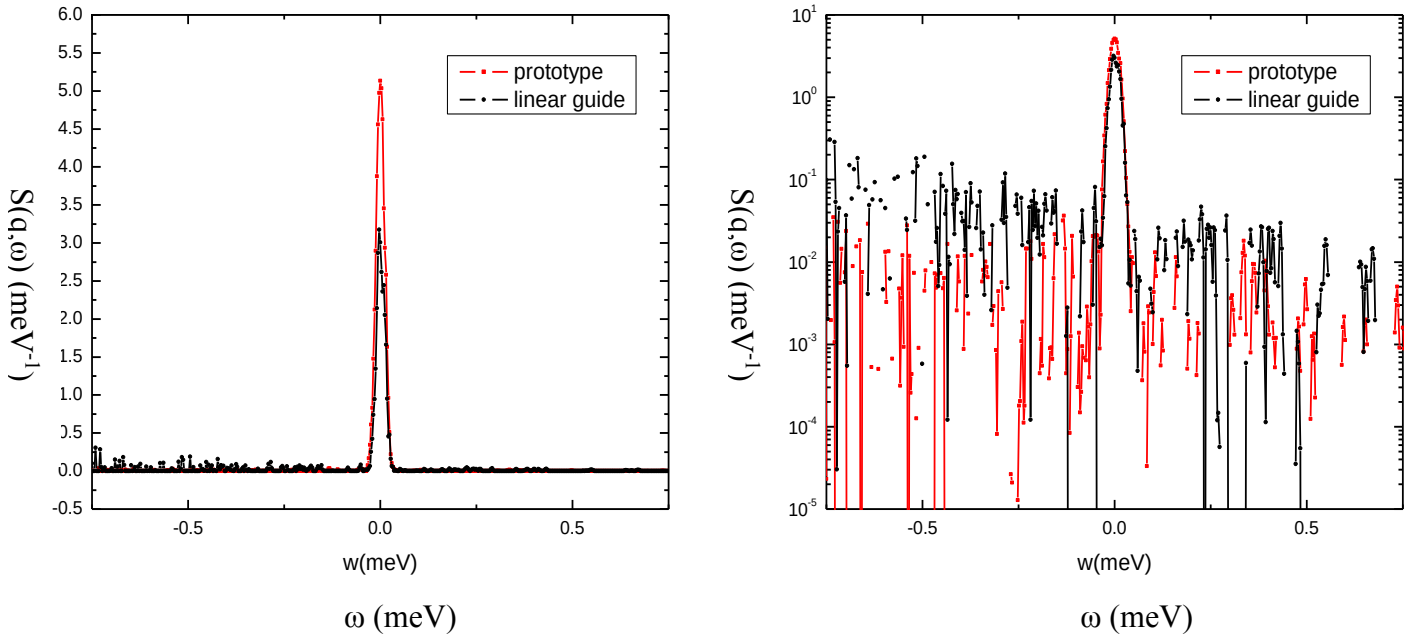

Fig.5.49. Scattering function for 8 Å neutrons (left) and logarithmic representation for a better distinction of the background difference for the two cases (right) at q = 0.78 A^{-1}

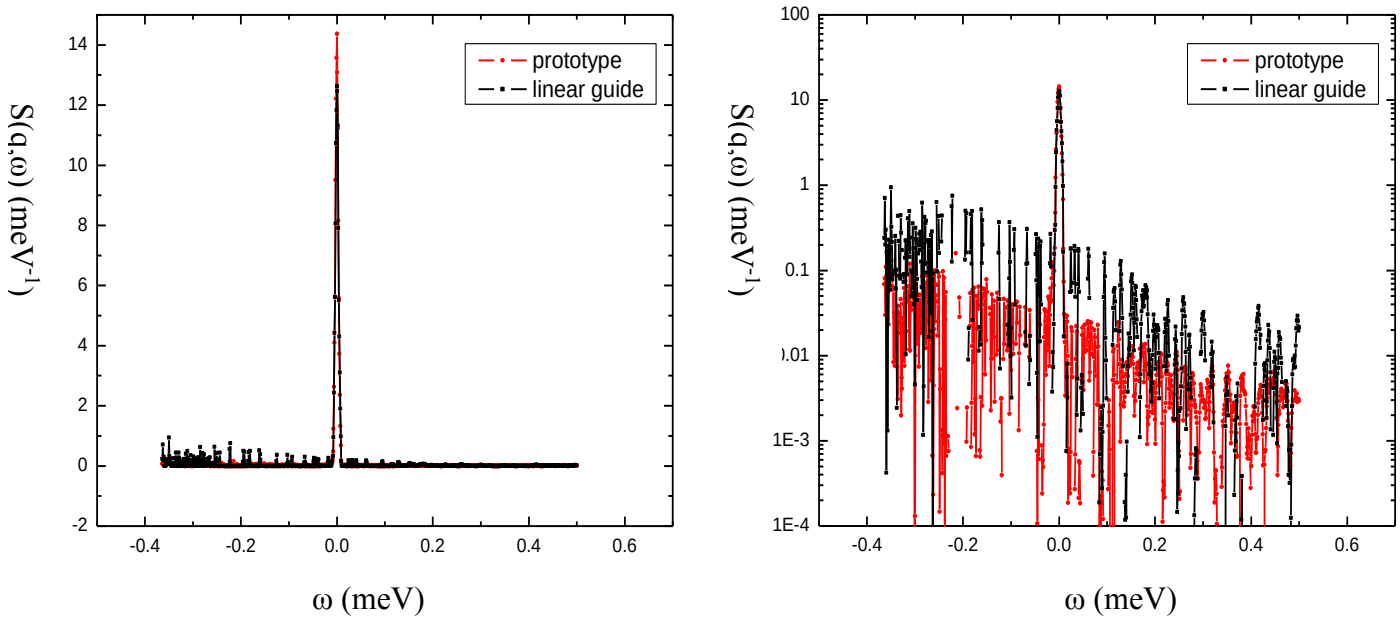

Fig.5.50. Scattering function for 12 Å neutrons(left) and logarithmic representation for a better distinction of the background difference for the two cases (right) at q = 0.51 A^{-1}

With the DelCam measurements we have observed that more neutrons reach the sample (already with open slits we have a gain factor of 2). Closing the slits we see that we can gain more because we avoid the inhomogeneity of the beam. There is less contribution from the sample environment so less background, especially at high wavelengths, typically used for high resolution measurements. One gets a higher signal-to-background ratio, especially at high q values. This means that because of the better focus we not only get a better statistics (i.e. more neutrons), but we also use the neutrons in a more efficient way.

6. Conclusions

First tests with an adaptive neutron guide optimized for the time of flight instrument TOFTOF at FRM II were performed with promising results. The tests show that a gain in intensity of factor 2 can be achieved for the entire bandwidth of the instrument (from 1.5 Å up to 12 Å) calculated for an area of 10 mm x 10 mm at sample position, results that are in agreement with the performed Monte Carlo simulations. There is also a reduction of the dimension of the beam from 23 mm x 39 mm in the initial case to 11 mm x 26 mm in the case of the adaptive guide. This opens wide possibilities in measuring small samples with less contribution from the sample environment so less background, especially at high wavelengths, typically used for high resolution measurements. The main advantage is that the guide is focusing the neutron

beam for all wavelengths at the same position (the sample position), only by the change in the curvature of the guide (therefore the adaptive guide is working as it was expected to do). Performing elastic scattering on a Vanadium sample, we obtained a higher signal-to-background ratio in the case of the adaptive guide, therefore we not only gain in intensity, but we also use the neutrons in a more efficient way.

Further steps in improving the adaptive guide could be the increase of the m-value of the supermirror coating (the replace of the existing m = 3,5 coating with an m = 6 one is expected to bring a gain factor of 2.78 in Intensity at sample position) or the design of a shielding frame for the gaps appearing in the guide when changing the curvature for higher wavelengths.

We can conclude that adaptive guides could be implemented at all instruments that need to vary the properties of the beam at the sample position (intensity and beam width) and that by use of Monte Carlo simulation one could optimize the proper shape of the focusing guide according with the desired beam properties.

Appendixes

5.a. Restrictions due to given geometry

The prototype is going to be placed at the position of the exchange guide (see fig.5.a.1) where a motor can bring it into the beam. At present the exchange guide has the option of a linear guide (represented in blue) and a collimator (in black), that will be replaced by the prototype. In front of the exchange guide there is a focusing linear guide which delivers an entrance angle for the prototype of 0.1 degrees. The entrance dimensions of the adaptive focusing guide are: height of 52.18 mm and width of 23 mm and the exit dimensions vary from 25.3 mm x 11.16 mm for a wavelength of 1.5 Å up to 31.2 mm x 13.6 mm for 12Å.
The length of the exchange guide is 500 mm but in order to be able to move the prototype in and out the beam without reaching the end of the surrounding structure, the length was set to 495 mm. The total external case dimensions of the prototype with all the adjusting parts have to be 104 mm height and 75 mm width.

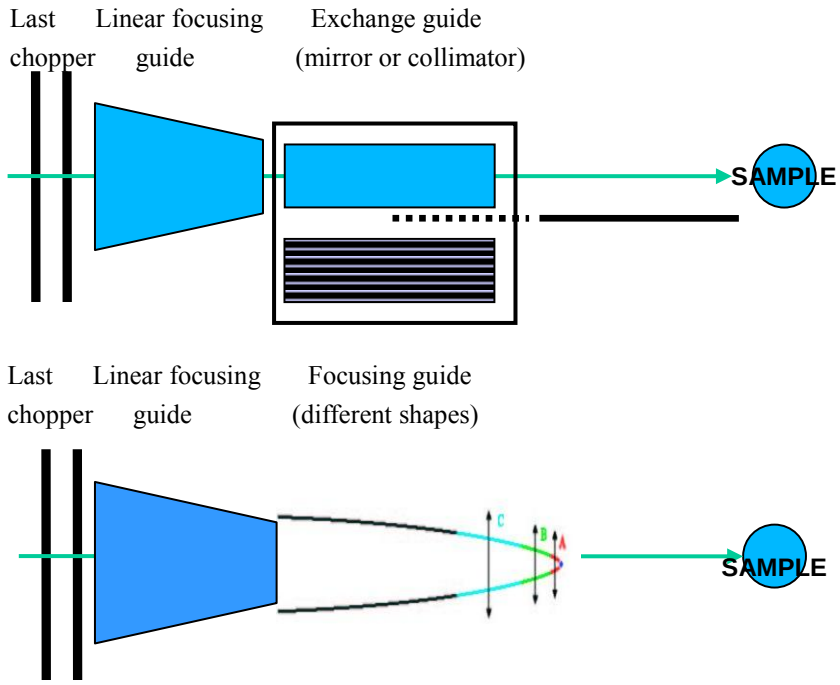

Fig.5.a.1 Schematic of the last part of neutron guides at TOFTOF

5.b. PiezoMotor

The Piezo LEGS linear motor is intended for a very large range of applications. The motor is ideally suited for move and hold applications or for automatic adjustments. This is due to the fact that the motor does not require any power in hold position as well as that the motor has no backlash and can move in increments of single nanometers.

The maximum force of the motor is set by the number of springs giving the force. The standard motor is set for a stall force of 6.5N. Higher forces are optional (up to 10 N).

The motor can move in full steps, shorter steps or partial steps (micro-stepping) giving positioning resolution in the nanometer range. For extreme positioning requirements in the sub-nanometer range a bending mode is possible. Speed is easily adjustable from extremely low up to maximum specified.

PiezoMotor offers a range of drivers and controllers. The basic one is a handheld push button driver. An option is the PDA 3.1 analogue driver that regulates the motor speed by means of an analogue ±7 Volt interface. The more advanced alternative is the PMD90 microstepping driver/controller. This product enables the user to vary the waveforms as well as speed. The microstepping feature divides full step cycle in up to 2048 increments which results in steps as small as two nanometers.

5.c Calibration

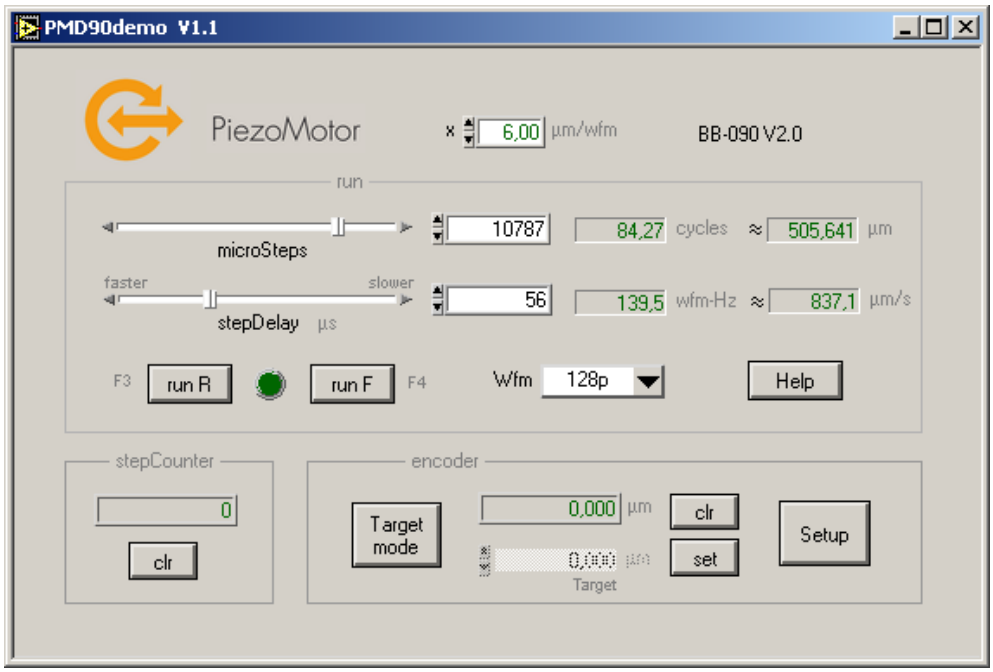

Fig.5.c.1 Software for operating the piezomotor

In the software that is used to operate the piezo motor (PMD90 microstepping driver/controller), the speed and the number of steps of the motor can be varied (see picture). There are 3 intervals of speed (given by Wfm option – short form from Waveform) which can be chosen - the 3 intervals are listed in the table below

Option	Lower limit (µm/s)	Upper limit (µm/s)
32p	60	10000
128p	15	5859
2048p	0.9	366

Table 5.c.1 Speed limits for the motor

With one of these options one chooses the speed interval and with the Cursor ~~–s~~tepDelay" one can choose discrete values in this interval.

Calibration for:-*the upper wall*

For the upper wall we have introduced a motor that has a maximum force of 12N. We have started with a wavelength of 1.5A. For this wavelength we have run the motor to the built end point (that corresponds to a run of the motor of 15 000 steps at a speed of 4000µm/s) and the run back with the low speed 60µm/s various number of steps. We measure then with the theodolyte the curvature obtained and calculated the standard deviation for each measurement (see table 5.c.2) to establish the number of steps necessary for this wavelength and we have also repeated the measurements for the chosen number of steps in order to test the reproducibility. The motor has to take back 1000 steps to reach the needed curvature. The same procedure has to be done for the wavelength of 12Å (see table 5.c.3).

Steps	Standard deviation (rad)
500	0.0015470
580	0.0009557
630	0.0008585
700	0.0013895
800	0.0009549
900	0.0008048
1000	0.0007351
1000	0.0007516
1000	0.0008416
1000	0.0007251
1000	0.0008248
1000	0.0007476
1100	0.0013290

Table 5.c.2 Standard deviation for 1.5Å

Steps	Standard deviation (rad)
1250	0.0019394
1400	0.00129117
1600	0.00064888
1700	0.00066364
1650	0.00060143
1650	0.00061731
1650	0.00062437
1650	0.00063443
1650	0.00063815

Table 5.c.3 Standard deviation for 12Å

For 12 Å the motor has to make 1650 steps back to reach the needed curvature.

Proceeding with the next wavelengths 3, 6 and 9 Å we were able to find the number of steps necessary to run back for reaching each of the necessary curves.

lambda	steps
1.5	1000
3	1225
6	1400
9	1525
12	1650

Table 5.c.4 Number of steps to run back for each wavelength

Plotting the number of steps dependent of wavelength we obtained the equation below that allows then to the number of steps for each desired wavelength

The side walls

For the side walls we had 2 motors to adjust (one with a maximum force of 12N named motor1 on the left side and one with a maximum force of 10N named motor 2 on the right side)We have started with a wavelength of 1.5A. For this wavelength we have run the motor to the built end point (that corresponds to a run of the motor of 10 000 steps at a speed of 4000µm/s) and the run back with the low speed 60µm/s various number of steps. We measure then with the theodolyte the curvature obtained and calculated the standard deviation for each measurement (see table 5.c.5 and 5.c.6) to establish the number of steps necessary for this wavelength and we have also repeated the measurements for the chosen number of steps in order to test the reproducibility.

Steps	Standard deviation (rad)
925	0.0000859
775	7.746E-05
800	0.0001023
785	0.0000577
790	0.0000539
790	0.0000517
790	0.0000523

Table 5.c.5 Standard deviation for 1.5Å for motor 1

Steps	Standard deviation (rad)
900	0.0002176
870	0.0001985
750	0.0003066
820	0.0000787
820	0.0000710
820	0.0000506
820	0.0000676

Table 5.c.6 Standard deviation for 1.5Å for motor 2

Therefore the motor1 has to take back 790 steps and motor2 820 steps to reach the needed curvature. The same procedure has to be done for the wavelength of 12Å (see table 5.c.7 and 5.c.8).

Steps	Standard deviation (rad)
1365	1.62249E-04
1350	9.39489E-05
1230	8.98557E-05
1220	4.62871E-05
1220	4.63451E-05
1220	4.71241E-05

Table 5.c.7 Standard deviation for 12Å for motor 1

Steps	Standard deviation (rad)
1250	5.6463E-05
1150	6.53964E-05
1150	6.10567E-05
1150	6.43732E-05

Table 5.c.8 Standard deviation for 12Å for motor 2

For 12 Å the motor1 has to make 1220 steps back and motor 2 1150 steps in order to reach the needed curvature. Proceeding with the next wavelengths 3, 6 and 9 Å we were able to find the number of steps necessary to run back for reaching each of the necessary curves.

lambda	steps
1.5	975
3	1010
6	1070
9	1135
12	1220

Table 5.c.9 Number of steps to run back for each wavelength for motor 1

lambda	steps
1.5	920
3	960
6	1050
9	1085
12	1150

Table 5.c.10 Number of steps to run back for each wavelength for motor 2

The lower wall

For the lower wall we mounted a motor with a maximum force of 20N to compensate the weight of the entire plate plus motor. We have started with a wavelength of 1.5A. For this wavelength we have run the motor to the built end point (that corresponds to a run of the motor of 20 000 steps at a speed of 4000µm/s) and the run back with the low speed 60µm/s various number of steps. We measure then with the theodolyte the curvature obtained and calculated the standard deviation for each measurement (see table 5.c.11) to establish the number of steps necessary for each wavelength.

lambda	steps	Standard deviation (rad)
1.5	300	0.00059373
	230	0.00051059
12	950	0.00045459
	925	0.00040353
9	800	0.00059373
	825	0.00051059
	850	0.00045675
6	750	0.00040039
	750	0.00035747
3	500	0.00024485
	500	0.00021819

Table 5.c.11 Standard deviation for each wavelength

Therefore we were able to find the number of steps necessary to run back for reaching each of the necessary curves.

lambda	steps
1.5	230
3	500
6	750
9	850
12	925

Table 5.c.12 Number of steps to run back for each wavelength

References

[Ande01] I. Anderson, From 1 to m: the development of supermirrors, *Neutron Optical Devices and Aplications 1992*

[Ande02] K. Andersen; D. Bazzoli, J. Beaucour, E. Farhi, S. Fuard, R. Gähler, T. Hürlimann, M. Kreuz, C. Mounier, A. Perillo-Marcone ,Neutron Guides – a review after 40 years of ILL, ILL-Grenoble, 2007

[Arzu01] S. Arzumanov, L. Bondarenko, S.Chernyavsky et.al., Phys.Lett. B 483 (2000), 15-22

[Asch01] B Aschenbach Rep. Prog. Phys., vol 48,1985,pp 579-629

[Baco01] G.E. Bacon, Neutron diffraction, Claredon Press, Oxford, 1979

[Boen01] P. Boeni, Supermirror-based beam devices, *Phyisica B 234-236(1997)*

[Boen02] P Boeni, D. Clemens, Challenges in the field of large m supermirrors, *Phyisica B 241-243(1998)*

[Boen03] P. Böni, Nucl. Instrum. Methods Phys. Res., Sect. A 586 (2008) 1

[Brue01] T. Brueckel, G. Hegel, D.Richter, Neutron scattering, FZ Jullich, 2000

[Chan01] J. Chang, N. B. Christensen, Ch. Niedermayer, K. Lefmann, H. M. Rnnow, D. F. McMorrow, A.Schneidewind, P. Link, A. Hiess, M. Boehm, R. Mottl, S. Pailhes, N. Momono, M. Oda, M. Ido, J.Mesot, Phys. Rev. Lett. 102 (2009) 177006

[Chri01] J. Christ, T. Springer, Ueber die Entwicklung eines Neutronenleiters an FRM Reaktor, *Nukleonik 4 (1962) 23*

[Chup01] T Chupp, Neutron optics and polarisation

[Clyn01] James R. Clynch, Newell Garfield, Equations of an Ellipse August 2006

[Dail01] J. Dailant, A. Gibaud, X-ray and neutron reflectivity: Principles and Aplications Lecture Notes in Physics Springer (2009)

[Dobr01] Dobrzynski, L.; Blinowski, K. In Neutrons and Solid State Physics; Cooper, M.; Ed.; Ellis Horwood Series and number; Publisher: New York, NY, 1994; Vol. 3, pp 8-16.

[Focu01] Focusing properties of spherical and parabolic mirrors, Physics 5B, 2009

[Hayt01] J.B. Hayter, H.A.Mook, Discrete thin-film multiplayer design for x-ray and neutron supermirrors, *J.Appl. Cryst. 22, 1989*

[Helm01] http://www.helmholtz-berlin.de/angebote/arbeiten-lernen/info/neutronen/eigenschaften_en.html

[Hend01] J.S.Hendricks, A Monte Carlo Code for Particle Transport, Los Alamos Science Number 22,1994

[Ibbe01] R. M. Ibberson, Nucl. Instrum. Methods Phys. Res., Sect. A 600 (2009) 47

[Jano01] M Janoschek, P Böni, M Braden Optimisation of elliptic neutron guides for triple-axis spectroscopy

[Kjae01] Peter Kjær Willendrup, Erik Knudsen, Kim Lefmann and Emmanuel Farhi, Component Manual for the Neutron Ray-Tracing Package McStas, Version 1.12

[Koma01] A. Komarek, P. Böni and M. Braden, Nuclear Instruments and Methods in Physics Research A 647 (2011) 63–72

[Kuld01] J. Kulda, J. Saroun, P. Courtois, M. Enderle, M. Thomas, P. Flores, Appl. Phys. A 74 (2002) S246

[Laep01] Volker Läpple, Einführung in die Festigkeitslehre (2008)

[Leib01] H.M.Leibnitz, T. Springer, The use of neutron optical devices on the beam-hole experiments, *Journal of Nuclear Energy Parts A/B 17 (1963) 217*

[Link01] P. Link, G. Eckold, J. Neuhaus, Physica B 276-278 (2000) 122

[Love01] S. W. Lovesey Theory of Neutron Scattering from Condensed Matter (1984), Oxford University Press

[Mess01] Messiah, Quantum Mechanics, Dover Publications, New York (1999)

[Meze01] F. Mezei, Novel polarised neutron devices: supermirror and spin component amplifier, *Communications on Physics 1, 1976*

[Meze02] F. Mezei, P.A. Dagliesh, Corrigendum and first experimental evidence on neutron supermirrors, *Communications on Physics 2, 1977*

[Mild01] D. F. R. Mildner: Acceptance diagrams for curved neutron guides, Nucl. Instr. Meth. A290 (1990), 189

[Mont01] Los Alamos National Laboratory Monte Carlo Team, MCNP — A General Monte Carlo N-Particle Transport Code, Version 5,Volume I: Overview and Theory, 2003

[Mont02] http://www.mcstas.com/documentation/manual/mcstas-1.12-components.pdf

[Mont03] http://www.mcstas.org/download/components/contrib/Guide_four_side.html

[Muhl01] S. Muhlbauer,P.G. Niklowitz, M. Stadlbauer, R. Georgii,P. Link, J. Stahn,P.Boni, Elliptic neutron guides—focusing on tiny samples, Nuclear Instruments and Methods in Physics Research A 586 (2008) 77–80

[Nune01] A.C. Nunes, G. Shirane, Nucl. Instrum. Methods 95 (1971) 445

[Parr01] L. G. Parratt, Phys. Rev. 95, (1954) 359

[Pint01] L. Pintschovius, Nucl. Instrum. Methods Phys. Res., Sect. A 339 (1994) 136

[Prin01] Prince, E. Appl. Spectrosc.Rev.1999, 34, 159-172.

[Pynn01] Pynn, R. Los Alamos Science 1990, 19, 1-31

[Pynn02] R. Pynn, Neutron scattering, Los Alamos National Laboratory, 2009

[Rina01] P. Rinard, Neutron interactions with matter Los Alamos Technical Report http://www.fas.org/sgp/othergov/doe/lanl/lib-www/la-pubs/00326407.pdf

[Rist01] T. Riste, Nucl. Instrum. Methods 86 (1970) 1

[Scha01] C. Schanzer et al., Nucl. Instr. Meth. A 529 (2004) 63

[Sche01] R. Scherm, G. Dolling, R. Ritter, E. Schedler, W. Teuchert and V. Wagner, Nucl. Instrum. Methods143 (1977) 77

[Sear01] V.F. Sears, Neutron Optics, Neutron scattering in condensed matter, Oxford University Press, 1989

[Sen01] D. Sen, P. Link, K. Hradil, A. Hiess, L. P. Regnault, Y. Sidis, N. Aliouane, D. N. Argyriou, and M.Braden, Phys. Rev. Lett. 98 (2007)1372 06.

[Sivi01] D. S. Sivia Elementary Scattering Theory (for X-ray and Neutron Users) 2010, Oxford University Press

[Skol01] Skold, K.; Price, D.L. Methods of Experimental Physics-Neutron Scattering: Part3, Academic:Orlando, FA,1987,pp 1-45

[Squi01] G.L. Squires, Introduction to the theory of thermal neutron scattering

[Stoc01] O. Stockert, M. Enderle, and H. v. Lohneysen, Phys. Rev. Lett. 99 (2007) 237203.

[Thie01] B. Thielemann, Ch. Ruegg, H.M. Rnnow, A.M. Lauchli, J.-S. Caux, B. Normand, D. Biner, K. W. Krämer, H.-U. Güdel, J. Stahn, K. Habicht, K. Kiefer, M. Boehm, D.F. McMorrow, J. Mesot, Phys.Rev. Lett. 102 (2009) 107204

[Unru01] T. Unruh, J. Neuhaus, W. Petry**,** Nucl. Instr. Methods A 580 (2007) 1414-1422, erratum 585 (2008) 201

[VanH01] L. Van Hove, Phys. Rev. 95, (1954) 249

[Volk01] L.Volker, Einführung in die Festigkeitslehre 2008

[Wagn01] W. Wagner, G.S. Bauer, J. Duppich, S. Janssen, E. Lehmann, M. Luthy, H. Spitzer, J. Neutron Res.6 (1998) 249

[Walt01] Handbook of Physics; Walter, B.; Harris, W. J.; Stocker, H.; Lutz, H., Eds.; Springer: New York, NY, 2002; pp 907-909.

Acknowledgments

Above all, I would like to thank the two persons who hired me for the project, and then stood beside me during the whole period, from the participation in the project, through developing my ideas and learning to present them: Professor Winfried Petry and Professor Peter Böni. They always had a lot of genuine interest, and understanding – when I needed it, for my work. They spent time contemplating my ideas, both those with some possible future and the hopeless ones, always coming back with inspiring comments.

I would like to express my sincere gratitude to Professor Gunther Borchert, who gave me the opportunity to perform this work in the Neutron Optics group and for his support and help during the entire time. Without his support, patience and guidance, this work would not have been completed.

I am also very thankful to Dr. Giovanna Giulia Simeoni for helping me out during the simulations and in data analysis, for her support during the thesis writing period and for always having time for questions and discussions.

Many thanks also to all past and present members of the Neutron Optics group for creating a pleasant and friendly atmosphere and for always being helpful and supportive. A special thanks goes to Josef Weber and Eberhard Kahle for their help in building and mounting the prototype.

I would also like to thank Jochen Stahn, Uwe Filges, Tobias Panzner, Yves Bodenthin and Michael Schneider from PSI for their guidance in Monte Carlo simulations and for offering me the possibility to participate at the first tests made with a prototype for adaptive optics, as well as for sharing with me a new Monte Carlo component that simulated truely curved guides

I am also grateful to Petra Kudejova responsible for PGAA instrument for discussing the simulation results with me and to Andreas Osterman for providing the Monte Carlo simulation codes from various instruments at FRM II.

Part of the work was supported by the project 226507-NMI3 within the the seventh framework program FP7 of the EU.

Finally and most importantly, my most sincere gratitude goes to my family for their love, for the constant support and encouragement throughout my entire life. I thank them for having so much faith in me and for allowing me to be as ambitious as I wanted.

Publication list

Articles

1. **X-ray and neutron reflectivity studies of self-assembled InAs quantum dots stacks on GaAs (1 0 0),** D.F. Anagnostopoulos, E. Skuras, C. Stanley, G.L. Borchert, R. Valicu, *Journal of Alloys and Compounds*, *Volume 483, Issues 1-2*, *26 August 2009*, *Pages 414-417*

2. **Structural and electrical properties of HfO_2/Dy_2O_3 gate stacks on Ge Substrates,** E.K. Evangelou, M.S. Rahman, I.I. Androulidakis, A. Dimoulas, G. Mavrou, K.P. Giannakopoulos, D.F. Anagnostopoulos, R. Valicu, G.L. Borchert, *Thin Solid Films*, *Volume 518, Issue 14*, *3 May 2010*, *Pages 3964-3971*

3. **Focusing Neutrons on Very Tiny Spots,** R. Valicu, P.Böni, *Annual Report E21, TUM, 2008*

4. **Development of higher m-supermirrors,** R.Valicu, R. Iannucci, A. Ofner, G. Borchert, *Annual Report FRM2, TUM, 2008*

5. **Focusing Neutron Beams to Sub-Millimeter Size,** R. Valicu, P.Böni, *submitted to Nuclear Instruments and Methods A*

Conferences- oral contributions

1. **Self-organisation Processes in Ferrofluids,** R. Valicu, L.M. Ivan, D.G.Dimitriu, *National Conference "Physics and new Educational Technologies" Iasi, Romania, July 2006*

2. **Development of higher m supermirrors,** R. Valicu, R. Iannucci, G. Borchert, *DPG Meeting, Dresden,Germany, March 2009*

3. **Adaptive Optics for Extreme Environments**, R. Valicu, P. Böni, *Meeting NMI3 - FP7 - PSI Villigen, Switzerland March 2009*

4. **Focussing SANS**, R. Valicu, P. Böni, *Meeting NMI3 - FP7 - PSI Villigen, Switzerland March 2009*

5. **Monte Carlo simulations for focusing elliptical guides**, R. Valicu, P. Böni,G.Borchert, *Neutron Delivery Systems, Grenoble, France, July 2009*

6. **Monte Carlo simulations for adaptive optics,** R. Valicu, P. Böni, J. Stahn ,U. Filges, T. Panzner, Y. Bodenthin, M. Schneider, C.Schanzer, *International Workshop on Neutron Optics, Grenoble, France, March 2010*

7. **Monte Carlo simulations for extreme environments experiments using adaptive optics**, R. Valicu, P. Böni, *Meeting NMI3 - FP7 - Barcelona, Spain Mai 2010*

8. **Focusing guide for TOFTOF**, R. Valicu, P. Böni, G.G. Simeoni, W. Petry, G. Borchert, *Meeting NMI3 - FP7 - Rome, Italy November 2011*

Conferences - Poster contributions

1. **X-ray and neutron reflectivity studies of self-assembled InAs quantum dots stacks on GaAs (1 0 0),** D.F. Anagnostopoulos,P. Patsalas, E. Skuras,C. Stanley, G.L. Borchert, R. Valicu, A.R.Wildes, *International Conference on Nanosciences and Nanotechnologies NN08, Thessaloniki, Greece, July 2008*

2. **Structural and electrical properties of HfO_2/Dy_2O_3 gate stacks on Ge (1 0 0)** M.S. Rahman, E.K. Evangelou, I.I. Androulidakis, D.F. Anagnostopoulos, R. Valicu, G.L. Borchert, *International Symposium on Metastable and Nanomaterials, ISMANAM2007, Corfu, Greece, August 2007*

3. **Self-assembled InAs quantum dots introduced in the bulk and on the surface of (1 0 0) GaAr grown by molecular beam epitaxy,** D.F. Anagnostopoulos, C. Stanley, E. Skuras, R. Valicu, H. Zoubos, T.H. Makris, G.L.Borchert, *International Symposium on Metastable and Nanomaterials, ISMANAM2007, Corfu, Greece, August 2007*

4. **Developing higher m supermirrors at FRM II**, R. Valicu, R. Iannucci, G. Borchert, *Deutsche Neutronenstreutagung, München, Germany, September 2008*

5. **McStas Simulations for focusing guides**, R. Valicu, P. Böni, *Deutsche Neutronenstreutagung, München, Germany, September 2008*

6. **Monte Carlo Simulations for focusing elliptical guides,** R. Valicu, P. Böni, *DPG Meeting, Dresden,Germany, March 2009*

7. **Focusing Neutron Beams to Sub-Millimeter Size,** R. Valicu, P. Böni, *DPG Meeting, Regensburg, Germany, March 2010*

8. **Adaptive Optics for neutrons – parabolically bent Supermirror,** M. Schneider, J. Stahn, C. Schanzer, T. Panzner, Y. Bodenthin, R. Valicu, P. Böni, *International Workshop on Neutron Optics, Grenoble, France, March 2010*

9. **Development of new focusing neutron guide for TOFTOF,** R. Valicu, G. G. Simeoni , P. Böni, *International Workshop on Neutron Optics, Grenoble, France, March 2010*

10. **The Time-of-Flight spectrometer TOFTOF**, G.G.Simeoni, T. Unruh, S. Busch, R. Mole, L. Peyker, R. Valicu, P. Böni, J. Neuhaus, W. Petry, *European High Pressure Research Group Conference, Uppsala, Sweden, July 2010*

11. **Adaptive optics for TOFTOF**, R. Valicu, G.G.Simeoni, G.Borchert, W. Petry, *DPG Meeting, Dresden, Germany, March 2011*